FINAL REPORT

Development and Evaluation of the FINNv.2.2 Global Model Application and Fire Emissions Estimates for the Expanded Texas Air Quality Modeling Domain

AQRP Project 18-022

Prepared for:
David Sullivan
Texas Air Quality Research Program
The University of Texas at Austin

and

Stephanie Shirley
Texas Commission on Environmental Quality

Prepared by:
Yosuke Kimura and Elena McDonald-Buller (Principal Investigator)
Center for Energy and Environmental Resources
The University of Texas at Austin

Christine Wiedinmyer (Co-Principal Investigator)
Cooperative Institute for Research in Environmental Sciences
University of Colorado, Boulder

and

Nathan Pavlovic, Crystal McClure, Steve Brown, and Fred Lurmann (Co-Principal Investigator)
Sonoma Technology, Inc.

QA Requirements: Audits of Data Quality: 10% Required

September 3, 2019

Table of Contents

LIST OF FIGURES **4**

LIST OF TABLES **10**

ACKNOWLEDGMENTS **11**

EXECUTIVE SUMMARY **12**

1. INTRODUCTION **14**

2. MODELING SYSTEM AND INPUT DATA RESOURCES **16**

2.1 PREPROCESSOR 16
2.1.1 Active Fire Detections *16*
2.1.2 Burned Area *17*
2.1.3 Land Cover Characterization *19*
2.2 EMISSIONS MODEL 23
2.2.1 Final Burned Area *23*
2.2.2 Emission Factors and Chemical Speciation *23*
2.2.3 Biomass Loading *24*
2.2.4 Fraction of Biomass Burned *24*
2.3 COMPUTING ENVIRONMENT 31

3. AIR QUALITY MODELING **32**

3.1 CAMX CONFIGURATION 32
3.2 FIRE EMISSIONS PROCESSING 37
3.3 HYSPLIT SMOKE DISPERSION MODELING 40
3.4 AEROSOL OPTICAL DEPTH 42

4. FIRE EMISSIONS ESTIMATES **44**

4.1 FINN V2.2 EMISSIONS ESTIMATES WITH MODIS AND VIIRS FIRE DETECTIONS 44
4.1.1 Global Regions *44*
4.1.2 Interannual Trends in U.S. Subregions and Mexico *48*
4.2 SENSITIVITY OF EMISSIONS ESTIMATES TO VIIRS ACTIVE FIRE DETECTIONS AND FINN VERSION 55

5. ASSESSMENT OF FINN PERFORMANCE USING SATELLITE OBSERVATIONS **66**

5.1 MAIAC SATELLITE OBSERVATIONS OF AOD 67
5.2 ASSESSMENT OF HYSPLIT DISPERSION RESULTS 69
5.2.1 HYSPLIT Ground-Based Comparison *69*
5.2.2 HYSPLIT vs. MAIAC Observed AOD Comparison *70*
5.2.3 HYSPLIT vs. CAMx v2.2 Wildfire-Only Comparison *71*
5.3 ASSESSMENT OF CAMX MODEL RESULTS 86
5.3.1 CAMx vs. MAIAC comparison *87*
5.3.2 CAMx v2.2 versus CAMx v1.5 ..... *87*
5.4 CASE STUDIES 96
5.4.1 Case Study Selection *96*
5.4.2 Week-Long Case Study for September 19-26, 2012 ..... *97*
5.4.3 June 27, 2012 Case Study *99*
5.4.4 Case Study Summary *99*

6. AUDITS OF DATA QUALITY **118**

6.1 MODEL DEVELOPMENT 118
6.2 HYSPLIT MODEL AOD DATA QUALITY AUDIT 119
6.3 MAIAC SATELLITE AOD DATA QUALITY AUDIT 120

7. CONCLUSIONS AND RECOMMENDATIONS **121**

8. REFERENCES 123
APPENDIX A. - CHEMICAL SPECIATION 128
APPENDIX B – CAMX V1.5 WILDFIRE-ONLY VS. HYSPLIT 131
APPENDIX C – CAMX V1.5 VS. MAIAC 136

List of Figures

Figure 1.	Illustration of the burned area determination used in the FINNv2 preprocessor: (a) active fire detections, (b) burned area per detection, (c) detection clusters are joined for the determination of burned area.	18
Figure 2.	Illustration of the land cover determination in the FINNv2 preprocessor: (a) the burned area is subdivided to approximately 1 to 3 km2 polygons, overlaid onto the land cover raster (shown in the background) and (b) land cover for subdivided polygon is identified by the majority type.	20
Figure 3.	Spatial distribution of land cover in North America.	21
Figure 4.	MOD44B v006 MODIS/Terra VCF product for 2012 showing (a) percent tree cover, (b) percent non-tree cover, and (c) percent non-vegetated (bare)	22
Figure 5.	Spatial distribution of fuel loadings in the North American region of FINN v2.2.	27
Figure 6.	CAMx 36km (black)/12km (blue)/4km (green) nested modeling grids.	33
Figure 7.	Temporal profiles applied to fire emissions in the EPSv3.22 processing stream based on the approaches of the WRAP-FEJF and Randerson et al. (2012).	38
Figure 8.	(a) Diurnal profile of the vertical distribution of the fire plumes and (b) the fraction of hourly emissions allocated to CAMx vertical layer 1 in each of the five fire classes defined by daily area burned within each fire complex. Classes are defined by the area burned, less than 10 acres (class 1), 10 to 100 acres (class 2), 100 to 1000 acres (class 3), 1000 to 5000 acres (class 4), greater than 5000 acres (class 5).	39
Figure 9.	Receptor domain used for HYSPLIT modeling; the full map area covers 6° N to 41° N Latitude and 57° W to 124° W Longitude. Fire screening was applied in the outer domain, domain 1 (red), and domain 2 (purple). No screening was performed in domain 3 (green).	42
Figure 10.	FINNv2.2 global regions.	44
Figure 11.	Monthly total CO emissions (Tg/month) during 2016 (solid) and 2018 (dashed) from FINNv2.2 with MODIS and VIIRS active fire detections: (a) North America, (b) Central America, (c) South America, (d) Oceania, (e) Northern Africa, (f) Southern Africa, (g) Western Europe, (h) Eastern Europe, (i) Near East, (j) North Central Asia, (k) East Asia, and (l) Southern Asia. Note differences in scales between plots.	45
Figure 12.	Annual total PM2.5 emissions (kg/km2) in (a) 2016 and (b) 2018.	48
Figure 13.	Mexico and U.S. states grouped by subregion.	49
Figure 14.	Annual trends in monthly total PM2.5 emissions (Gg/mo) during 2012 through 2018 for (a) Texas, (b) Mexico, and (c) Western U.S., (d) Lower Mississippi Valley and (e) southeastern U.S.	50
Figure 15.	Annual trends in monthly total NOx emissions (Gg/month) during 2012 through 2018 for (a) Texas, (b) Mexico, and (c) Western U.S., (d) Lower Mississippi Valley and (e) southeastern U.S.	53
Figure 16.	Monthly total (a) PM2.5, (b) NOx and (c) NMOC emissions estimates during 2016 in Texas by FINNv.1.5, FINNv2.2 with MODIS only fire detections, and FINNv2.2 with MODIS and VIIRS fire detections.	57
Figure 17.	Total PM2.5 emissions (Mg/km2/mo) in February 2016 from FINNv.1.5, FINNv2.2 with MODIS only fire detections, and FINNv2.2 with MODIS and VIIRS fire detections.	58
Figure 18.	Contribution of land cover type to area burned, biomass loading, and total monthly CO, NMOC, NOx, and PM2.5 emissions in Texas from FINN v2.2 with MODIS only or in	59

combination with VIIRS fire detections during (a) February and (b) September 2016. Contributions are normalized by the values for FINNv1.5. Land cover types shown for Texas include tropical forest, temperate forest, evergreen forest, shrublands, grasses, and croplands.
Figure 19. Monthly total (a) PM2.5, (b) NOx and (c) NMOC emissions estimates during 2016 in the Southeastern U.S. and Lower Mississippi Valley by FINNv.1.5, FINNv2.2 with MODIS only fire detections, and FINNv2.2 with MODIS and VIIRS fire detections. 60
Figure 20. March monthly total PM2.5 emissions (Mg/km2/mo) in the Southeastern U.S. and Lower Mississippi Valley from FINNv.1.5, FINNv2.2 with MODIS only fire detections, and FINNv2.2 with MODIS and VIIRS fire detections. 61
Figure 21. Contribution of land cover type to area burned, biomass loading, and total monthly CO, NMOC, NOx, and PM2.5 emissions in the Southeastern U.S. and Lower Mississippi Valley from FINN v2.2 with MODIS only or in combination with VIIRS fire detections during (a) March and (b) September 2016. Contributions are normalized by the values for FINNv1.5. Land cover types shown include tropical forest, temperate forest, evergreen forest, shrublands, grasses, and croplands. 62
Figure 22. Monthly total (a) PM2.5, (b) NOx and (c) NMOC emissions estimates in 2016 in Mexico by FINNv.1.5, FINNv2.2 with MODIS only fire detections, and FINNv2.2 with MODIS and VIIRS fire detections. Note differences in scales between plots. 63
Figure 23. May monthly total PM2.5 emissions (Mg/km2/mo) in Mexico from FINNv.1.5, FINNv2.2 with MODIS only fire detections, and FINNv2.2 with MODIS and VIIRS fire detections. 64
Figure 24. Contribution of land cover type to area burned, biomass loading, and total monthly CO, NMOC, NOx, and PM2.5 emissions in Mexico from FINN v2.2 with MODIS only or in combination with VIIRS fire detections during May 2016. Contributions are normalized by the values for FINNv1.5. Land cover types shown include tropical forest, temperate forest, evergreen forest, shrublands, grasses, and croplands. 65
Figure 25. Correlation between HYSPLIT PM2.5 concentrations and IMPROVE TC concentrations for 10 IMPROVE sites in and around Texas. July through September values were chosen to better compare with wildfire season. 73
Figure 26. Comparison of daily sum HYSPLIT PM2.5 to IMPROVE TC at Big Bend, TX (left), and Wichita Mountains, OK (right), for 2012 through 2017. Linear regression equations and R2 values for each comparison are shown at the top of the figure. 74
Figure 27. Domain-wide HYSPLIT AOD values (mean model AOD - left) and MAIAC AOD values (mean observed AOD – bottom) for 2012–2017. Linear regression equations and R2 values for each comparison are shown at the top of the figure. 76
Figure 28. Domain-wide HYSPLIT vs. MAIAC AOD correlation coefficients for 2012 - 2017. 77
Figure 29. Domain-wide FB histogram of HYSPLIT vs. MAIAC AOD values for 2012-2017. 78
Figure 30. Domain-wide NMSE histogram of HYSPLIT vs. MAIAC AOD values for 2012-2017. 79
Figure 31. Domain-wide bugle plots of HYSPLIT vs. MAIAC AOD values for 2012-2017 are shown. The fractional bias bugle plot is shown on the left, while the fraction error bugle plot is shown on the right. 79
Figure 32. Domain-wide Q-Q plots of HYSPLIT (mean model AOD - left) and MAIAC (mean observational AOD - right) AOD values for 2012-2017. 80
Figure 33. A domain-wide soccer plot of normalized mean error vs. normalized mean bias for HYSPLIT vs. MAIAC AOD data during 2012-2017. Values are colored by the maximum 80

HYSPLIT AOD value in the domain to assess the influence of wildfire smoke on bias and error between the two datasets.
Figure 34. HYSPLIT vs. MAIAC Correlation Coefficient for 2012-2017 shown in top panel. The red line indicates a 3 day moving average of hourly correlation coefficients. Daily sum FINN v2.2 PM2.5 fire emissions are shown in the bottom panel. 81
Figure 35. Monthly HYSPLIT vs. MAIAC Correlation Coefficients are shown on the left. Monthly FINN v2.2 emissions are shown on the right for 2012-2017. 81
Figure 36. Domain-wide HYSPLIT AOD values (mean model AOD - left) and CAMx v2.2 WF-only AOD values (mean observed AOD – bottom) for 2012. Linear regression equations and R2 values for each comparison are shown at the top of the figure. 82
Figure 37. Domain-wide HYSPLIT vs. CAMx v2.2 WF-only AOD correlation coefficients for 2012. 83
Figure 38. Domain-wide FB histogram of HYSPLIT vs. CAMx v2.2 WF-only AOD values for 2012. 83
Figure 39. Domain-wide NMSE histogram of HYSPLIT vs. CAMx v2.2 WF-only AOD values for 2012. 84
Figure 40. Domain-wide bugle plots of HYSPLIT vs. CAMx v2.2 WF-only AOD values for 2012. The fractional bias bugle plot is shown on the left, while the fraction error bugle plot is shown on the right. 84
Figure 41. Domain-wide Q-Q plots of HYSPLIT (mean model AOD – left) and CAMx v2.2 (mean observational AOD – right) WF-only AOD values for 2012. 85
Figure 42. A domain-wide soccer plot of normalized mean error vs. normalized mean bias for HYSPLIT vs. CAMx v2.2 WF-only AOD data during 2012. Values are colored by the maximum HYSPLIT AOD value in the domain to assess the influence of wildfire smoke on bias and error between these two datasets. 86
Figure 43. Domain-wide CAMx v2.2 AOD values (mean model AOD - left) and MAIAC AOD values (mean observed AOD – bottom) for 2012. Linear regression equations and R2 values for each comparison are shown at the top of the figure. 89
Figure 44. Domain-wide FB histogram of MAIAC vs. CAMx v2.2 AOD values for 2012. 90
Figure 45. Domain-wide NMSE histogram of MAIAC vs. CAMx v2.2 AOD values for 2012. 90
Figure 46. Domain-wide bugle plots of MAIAC vs CAMx v2.2 AOD values for 2012. The fractional bias bugle plot is shown on the left, while the fraction error bugle plot is shown on the right. 91
Figure 47. Domain-wide Q-Q plots of CAMx v2.2 (mean model AOD - left) and MAIAC (mean observational AOD - right) AOD values for 2012. 91
Figure 48. A domain-wide soccer plot of normalized mean error vs. normalized mean bias for MAIAC vs. CAMx v2.2 AOD data during 2012. Values are colored by the maximum CAMx v2.2 WF-only AOD value in the domain to assess the influence of wildfire smoke on bias and error between these two datasets. 92
Figure 49. MAIAC vs. CAMx v2.2 monthly average cell-based FAC2 values for June 2012. 93
Figure 50. MAIAC vs. CAMx v2.2 monthly average cell-based R2 values for June 2012. 93
Figure 51. MAIAC (green) versus total CAMx v2.2 (red) and total CAMx v1.5 (blue) hourly domain-averaged AOD for 2012. 94

Figure 52. MAIAC observed AOD (bottom) vs. CAMx v2.2 (left, blue) and CAMx v1.5 (left, green) for all hourly 2012 values. 95
Figure 53. MAIAC observed AOD (bottom) vs. CAMx v2.2 (left, blue) and CAMx v1.5 (left, green) values for hourly WF-only events (filtered by CAMx WF-only 75th percentile) in 2012. 96
Figure 54. HYSPLIT (left), CAMx v2.2 wildfire-only (middle), and MAIAC (right) AOD values for September 19, 2012 at 17:00 Z. HYSPLIT data is at 50 km resolution, while CAMx and MAIAC data is at 4 km resolution. Light grey area indicates areas outside of the boundaries of MAIAC/CAMx data. Dark grey indicates areas with no AOD values within the HYSPLIT, CAMx, and MAIAC boundaries. 100
Figure 55. CAMx v2.2 wildfire-only AOD values (shown in blue) and CAMx v1.5 wildfire-only AOD values (shown in green) plotted versus MAIAC observed AOD on September 19, 2012, at 17:00 Z. The background cut-off for CAMx is 0.05. The subset area is 95°-100° W Longitude and 30°-34° N Latitude. Linear regression equations and R2 values for each comparison are shown at the top of the figure in the respective model color. 101
Figure 56. HYSPLIT (left), CAMx v2.2 wildfire-only (middle), and MAIAC (right) AOD values for September 20, 2012, at 19:00 Z. HYSPLIT data is at 50 km resolution, while CAMx and MAIAC data is at 4 km resolution. Light grey indicates areas outside of the boundaries of MAIAC/CAMx data. Dark grey indicates areas with no AOD values within the HYSPLIT, CAMx, and MAIAC boundaries. 102
Figure 57. CAMx v2.2 AOD values (shown in blue) and CAMx v1.5 wildfire-only AOD values (shown in green) versus MAIAC observed AOD on September 20, 2012, at 19:00 Z. Linear regression equations and R2 values for each comparison are shown at the top of the figure in the respective model color. 103
Figure 58. CAMx v2.2 wildfire-only AOD values (shown in blue) and CAMx v1.5 wildfire-only AOD values (shown in green) are plotted versus MAIAC observed AOD on September 20, 2012, at 19:00 Z. The background cut-off for CAMx is 0.1. The subset area is 90°-95° W Longitude and 29°-34° N Latitude. Linear regression equations and R2 values for each comparison are shown at the top of the figure in the respective model color. 104
Figure 59. HYSPLIT (left), CAMx v2.2 wildfire-only (middle), and MAIAC (right) AOD values are shown for September 21, 2012, at 18:00 Z. HYSPLIT data is at 50 km resolution, while CAMx and MAIAC data is at 4 km resolution. Light grey area indicates area outside of the boundaries of MAIAC/CAMx data. Dark grey indicates areas with no AOD values within the HYSPLIT, CAMx, and MAIAC boundaries. 105
Figure 60. CAMx v2.2 wildfire-only AOD values (shown in blue) and CAMx v1.5 wildfire-only AOD values (shown in green) are plotted vs. MAIAC observed AOD on September 21, 2012, at 18:00 Z. The background cut-off for CAMx is 0.2. The subset area is 90°-100° W Longitude and 29°-34° N Latitude. Linear regression equations and R2 values for each comparison are shown at the top of the figure in the respective model color. 106
Figure 61. HYSPLIT (left), CAMx v2.2 wildfire-only (middle), and MAIAC (right) AOD values are shown for September 22, 2012, at 18:00 Z. HYSPLIT data is at 50 km resolution, while CAMx and MAIAC data is at 4 km resolution. Light grey area indicates area outside of the boundaries of MAIAC/CAMx data. Dark grey indicates areas with no AOD values within the HYSPLIT, CAMx, and MAIAC boundaries. 107
Figure 62. CAMx v2.2 wildfire-only AOD values (shown in blue) and CAMx v1.5 wildfire-only AOD values (shown in green) are plotted vs. MAIAC observed AOD on September 22, 2012, at 18:00 Z. The background cut-off for CAMx is 0.2. The subset area is 92°-101° W 108

Longitude and 29°-34° N Latitude. Linear regression equations and R2 values for each comparison are shown at the top of the figure in the respective model color.
Figure 63. HYSPLIT (left), CAMx v2.2 wildfire-only (middle), and MAIAC (right) AOD values are shown for September 23, 2012, at 18:00 Z. HYSPLIT data is at 50 km resolution, while CAMx and MAIAC data is at 4 km resolution. Light grey area indicates area outside of the boundaries of MAIAC/CAMx data. Dark grey indicates areas with no AOD values within the HYSPLIT, CAMx, and MAIAC boundaries. 109
Figure 64. CAMx v2.2 wildfire-only AOD values (shown in blue) and CAMx v1.5 wildfire-only AOD values (shown in green) are plotted versus MAIAC observed AOD on September 23, 2012, at 18:00 Z. The background cut-off for CAMx is 0.05. The subset area is 90°-96° W Longitude and 29°-33° N Latitude. Linear regression equations and R2 values for each comparison are shown at the top of the figure in the respective model color. 110
Figure 65. HYSPLIT (left), CAMx v2.2 wildfire-only (middle), and MAIAC (right) AOD values are shown for September 24, 2012, at 17:00 Z. HYSPLIT data is at 50 km resolution, while CAMx and MAIAC data is at 4 km resolution. Light grey area indicates area outside of the boundaries of MAIAC/CAMx data. Dark grey indicates areas with no AOD values within the HYSPLIT, CAMx, and MAIAC boundaries. 111
Figure 66. CAMx v2.2 wildfire-only AOD values (shown in blue) and CAMx v1.5 wildfire-only AOD values (shown in green) are plotted vs. MAIAC observed AOD on September 24, 2012, at 17:00 Z. The background cut-off for CAMx is 0.1. The subset area is 90°-94° W Longitude and 30°-33° N Latitude. Linear regression equations and R2 values for each comparison are shown at the top of the figure in the respective model color. 112
Figure 67. HYSPLIT (left), CAMx v2.2 wildfire-only (middle), and MAIAC (right) AOD values are shown for September 26, 2012, at 19:00 Z. HYSPLIT data is at 50 km resolution, while CAMx and MAIAC data is at 4 km resolution. Light grey area indicates area outside of the boundaries of MAIAC/CAMx data. Dark grey indicates areas with no AOD values within the HYSPLIT, CAMx, and MAIAC boundaries. 113
Figure 68. CAMx v2.2 wildfire-only AOD values (shown in blue) and CAMx v1.5 wildfire-only AOD values (shown in green) are plotted vs. MAIAC observed AOD on September 26, 2012 at 19:00 Z. The background cut-off for CAMx is 0.05. The subset area is 90°-93° W Longitude and 30°-33° N Latitude. Linear regression equations and R2 values for each comparison are shown at the top of the figure in the respective model color. 114
Figure 69. HYSPLIT (left), CAMx v2.2 wildfire-only (middle), and MAIAC (right) AOD values are shown for June 27, 2012, at 17:00 Z. HYSPLIT data is at 50 km resolution, while CAMx and MAIAC data is at 4 km resolution. Light grey area indicates area outside of the boundaries of MAIAC/CAMx data. Dark grey indicates areas with no AOD values within the HYSPLIT, CAMx, and MAIAC boundaries. 115
Figure 70. CAMx v2.2 AOD values (shown in blue) and CAMx v1.5 wildfire-only AOD values (shown in green) are plotted vs. MAIAC observed AOD on June 27, 2012, at 17:00 Z. Linear regression equations and R2 values for each comparison are shown at the top of the figure in the respective model color. 116
Figure 71. CAMx v2.2 wildfire-only AOD values (shown in blue) and CAMx v1.5 wildfire-only AOD values (shown in green) are plotted vs. MAIAC observed AOD on June 27, 2012, at 17:00 Z. The background cut-off for CAMx is 0.1. The subset area is 91°-97° W 117

Longitude and 30°-33° N Latitude. Linear regression equations and R2 values for each comparison are shown at the top of the figure in the respective model color.

List of Tables

Table 1.	Emission factors by land cover type and chemical species for FINN v1.5 and v2.2 (g kg biomass burned−m).	25
Table 2.	Fuel loadings (g m−u) assigned by land cover type and global region. These values are based on the average of the two model estimates from Table 2 of Hoelzemann et al. (2004) as described Wiedinmyer et al. (2011) unless noted otherwise. Highlighted values indicate those updated for FINN v.2.2 based on Leeuwen et al. (2014).	28
Table 3.	North American biomass loadings (g m−2) by land cover type for coarse/woody and herbaceous vegetation. These values are based on the Fuel Characteristic Classification System (https://www.fs.fed.us/pnw/fera/fccs/) with the exceptions of croplands.	30
Table 4.	Mapping between WRF and CAMx model vertical layer structures.	34
Table 5.	Default model configuration and input data for the 2012 CAMx modeling episode.	36
Table 6.	Fire screening domains. Fires smaller than the Fire Site Threshold after clustering were removed from the fire emissions dataset prior to HYSPLIT dispersion modeling.	41
Table 7.	HYSPLIT configuration parameters.	41
Table 8.	Fractionated PM2.5 assumed for HYSPLIT AOD calculations.	43
Table 9.	AOD QA definitions and quality flags used to screen AOD retrievals for subsequent use. AOD values were retained for retrievals with quality flags shown in bold.	68
Table 10.	IMPROVE Sites used for TC analysis with HYSPLIT PM2.5. The IMPROVE site code is shown on the left, and the EPA site code is shown on the right.	72
Table 11.	MAIAC vs. HYSPLIT AOD model comparison statistics. Monthly values are averaged over all years in which monthly data is available (2012 – 2017). Values are provided with ± one standard deviation.	75
Table 12.	HYSPLIT vs. CAMx v2.2 WF-only AOD Model Comparison Statistics are shown. Monthly values are averaged hourly data for 2012. Values are provided with ± one standard deviation.	82
Table 13.	MAIAC vs. CAMx v2.2 AOD model comparison statistics. Monthly values are averaged hourly data for 2012. Values are provided with ± one standard deviation.	88
Table 14.	Execution wall clock time (hours) by geographic extent and model year (with active fire feature count).	118

Acknowledgments

The preparation of this presentation was funded by a grant from the Texas Air Quality Research Program (AQRP) at The University of Texas at Austin through the Texas Emission Reduction Program (TERP) and the Texas Commission on Environmental Quality (TCEQ). The findings, opinions and conclusions are the work of the author(s) and do not necessarily represent findings, opinions, or conclusions of the AQRP or the TCEQ.

Executive Summary

Wildland fires and open burning are substantial sources of ozone precursors, particulate matter, and greenhouse gases. Fire emissions and their transport and chemical processing influence air quality, climate, and human health across a range of temporal and spatial scales. Air quality in Texas can be affected by fire events that occur locally, regionally, or across longer distances from within the United States or across international borders with Canada, Mexico, or Central America.

The FINN modeling system was developed as a global-scale fire emissions model to estimate the daily emissions of trace gases and particles from open biomass burning. It was designed to support atmospheric chemical transport modeling, including consistent, high temporal and spatial resolution across local to global scales and chemical speciation of compounds for common atmospheric chemical mechanisms. Since its initial release in 2010, the model and its applications have continued to evolve, which has culminated in the development of FINNv2.2.

The FINNv2.2 modeling system consists of three primary components that include the preprocessor, emissions model, and chemical speciation code. Its development addresses improvements needed to earlier versions, particularly in the detection of smaller fires and the estimation of area burned. The model incorporates recent data products and/or scientific findings for active fire detections, land cover characterization, biomass loadings, emission factors, and chemical speciation of emissions.

Global simulations for 2016 and 2018 highlighted the effects of fire activity on emissions estimates for different regions of the world, as well as the interannual variability of emissions between the 2016 and 2018 fire seasons. Emissions estimates were developed for 2012 through 2018 for North America. In Texas during this time span, years with relatively higher peaks in emissions, which typically occurred in the late winter/spring, included 2013 and 2016, 2017, and in particular 2018 as shown in Figure ES1.

During 2016, which is the base year for the national Collaborative Emissions Modeling Platform, fire activity in Texas primarily occurred during the winter/spring months with peak emissions in February, as well as the late summer/fall with peak emissions in September. $PM_{2.5}$, NO_x, and non-methane organic compounds (NMOC) emissions exhibited the same seasonal patterns. Grasslands had a greater contribution to fire activity in February 2016 than September 2016. Forests provided smaller contributions to total area burned and NO_x emissions than grasses or shrublands in Texas but had more pronounced influences on emissions of $PM_{2.5}$ and especially NMOC.

Several significant changes occurred between FINNv1.5 and v2.2. Overall the changes led to increases in emissions of $PM_{2.5}$, NO_x and NMOC with v2.2 in Texas during 2016. It is difficult to capture the full complexity of the interactions between model parameters that contribute to variations emissions estimates for any given fire event or between different fire events. However, it is evident that the new algorithm implemented in FINNv2.2 to address the limitations in the burned area assumptions of previous versions and the inclusion of active fire detections from

Figure ES1. Annual trends in monthly total $PM_{2.5}$ emissions (Gg/mo) from FINN v2.2 during 2012 through 2018 in Texas with active fie detections from the Visible Infrared Imaging Radiometer Suite (VIIRS) and Moderate Resolution Spectroradiometer (MODIS).

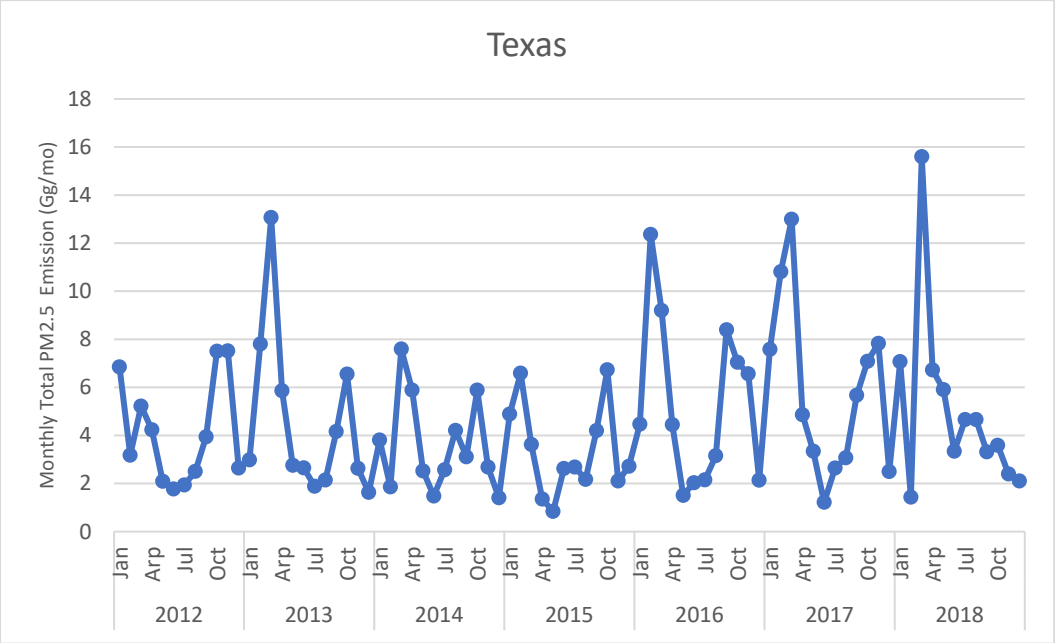

VIIRS, in addition to MODIS, have made important contributions to differences in emissions estimates. Transitions to more recent MODIS active fire detection and land cover data products, as well as biomass loadings from the USDA Forest Service FCCS, also play a role. Emission factors are similar between the model versions with the notable exception of NMOC. All measured NMOC is included in the applied emission factor for FINN v2.2 rather than only the identified NMOC fraction. This change dominates the contribution to differences in these emissions estimates between the model versions.

Results of the performance evaluation indicate that the modifications to FINN made between versions 1.5 and 2.2 have improved representation of wildfire smoke in the photochemical modeling results. Overall statistics for the CAMx model AOD comparison with satellite data indicate similar performance with the two versions of the emissions model. However, when smoke-dominated events were identified, the relationship between modeled and observed AOD improved for both FINN emissions versions. Furthermore, the case studies of smoke events show that model runs conducted with FINN v2.2 frequently showed better agreement with satellite observations of AOD relative to model runs conducted with FINN v1.5. These results indicate that the domain-wide statistics are dominated by variability in AOD unrelated to wildfire smoke. By focusing on high-smoke cases, we are able to identify and quantify notable improvements in model performance between FINN v1.5 and FINN v2.2. The evaluation performed here further demonstrate the value of emissions inventory assessment using satellite data.

It is recommended that FINNv2.2 continue to undergo evaluation across different regions of the world and that new findings from on-going field campaigns continue to be used to inform future evolution of the model.

1. Introduction

Wildland fires and open burning are substantial sources of ozone precursors, particulate matter, and greenhouse gases. Fire emissions and their transport and chemical processing influence air quality, climate, and human health across a range of temporal and spatial scales. Air quality in Texas can be affected by fire events that occur locally, regionally, or across longer distances from within the United States or across international borders with Canada, Mexico, or Central America. Crop residue burning for ground clearing and soil enrichment in Mexico's Yucatan Peninsula and Central America during the spring months is an annual recurrence that has had pronounced, well-documented impacts on Texas air quality (Wang et al, 2009; Villanueva-Fierro et al., 2009; McMillan et al, 2010; TCEQ, 2013; Wang et al, 2017). Fires that have been shown to exacerbate Texas air pollution levels have originated from the remote boreal forests of eastern Alaska and western Canada (Morris et al., 2006), from the Mississippi delta states of Arkansas, Louisiana, Mississippi (Westenbarger and Morris, 2018), and from drought-stressed areas within or close to Texas such as the western Oklahoma and Texas Panhandle fires during March 2017 and the Bastrop County Complex Fire in Central Texas during 2011. These events can lead to elevated pollutant levels in many of the state's most populous areas and pose risks to human health.

A myriad of factors contribute to the patterns and severity of biomass burning and emissions, including agricultural, forest, and waste management practices, land use change, climatic factors such as temperature and rainfall, drought status, and ecosystem diversity and health. Future climate, policy, and human behaviors may have profound and complex effects on the occurrence of fires. Schoennagel (2017) suggested that if trends in the increasing number and size of wildfires in western North America continue in the coming decades, policies that promote adaptive resilience of people and ecosystems to changing fire regimes will be needed to reduce future vulnerability.

Characterization of fire emissions is required to understand contributions to ambient concentrations and population exposure to pollutants such as ozone, toxics, and primary and secondary particulate matter. Emission estimates can support a weight of evidence for exceptional event demonstrations for wildfires that influence measured ozone concentrations and affect determinations of exceedances of the National Ambient Air Quality Standards (NAAQS). In the context of air quality planning and management, fire emissions can contribute to background ozone concentrations that influence the relative effectiveness of local and regional emissions controls.

The Fire Inventory from NCAR (FINN) was developed as a global fire emissions model that estimates daily emissions of trace gases and particles from open biomass burning (Wiedinmyer et al., 2011). It was designed to meet the needs of atmospheric chemical transport modeling, which include consistent, high temporal and spatial resolution across local to global scales and chemical speciation of compounds for common atmospheric chemical mechanisms. FINNv1 was released in 2010 (Wiedinmyer et al., 2011). FINNv1.5, was released in 2014, and the National Center for Atmospheric Research (NCAR) has served as the central repository for global emissions files spanning 2002-2018: http://bai.acom.ucar.edu/Data/fire/. Differences between versions 1 and 1.5 included updates to use the MODIS Collection 6 versus 5 product for fire detections, year-specific data for the MODIS Land Cover Type (LCT) and Vegetation Continuous Fields (VCF) products to identify land use/land cover classes and vegetation density,

respectively, and revisions to emissions factors for savanna, temperate and extratropical forest and chaparral. FINN has been applied in regions of the world that experience high fire activity to evaluate the influence of fire activity on air quality and public health (Nuryanto, 2015; Crippa et al., 2016; Ivey et al., 2014; Pimonsree et al., 2018), to examine the effects of changing climate and development patterns on wildfire emissions (Hurteau et al., 2014), and in comparisons with surface, aircraft and satellite-based observations (Stavrakou et al., 2016; Reddington et al., 2019) as well as with bottom-up inventories from other fire emission modeling systems (Larkin et al., 2014, Pereira, 2016; Urbanski et al., 2018). Real-time emissions estimates from FINNv1.0 are used in the Whole Atmosphere Community Climate Model (WACCM) real-time forecasts (http://www.acom.ucar.edu/waccm/forecast/). Emissions estimates from FINN have been used in air quality modeling for Texas ozone nonattainment areas conducted by the Texas Commission on Environmental Quality (TCEQ).

The objective of this work is to introduce the next generation of the FINN modeling system that is designated and publicly released as FINNv2.2. The Texas Air Quality Research Program (AQRP) has been instrumental in the ongoing development of FINN that has resulted in the development of this next generation model. Previous efforts have included AQRP Projects 12-018 (McDonald-Buller et al., 2013) and 14-011 (McDonald-Buller et al., 2015). Significant changes have been made in the approach to determining burned area and the underlying land cover from previous versions, as well as updates to fuel loadings, emission factors, and chemical speciation profiles based on recent literature. Global simulations for 2016 and 2018 highlight the effects of fire activity on emissions estimates for different regions of the world. Emissions estimates for North America were developed for 2012 through 2018, a time period that includes 2016, which is the base year for the national Collaborative Emissions Modeling Platform. FINNv2.2 performance was assessed using a new satellite algorithm, the Multi-Angle Implementation of Atmospheric Correction (MAIAC), for aerosol optical depth (AOD) retrievals, with a special focus on fire events that originate from within Mexico, Central America, or the Caribbean and influence Texas air quality.

2. Modeling System and Input Data Resources

As in previous versions, FINNv2.2 is based on the framework developed by Wiedinmyer et al. (2006). Emissions are estimated as

$$E_i = A(x,t) * B(x) * FB * ef_i \quad (1)$$

where E_i is the mass emission of species *i* (kg day^{-1}), A(x,t) is the area burned at time t and location x (km^2 day^{-1}), B(x) is the biomass (fuel) loading at location x (g m^{-2}), FB is the fraction of biomass burned, and ef_i is the emission factor of species *i* (g kg^{-1} biomass burned) (Wiedinmyer et al., 2011). All biomass terms are on a dry weight basis. The FINNv2.2 modeling system consists of three primary components that include the preprocessor, emissions model, and chemical speciation code. Each is described below along with the default input data resources.

2.1 Preprocessor

2.1.1 Active Fire Detections

The FINNv2.2 preprocessor was designed to estimate burned area from daily satellite detections of active fires and characterize the underlying land cover. In earlier version of FINN, global observations from the MODIS instruments on-board the National Aeronautics and Space Administration's (NASA's) Terra and Aqua satellites were used as the default for fire detection. FINNv2.2 adds the option to use active fire detections from VIIRS, onboard the Suomi National Polar-orbiting Partnership (Suomi-NPP), alone or in combination with MODIS active fire data.

The MODIS Collection 6 (MCD14DL) and VIIRS active fire products were obtained from the NASA's Fire Information for Resource Management System (FIRMS) data portal: https://firms.modaps.eosdis.nasa.gov/download/. Use of the MODIS product in FINNv2.2 follows that of earlier versions of the model (Wiedinmyer et al., 2011). The MODIS product provides daily fire detections with a nominal horizontal resolution of ~1 km^2 and the location, overpass time (UTC), and confidence of the detection. Data confidence is specified by a numeric scale of 0 to 100%. Detections with a confidence specification of less than 20% are eliminated from the analysis. Daily global coverage is not provided at latitudes between approximately 30° N and 30°S due to the observational swath path. Fire detections only in these equatorial regions are counted for a two-day period. Each fire is assumed to continue into the next day.

With its improved spatial resolution of 375m, the VIIRS product provides more sensitive detection of fires of relatively small areas, improved mapping of large fire perimeters, and improved nighttime performance relative to MODIS fire detections (NASA, 2019). The higher detection rates of small fires could be particularly important for areas of the world where agriculture burning is common. Detection confidence for the VIIRS product is specified by three categories, low/nominal/high. In the FINNv2.2 preprocessor, detections with a confidence specification identified as "low" are eliminated from the analysis. It should be noted that only the data (Type=0) attributed to thermal anomalies from vegetation fires (Type=0) were included, i,e.,

other thermal anomaly types associated with active volcanos or other static land sources had been filtered from the product.

The simultaneous use of two fire products in FINNv2 does not lead to double counting fires by the preprocessor algorithm. The algorithm determines the spatial union of all detections for a given day as the burned area of the fire, as described in the Section 2.1.2. The identity of the sensor is not relevant for the determination of burned area, as long as the pixel size for each detection is correctly represented (i.e., 0.14 km^2 for VIIRS and 1 km^2 for MODIS).

The active fire products report the time of date acquisition by Coordinated Universal Time (UTC). In contrast to previous versions of the model, the FINN v2.2 preprocessor uses local time in the specification of the date of a fire detection in order to facilitate comparisons of emissions estimates with observational data:

$$\text{Local Time} = \text{UTC} + \text{Nearest\_Integer}\ (\text{Longitude}/15) \quad (2)$$

2.1.2 Burned Area

Each reported active fire detection (Figure 1a) is assigned with a square area of 0.14 km^2 from VIIRS or 1 km^2 from MODIS (Figure 1b) based on the horizontal resolution of the data. The scan and track sizes of the satellite pixel for each fire detection are used to identify groups of records that represented contiguous detections. A rectangle with easterly and northerly sizes equal to 110% of the scan and track sizes is established for each detection ("detection rectangle"). Intersecting detection rectangles are associated with the detection of a single fire event by two contiguous satellite sensors or the detection of a fire in a nearby location by another satellite overpass. In either case, these overlapping records are assumed to be detections of the same fire event stretching across the area. A convex hull is generated between corresponding pairs of detection rectangles that directly intersect. Convex hulls from a cluster of detections are joined such that the resulting "fire polygon" is an estimate of the burned area for a single fire event for the day (Figure 1c).

Figure 1. Illustration of the burned area determination used in the FINNv2 preprocessor: (a) active fire detections, (b) burned area per detection, (c) detection clusters are joined for the determination of burned area.

(a)

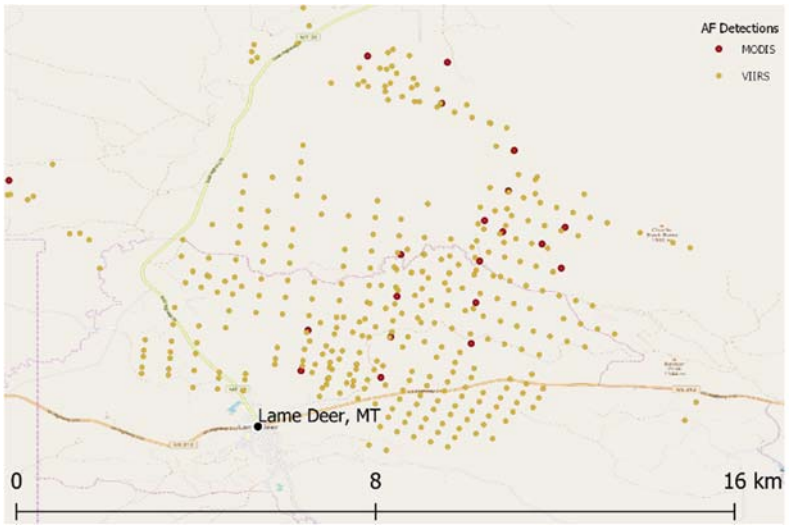

(b)

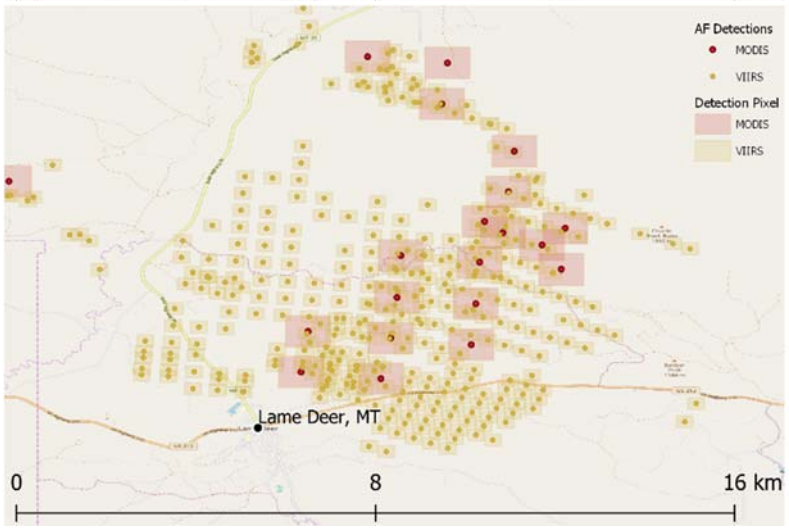

(c)

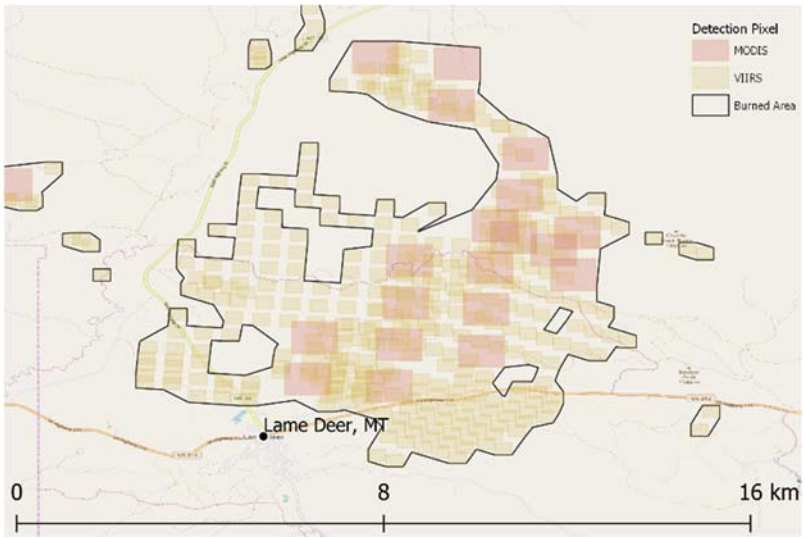

2.1.3 Land Cover Characterization

The burned area for each fire is subdivided to analyze the underlying land cover. FINNv2.2 uses the Terra and Aqua combined MODIS Land Cover Type (MCD12Q1) Version 6 data product with the International Geosphere-Biosphere Programme (IGBP) classification scheme (https://lpdaac.usgs.gov/products/mcd12q1v006/). Other land cover data could be used with FINN, as in McDonald-Buller et al. (2013). Year-specific data are used when available. If unavailable for most of the current year due to a lag in the LCT data release, the most recent data available are used.

For each fire polygon, the land cover characterization algorithm determines the distance between each detection point that is shorter than 0.5 arcminute (~1 km). Detection points are represented as nodes, and edges are weighted by the inverse distance. Each of the connected components is evaluated, and nodes are iteratively eliminated until no edges remained. For each node within the connected component, the sum of the weights of the edges (i.e., the inverse distance to neighboring nodes) is calculated. Nodes with the largest values are eliminated first; when this criterion includes more than one node, all nodes are replaced by the midpoint of the directly connected group. The fire polygon is divided into Voronoi tessellations using a subset of the fire detection coordinates. A raster is clipped based on the geometry of the subdivided fire polygon and the majority land cover type classification is determined (Figure 2).

Each of the 16 IGBP land cover classifications are mapped to a generic vegetation type, depending on the vegetation type and latitude that distinguish tropical, temperate and boreal forests. The generic vegetations types include grassland, shrubs, tropical forest, temperate forest, boreal forest, temperate evergreen forest, and crops (generic). Figure 3 shows the spatial distribution of land cover in North America.

The MODIS Vegetation Continuous Fields (VCF) product from NASA provides estimates of bare and vegetative cover. The map of bare cover from the MOD44B v006 MODIS/Terra VCF yearly product (https://lpdaac.usgs.gov/products/mod44bv006/) with a horizontal resolution of 250m, shown in Figure 4, is overlaid on the fire polygon. The VCF raster is clipped based on the geometry of the polygon, and the average VCF value is calculated for tree, grass, and bare cover.

Figure 2. Illustration of the land cover determination in the FINNv2 preprocessor: (a) the burned area is subdivided to approximately 1 to 3 km^2 polygons, overlaid onto the land cover raster (shown in the background) and (b) land cover for subdivided polygon is identified by the majority type.

(a)

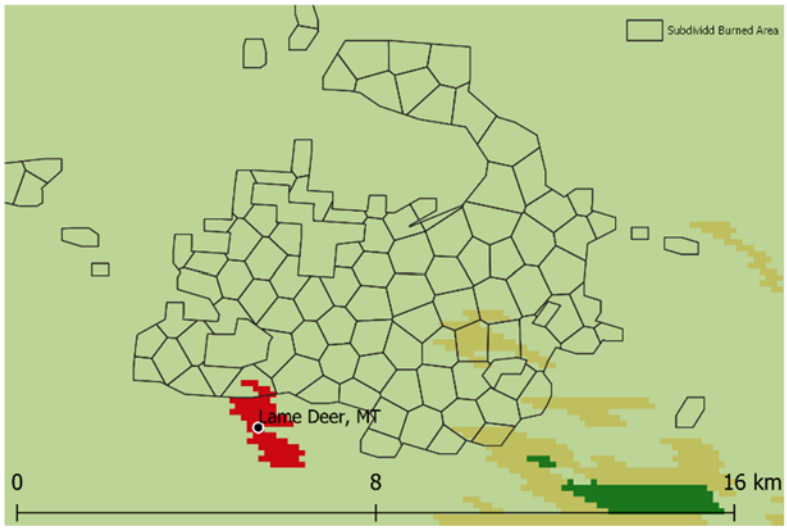

(b)

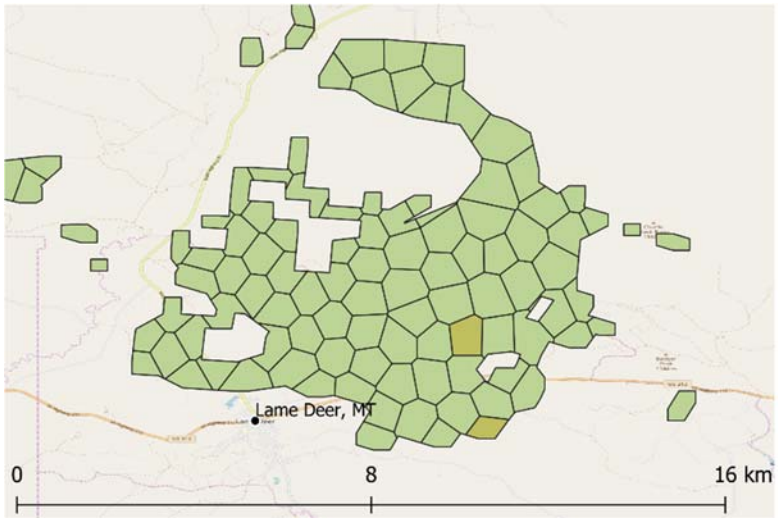

Figure 3. Spatial distribution of land cover in North America.

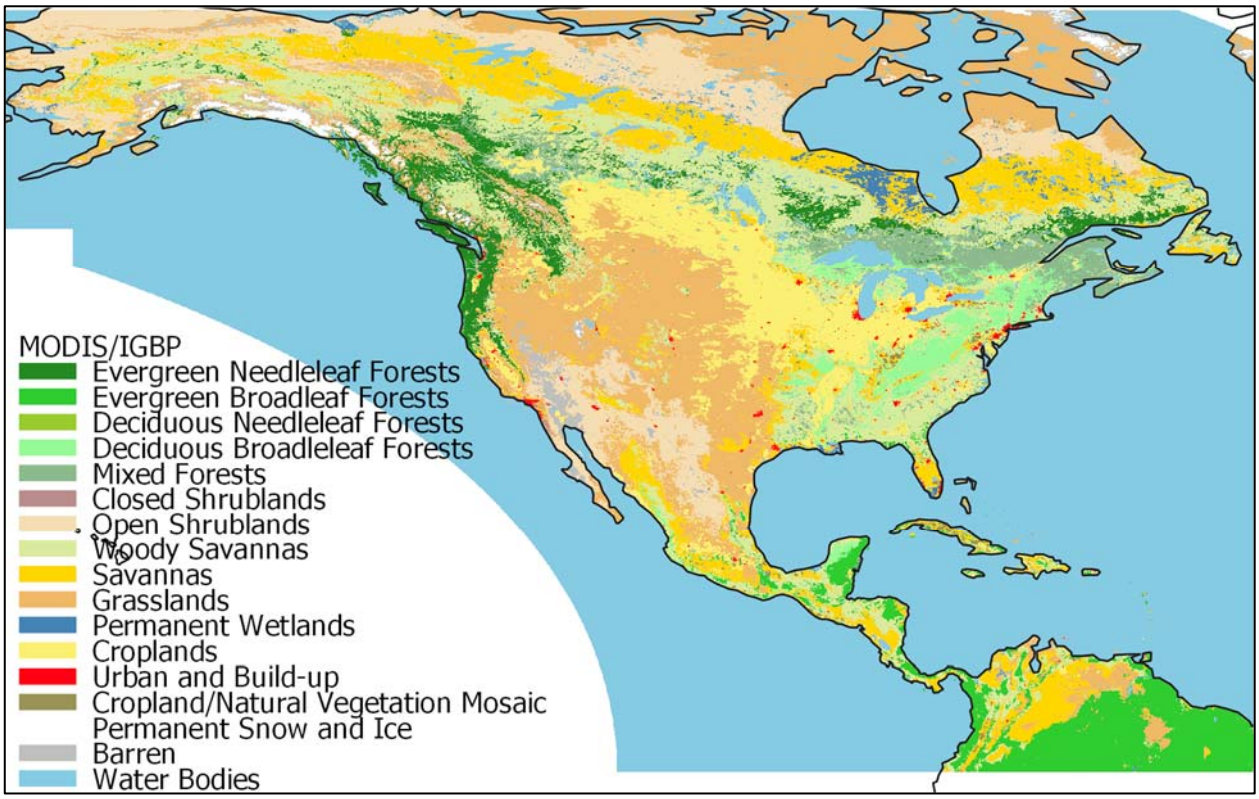

Figure 4. MOD44B v006 MODIS/Terra VCF product for 2012 showing (a) percent tree cover, (b) percent non-tree cover, and (c) percent non-vegetated (bare)

(a)

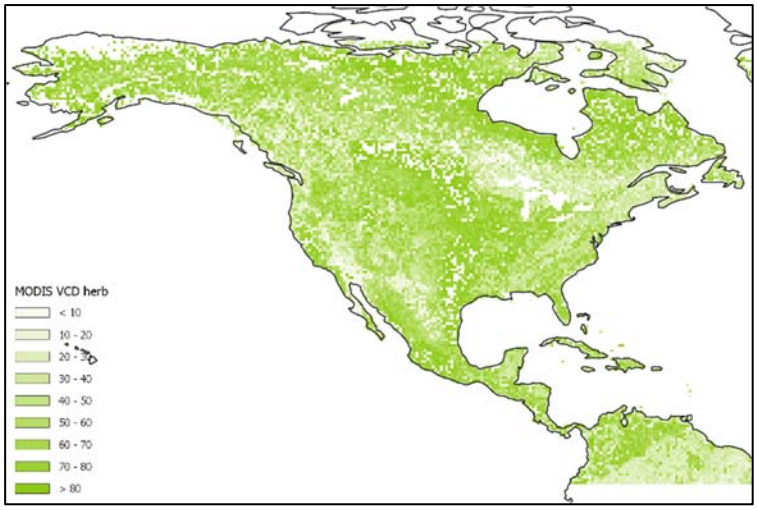

(b)

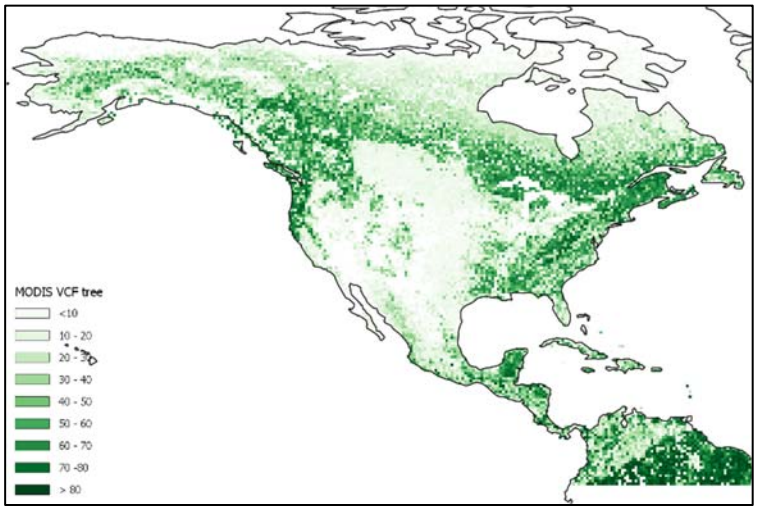

(c)

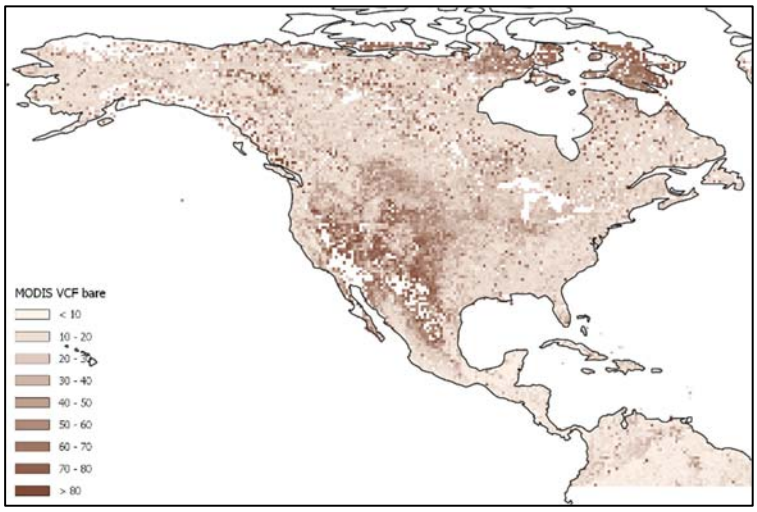

2.2 Emissions Model

The FINNv2.2 emissions model utilizes the burned area estimate and land cover characterization from the preprocessor with mappings of bare ground cover and fuel loadings, emission factors by land cover type, and estimates of the fraction of biomass burned to determine the mass emissions of chemical species (Equation 1).

2.2.1 Final Burned Area

The area of each polygon is assumed to be the area of the fire (burned area), unless the land cover type as defined by the MODIS LCT product is grass, or if bare ground or water is identified in that space. The final burned area is estimated as:

$$\text{Burned Area} = \begin{cases} \text{Polygon Area} & \text{if the land cover type is forest/shrub} \\ \text{Polygon Area} * 0.75 & \text{if the land cover type is savanna/grass} \\ 0 & \text{if the land cover type is bare/water} \end{cases} \quad (3)$$

2.2.2 Emission Factors and Chemical Speciation

Emission factors are assigned to each generic vegetation type (listed in Section 2.1.3). In earlier versions of the FINN framework, results from Akagi et al. (2011) provided tabulations of weighted average emission factors for different ecosystems and fuel types that became part of the framework for FINNv1 (Wiedinmyer et al., 2011). These tables were last updated in February 2015 and can be obtained from http://bai.acom.ucar.edu/Data/fire/. Emission factors in FINN have been updated concurrently with the updates in these tables. As part of AQRP Project 14-011, McDonald-Buller et al., 2015 added crop-specific emission factors for major crop types in the United States developed by McCarty (2011).

Although there have been many studies since the Akagi et al. 2015 update, a complete update to the Akagi tables is challenging and beyond the scope of this project. For the FINNv2.2 development, emission factors for temperate/boreal evergreen forests were updated with the Akagi et al. 2015 updates and reported emission factors from Liu et al (2017), Urbanski (2014), and Paton-Walsh (2014) (conifer forest results) and for croplands from Liu et al (2017), Fang et al. (2017), Santiago De La Rosa et al. (2018), Stockwell et al. (2015, Table S3). Crop-specific emission factors for the United States are not included here but could be added to FINN v2.2, as in McDonald-Buller et al. (2015). Emission factors used in FINN v1.5 and v2.2 are summarized in Table 1.

A notable difference in the emission factors used in FINN v2.2 relative to the earlier versions of FINN (e.g. Wiedinmyer et al, 2011) is that all measured NMOC is included in the applied emission factor rather than only the identified NMOC fraction. This reflects that identification of the NMOCs measured in emissions from fires has increased significantly in the time since Akagi et al. (2011), (e.g., Stockwell et al., 2015; Liu et al., 2016; Hatch et al., 2017). in FINNv1) and the contribution of unidentified compounds to the total mass of NMOC emissions. Overall, this

modification leads to a dramatic increase in the total NMOC emission factors for all vegetation types.

The total NMOC emissions need to be distributed to the surrogate species of a chemical mechanism in order to be input and used with a chemical transport model. Mapping of the NMOC emissions to three different chemical mechanisms (SAPRC99, MOZART-4, and GEOS-Chem) is presented by Wiedinmyer et al. (2011). For this project, an updated speciated mapping has been developed for the MOZART-T1 mechanism, shown in Table A1 of Appendix A. This mechanism is an update to the MOZART-4 mechanism and includes more species to which we can map the total NMOC. This mapping was done in part with the guidance from experts at NCAR who created the mechanism and will be called here MOZT1_map1.0. This is the first version of the mapping. Table A1 also includes mapping of FINN's particulate matter species to those of the CF particulate matter mechanism in CAMx.

2.2.3 Biomass Loading

Biomass loading, or the amount of fuel available to be burned, is a needed input and is assigned by land cover type and global region. For areas outside of the continental U.S., biomass loadings are assigned to each generic vegetation type and global region. Selected values were updated for FINN v2.2 based on van Leeuwen et al. (2014). The fuel loading for crops was updated to 902 g/m^2 based on an average from van Leeuwen et al. (2014), Akagi et al. (2011), and Pouliot et al. (2017). Specific crop types are not identified in this version.

Biomass loadings that can be burned by fuel type and global region are shown for FINNv.1.5 and FINNv2.2 in Table 2. Biomass loadings for FINN v1.5 match those presented by Wiedinmyer et al. (2011; refer to Table 2).

For North America, FINNv2.2 utilizes biomass loadings for coarse/woody and herbaceous vegetation by land cover type derived from the Fuel Characteristic Classification System (FCCS) of the U.S. Department of Agriculture Forest Service (https://www.fs.fed.us/pnw/fera/fccs/), as described in the final project report and addendum for AQRP 14-011 (http://aqrp.ceer.utexas.edu/projects.cfm). These biomass loadings, shown in Table 3, have priority over the regional default fuel loadings shown in Table 2. Biomass loadings for North America are shown in Figure 5.

2.2.4 Fraction of Biomass Burned

As in earlier version of the model, the fraction of biomass burned (FB) is determined as a function of tree cover based on the approach of Ito and Penner (2004). For areas with > 60% tree cover in the VCF product, FB is 0.3 for the woody fuel and 0.9 for the herbaceous cover. For areas < 40% tree cover, no woody fuel is assumed to burn, and the FB is 0.98 for the herbaceous cover. For fires in areas with 40% - 60% tree cover, the FB is 0.3 for woody fuels and is calculated as the following for herbaceous fuels: FB = exp (-0.13 × *fraction of tree cover*). The fraction of tree cover and fuel loading by land cover type are used to determine the amount of woody fuel available in each global region; herbaceous fuel loading is assumed to be identical to that of grasslands in each global region.

Table 1**.** Emission factors by land cover type and chemical species for FINN v1.5 and v2.2 (g kg biomass burned^{-1}).

Chemical Species	FINN v1.5 and FINN v2.2 Emission Factors by Land Cover Type (g kg biomass burned^{-1})													
	Tropical Forest[1]		Temperate Forest[2]		Temperate Evergreen Forest[2]		Boreal[3]		Woody Savannah[4]		Savanna and Grasslands[1]		Crops[5]	
	v1.5	v2.2	v1.5	v2.2	v1.5	v2.2	v1.5	v2.2	v1.5	v2.2	v1.5	v2.2	v1.5	v2.2
CO_2	1643	1643	1510	1510	1647	1623	1489	1565	1716	1681	1692	1686	1537	1444
CO	92	93	122	122	88	112	127	111	68	67	59	63	111	91
CH_4	5.1	5.1	5.61	5.61	3.36	3.4	6	6	2.6	3	1.5	2	6	5.82
NMOC[6]	26	51.9	28.5	56	23.5	49.3	29.3	48.5	4.8	24.8	9.3	28.2	57	51.4
H_2	3.4	3.4	2	2	2	2	2.3	2.3	0.97	0.97	0.97	1.7	2.4	2.59
NO_x as NO	2.6	2.6	1.04	1.04	1.92	1.96	0.9	0.95	3.9	3.65	2.8	3.9	3.5	2.43
SO_2	0.4	0.4	1.1	1.1	1.1	1.1	1	1	0.68	0.68	0.48	0.9	0.4	0.4
$PM_{2.5}$	9.1	9.9	15	15	12.9	17.9	15.3	18.4	9.3	7.1	5.4	7.17	5.8	6.43
TPM	18.5	18.5	18	18	18	18	18	18.4	15.4	15.4	8.3	8.3	13	13
TPC	5.2	5.2	9.7	9.7	9.7	9.7	8.3	8.3	7.1	7.1	3	3	4	4
OC	4.7	4.7	7.6	7.6	7.6	7.6	7.8	7.8	6.6	3.7	2.6	2.6	3.3	2.66
BC	0.52	0.52	0.56	0.56	0.56	0.56	0.2	0.2	0.5	1.31	0.37	0.37	0.69	0.51

Chemical Species	FINN v1.5 and FINN v2.2 Emission Factors by Land Cover Type (g kg biomass burned^{-1})													
	Tropical Forest[1]		Temperate Forest[2]		Temperate Evergreen Forest[2]		Boreal[3]		Woody Savannah[4]		Savanna and Grasslands[1]		Crops[5]	
	v1.5	v2.2	v1.5	v2.2	v1.5	v2.2	v1.5	v2.2	v1.5	v2.2	v1.5	v2.2	v1.5	v2.2
NH_3	1.33	1.3	2.47	2.47	0.84	1.17	2.7	1.8	1.2	1.2	0.49	0.56	2.3	2.12
NO	0.91	0.9	0.34	0.95	0.34	0.95	1.5	0.83	1.4	0.77	0.74	2.16	1.7	1.18
NO_2	3.6	3.6	2.7	2.34	2.7	2.34	3	0.63	1.4	2.58	3.2	3.22	3.9	2.99
NMHC	1.7	1.7	5.7	5.7	5.7	5.7	5.7	5.7	3.4	3.4	3.4	3.4	7	7

[1]Emission factors for Tropical Forests, Savannah/Grasslands updated to average values from Akagi et al. 2011 (updated Feb. 2015)

[2]Emission factors for Temperate Forest and Temperate Evergreen Forests are average values from Akagi et al 2011 (updated Feb 2015) and results from Liu et al (2017), Urbanski (2014), and Paton-Walsh (2014). For Temperate Evergreen Forest, only results from evergreen forests included.

[3]Boreal Forest emission factors are average of Akagi et al 2011 (updated 2015) with emission factors from boreal emission factors from Urbanski et al. (2014)

[4]Woody Savannah (Shrubland) emission factors updated with values from Akagi et al. 2011 (updated Feb. 2015).

[5]Crop Emission factors updated with average values from Akagi et al (2011) updated Feb. 2015 and results from Liu et al (2017), Fang et al. (2017), Santiago De La Rosa et al. (2018), Stockwell et al. (2015, Table S3).

[6]NMOC emission factors now include identified and unidentified compounds.

Figure 5. Spatial distribution of fuel loadings in the North American region of FINN v2.2.

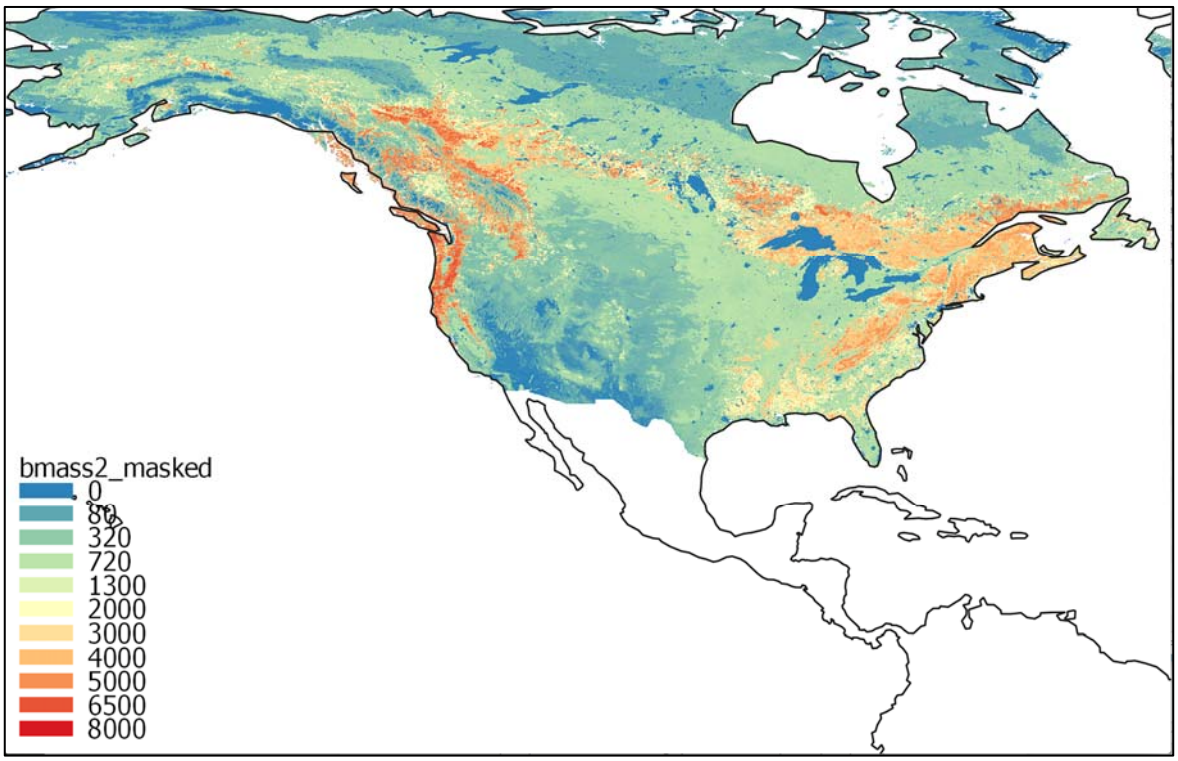

Table 2**.** Fuel loadings (g m^{-2}) assigned by land cover type and global region. These values are based on the average of the two model estimates from Table 2 of Hoelzemann et al. (2004) as described Wiedinmyer et al. (2011) unless noted otherwise. Highlighted values indicate those updated for FINN v.2.2 based on Leeuwen et al. (2014).

Global Region	Biomass Loading by Land Cover Type for FINN v1.5 and FINNv2.2 (g m^{-2})									
	Tropical Forest		Temperate Forest		Boreal Forest		Woody Savanna/ Shrublands		Savanna and Grasslands[g]	
	v1.5	v2.2	v1.5	v2.2	v1.5	v2.2	v1.5	v2.2	v1.5	v2.2
North America	28,076[b]	28,076	10,492	10,661[e]	25,000[a]	17,875[e]	5,705	4,762	976	976
Central America	20,260	26,500[e]	11,000[a]	11,000			2,224	2,224	418	418
South America	25,659	26,755[e]	7,400[a]	7,400			3,077	3,077	552	624[e]
Northern Africa	25,366	25,366	3,497	3,497			2,501	2,501	318	382[e]
Southern Africa	25,295	25,295	6,100	6,100			2,483	2,483	360	411[e]
Western Europe	28,076[b]	28,076	7,120	7,120	6,228	6,228	4,523	4,523	1,321	1,321
Eastern Europe	28,076[b]	28,076	11,386	11,386	8,146	8,146	7,752	7,752	1,612	1,612
North Central Asia	6,181[c]	6,181	20,807	20,807	25,000[a]	14,925[e]	11,009	11,009	2,170	2,170
Near East	6,181[c]	6,181	10,316	10,316			2,946	2,946	655	655

Global Region	Biomass Loading by Land Cover Type for FINN v1.5 and FINNv2.2 ($g\ m^{-2}$)									
	Tropical Forest		Temperate Forest		Boreal Forest		Woody Savanna/ Shrublands		Savanna and Grasslands[g]	
	v1.5	v2.2	v1.5	v2.2	v1.5	v2.2	v1.5	v2.2	v1.5	v2.2
East Asia	6,181[c]	14,941[e]	7,865	7,865			4,292	4,292	722	722
Southern Asia	27,969	26,546[e]	14,629	14,629			5,028	5,028	1,445	1,445
Oceania	16,376	16,376	11,696[d]	13,535[e]			1,271	2,483[f]	245	552[e]
Antarctica	0	0	0	0	0	0	0	0	0	0

[a] Akagi et al. (2011) and references therein; [b] tropical forest class added for North America and Europe (in LCT); [c] all Asia assigned equal tropical forest values; [d] taken as the average of tropical and temperate forest fuel loadings for Oceania; [e] van Leeuwen et al., 2014; [f] taken as the same for African woody savanna from van Leeuwen et al., 2014; [g] croplands assigned same biomass loading as grasslands.

Table 3**.** North American biomass loadings (g m−2) by land cover type for coarse/woody and herbaceous vegetation. These values are based on the Fuel Characteristic Classification System (https://www.fs.fed.us/pnw/fera/fccs/) with the exceptions of croplands[a].

Land Cover Type	Biomass Loading ($g\ m^{-2}$)	
	Coarse/Woody	Herbaceous
Water	0	0
Evergreen Needleleaf Forest	28,930	437
Evergreen Broadleaf Forest	19,917	650
Deciduous Needleleaf Forest	15,653	541
Deciduous Broadleaf Forest	19,982	964
Mixed Forests	20,339	766
Closed Shrublands	5,136	229
Open Shrublands	2,889	169
Woody Savannas	12,907	668
Savannas	10,907	764
Grasslands	2,822	407
Permanent Wetlands	8,509	712
Croplands	0	902[a]
Urban and Built-Up	0	0
Cropland/Natural Vegetation	9,080	822
Snow and Ice	0	0
Barren or Sparsely Vegetated	1,355	104

[a] Taken as an average from van Leeuwen et al. (2014), Akagi et al., (2011), and Pouliot et al. (2017)

2.3 Computing Environment

The FINNv2.2 modeling system has three primary components that include the preprocessor, emissions model, and chemical speciation code. It is in the preprocessing component of the code that the burned area polygons are created and merged with the associated land cover data. In earlier versions of the FINN model, preprocessing was accomplished in a piecemeal manner. The FINN v2.2 preprocessing algorithm was implemented in PostGIS, a database that supports geospatial data types and operations, which resulted in improved performance (i.e., shorter execution time) for the model. In order to facilitate portability, the Docker environment was selected to house the FINN preprocessor tools. Docker is an open source software development system platform (https://www.docker.com). It allows a developer to establish a Linux-based environment customized for the application that will run on multiple hosts such as Windows, MacOS, Linux. The Dockerfile, included as part of the FINN preprocessor, specifies the necessary libraries and applications, such as PostGIS and python. The output is a comma-delimited file characterizing burned area and underlying land cover for active fires for use with the FINN v2.2 emissions model.

For each fire point, fuel loadings and emissions factors are assigned based on region, land cover type and vegetation density within the emissions model. The emissions code utilizes this information with the input file created from the preprocessor to determine overall emissions for all fires. The output are emission estimates in units of mass per time in comma-delimited format. The emissions code is in IDL.

Output from the emissions model is postprocessed by the speciation model, the final component of the FINN framework. It allocates the total NMOC to the surrogate species of the MOZART-T1 mechanism. The output provides emission estimates in units of moles per time. As with the emissions mode in comma-delimited format. As with the code for the emissions model, the code for the chemical speciation algorithm is in IDL.

The FINNv2.2 code will be distributed through the NCAR GitHub (https://github.com/NCAR).

3. Air Quality Modeling

A photochemical modeling episode, developed by the TCEQ, was used to examine the effects of fires on air quality in North America and to support the assessment of FINN performance with the MAIAC AOD product. This section described the model configuration and spatial domain as well as the preprocessing conducted to prepare the chemically speciated FINN v2.2 emissions estimates for use as input to the model. At the time of this study, the TCEQ was conducting its air quality modeling for the 2012 base year. Thus, the implications of fire events on air quality during 2012 were the focus of this analysis.

3.1 CAMx Configuration

Air quality simulations were conducted with the Comprehensive Air Quality Model with Extensions (CAMx) for the May 1- October 1, 2012, time period, obtained from the TCEQ (https://www.tceq.texas.gov/airquality/airmod/data/tx2012. The modeling domain is shown in Figure 6. It includes a 36-km domain over the CONUS and southern Canada and northern Mexico, a 12-km domain covering Texas and most surrounding states, and a 4-km grid over eastern Texas. The vertical grid shown in Table 4 consists of 29 layers.

The TCEQ's base case with episode day-specific emissions was selected as the starting point for this project. Fire emissions from FINN v1.5 (GLOB_2012_02282013_MOZ4.txt) were processed by the TCEQ at the time of the episode development. These were retained in the default configuration of CAMx for this project and used as the basis for comparison with new emissions estimates from FINNv2.2. The processing of fire emissions estimates from FINN for use with CAMx is described in Section 3.2. Several changes were made to the TCEQ's base case configuration to obtain the default configuration used in this work. The CAMx version was updated from v6.31 to v.6.5. The gas-phase chemical mechanism was updated from TCEQ's default of CB6r2h to CB6r4. The particulate matter mechanism was also enabled. The model configuration and input data sources used in this project are summarized in Table 5.

Figure 6. CAMx 36km (black)/12km (blue)/4km (green) nested modeling grids.

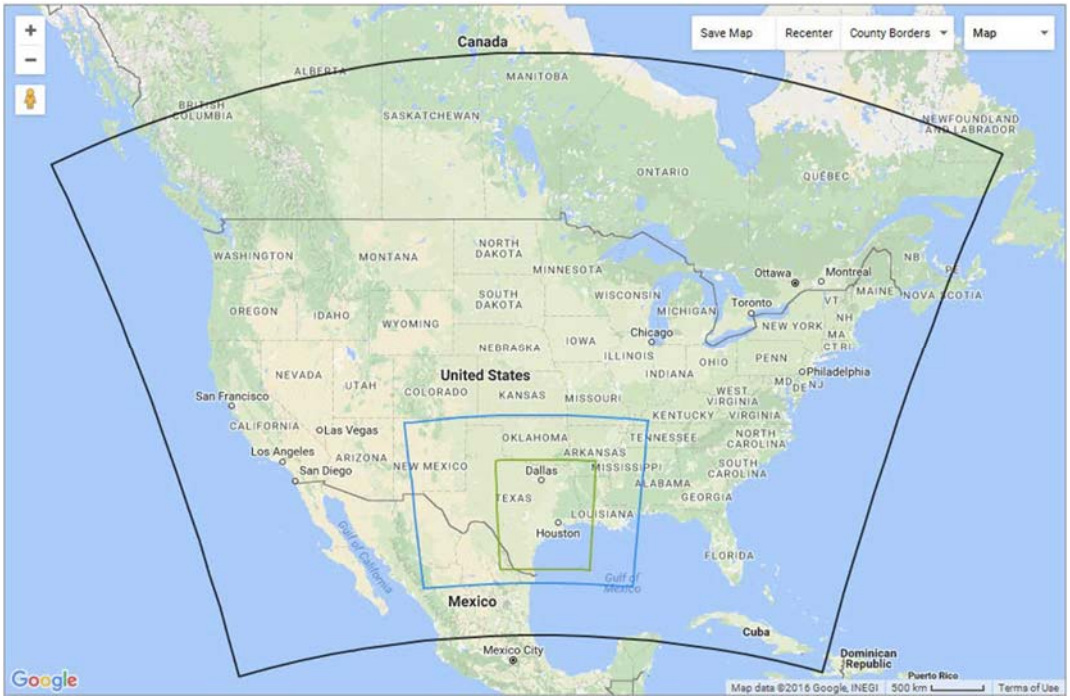

Source:https://www.tceq.texas.gov/assets/public/implementation/air/sip/hgb/HGB_2016_AD_RFP/AD_Adoption/16016SIP_HGB08AD_ado.pdf

Table 4**.** Mapping between WRF and CAMx model vertical layer structures.

CAMx Layer	WRF Layer	Top m (AGL)	Center m (AGL)	Thickness (m)
29	42	18250	16445	3611
28	39	14369	13632	2015
27	37	12624	10786	3675
26	33	8949	7891	2115
25	30	6833	6289	1088
24	28	5746	5290	911
23	26	4835	4449	772
22	24	4063	3704	717
21	22	3346	3175	341
20	21	3005	2840	330
19	20	2675	2515	320
18	19	2355	2225	259
17	18	2096	1969	253
16	17	1842	1718	248
15	16	1595	1474	242
14	15	1353	1281	143
13	14	1210	1140	141
12	13	1069	1000	139
11	12	930	861	138
10	11	792	747	91
9	10	702	656	90
8	9	612	567	89
7	8	522	478	89

CAMx Layer	WRF Layer	Top m (AGL)	Center m (AGL)	Thickness (m)
6	7	433	389	88
5	6	345	302	87
4	5	258	215	87
3	4	171	128	86
2	3	85	60	51
1	2	34	17	34

Source:https://www.tceq.texas.gov/assets/public/implementation/air/sip/hgb/HGB_2016_AD_RFP/AD_Adoption/16016SIP_HGB08AD_ado.pdf

Table 5. Default model configuration and input data for the 2012 CAMx modeling episode.

Model Component	Description
Modeling Period	May 1 – October 1, 2012
CAMx Version	6.5
Horizontal Domain	36km/12km/4km (Figure 6)
Vertical Structure	28 Vertical Layers (Table 6)
Meteorological Model	Weather Research and Forecast (WRF) v.3.7.1 with KVPATCH modification
Dry Deposition Scheme	Wesely
Chemical Mechanism	CB6r4 (Carbon Bond v6 revision 4) gas-phase mechanism CF_SOAP_ISORROPIA particulate matter mechanism (CF: coarse/fine size fraction, SOAP2.1: organic aerosol module, ISORROPIA: inorganic module)
Boundary and Initial Conditions	Goddard Earth Observing System Chemistry Model (GEOS-Chem)
Surface Characteristics (Topographic Elevation, Leaf Area Index (LAI), Vegetative Distribution, Water/Land Boundaries)	36-km domain: Biogenic Emissions Land use Database (BELD) v.3 outside the U.S., 2006 National Land Cover Dataset (NLCD) for U.S 4-km and 12-km domains: Popescu et al., 2012[a] LAI: Monthly average from the 8-day Moderate-Resolution Imaging Spectroradiometer (MODIS) MCD15A2 product
Emissions	Fires: FINNv1.5 (http://bai.acom.ucar.edu/Data/fire/,file GLOBAL_FINNv15_2012_MOZ4_7112014.txt) TCEQ 2012 “reg4a” for low-level sources and “reg6a” for elevated sources: Biogenic: BEIS v 3.61 Stationary Point Sources: EPA’s 2011 Modeling Platform, EPA’s Air Markets Program Database (AMPD), State of Texas Air Reporting System (STARS), U.S. Bureau of Ocean Energy Management 2011 Gulf-Wide Emissions Inventory; Environment Canada 2006 National Pollutant Release Inventory On-Road Mobile: MOVES2014 Nonroad Mobile: EPA’s National Mobile Inventory Model (NMIM), EPA’s 2011 National Emissions Inventory (NEI), Texas Air Emissions Repository (TexAER), Texas Nonroad Model (TexN), Federal Aviation Administration (FAA) Emissions Dispersion Modeling System (EDMS)

Model Component	Description
	Area: EPA's 2011 NEI, TexAER

Source:https://www.tceq.texas.gov/assets/public/implementation/air/sip/hgb/HGB_2016_AD_RFP/AD_Adoption/16016SIP_HGB08AD_ado.pdf

[a] Popescu, S. C., J. Stukey, M. Karnauch, J. Bowling, X. Zhang, W. Booth, N.-W. Ku, 2008, The New Central Texas Land Use Land Cover Classification Project, TCEQ Contract No. 582-5-64593-FY08-23, http://www.tceq.state.tx.us/assets/public/implementation/air/am/contracts/reports/oth/5820564593FY0823-20081230-tamu-New_Central_TX_LULC.pdf

3.2 Fire Emissions Processing

Processing of the fire emissions estimates from the FINN modeling system for use with CAMx was accomplished using version 3.22 of the Emission Processing System (EPS) (Ramboll, 2015). Several key aspects of the processing included chemical speciation of emissions from MOZART-T1, which is the output of the FINN modeling system, for the CB6r4 mechanism used in CAMx, as well as the temporal and vertical allocations of fire emissions.

A mapping of MOZART-T1 species to CB6r4 compounds is shown in Table A2 of Appendix A. This mapping was applied in the *firespec* v3.2 that served as the bridge between output from the FINN modeling system and EPS3. FINN's coarse PM, fine PM, organic carbon, elemental carbon, are mapped CF mechanism species. The module also removes fires outside of the CAMx outer domain.

A diurnal profile is applied to the emissions in the *tmprl* module. In their base case, the TCEQ applied a diurnal profile developed by Randerson et al. (2012). In this work, the Randerson profile was retained in the default configuration but a sensitivity study was conducted using a profile developed by the Western Regional Air Partnership Fire Emissions Joint Forum (WRAP-FEJF). A comparison of the temporal profiles is shown in Figure 7.

Fire emissions were allocated vertically for each hour based on the WRAP-FEJF approach (Air Sciences, 2005, Morris et al., 2012; Ramboll, 2016) within the *pstfir* module. The daily area burned for each fire complex is used to classify each fire complex into one of five size bins. The fire size classification determines the fraction of emissions allocated to the CAMx surface layer and to the elevated plume and defines the top and bottom heights of the elevated plume, for each hour of the day (Figure 8). A single point source is used to represent elevated emissions from each member polygon of a fire complex using the new EPS3/CAMx capability to define initial plume depth.

Figure 7. Temporal profiles applied to fire emissions in the EPSv3.22 processing stream based on the approaches of the WRAP-FEJF and Randerson et al. (2012).

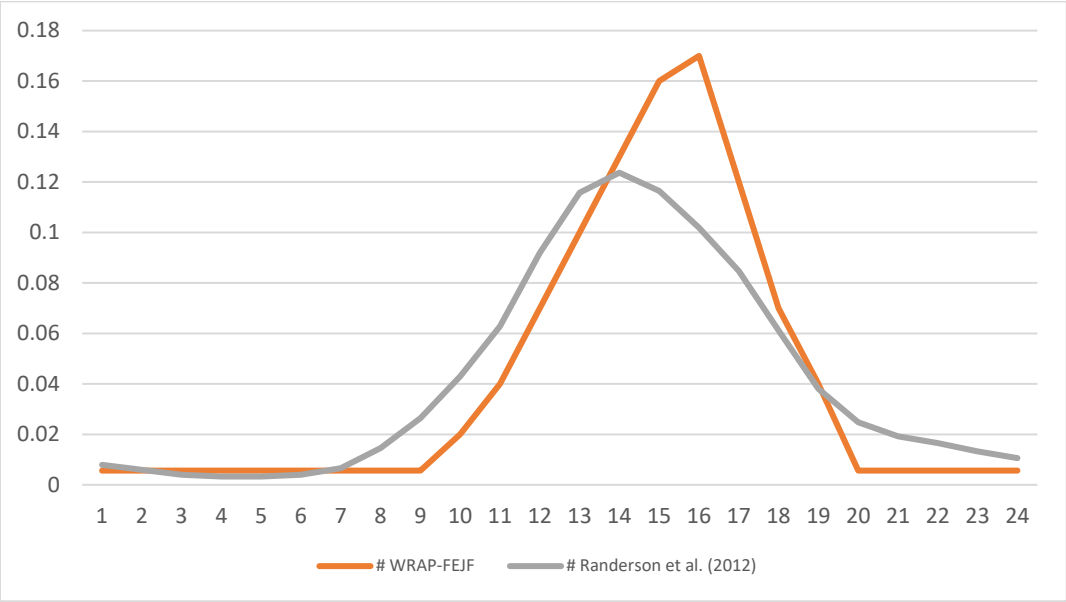

Figure 8. (a) Diurnal profile of the vertical distribution of the fire plumes and (b) the fraction of hourly emissions allocated to CAMx vertical layer 1 in each of the five fire classes defined by daily area burned within each fire complex. Classes are defined by the area burned, less than 10 acres (class 1), 10 to 100 acres (class 2), 100 to 1000 acres (class 3), 1000 to 5000 acres (class 4), greater than 5000 acres (class 5).

(a)

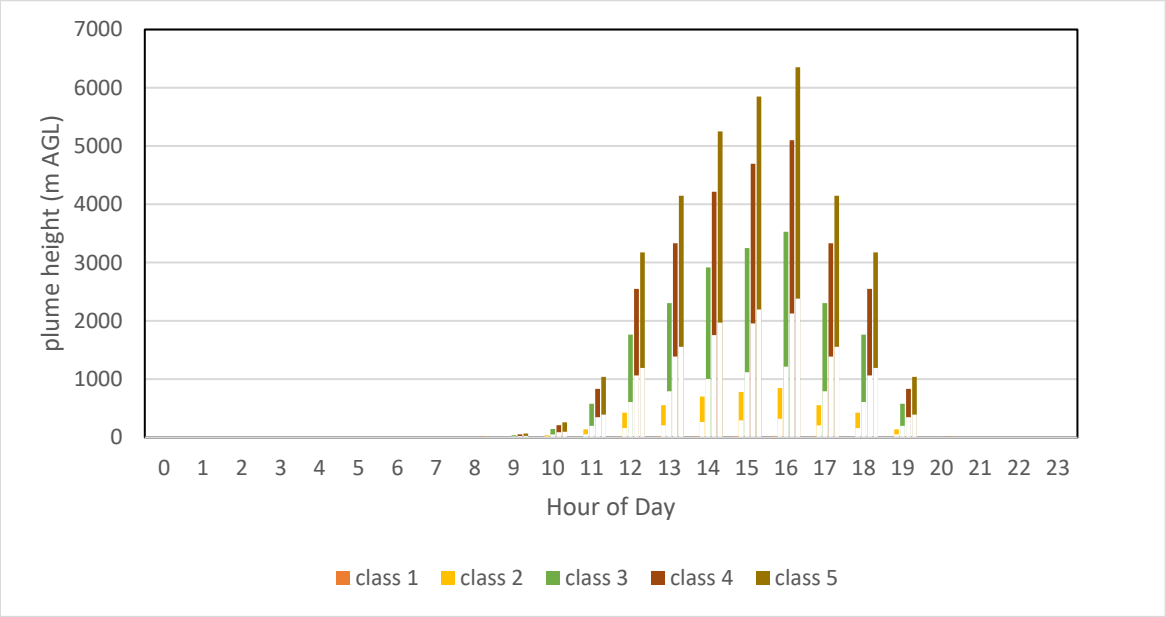

(b)

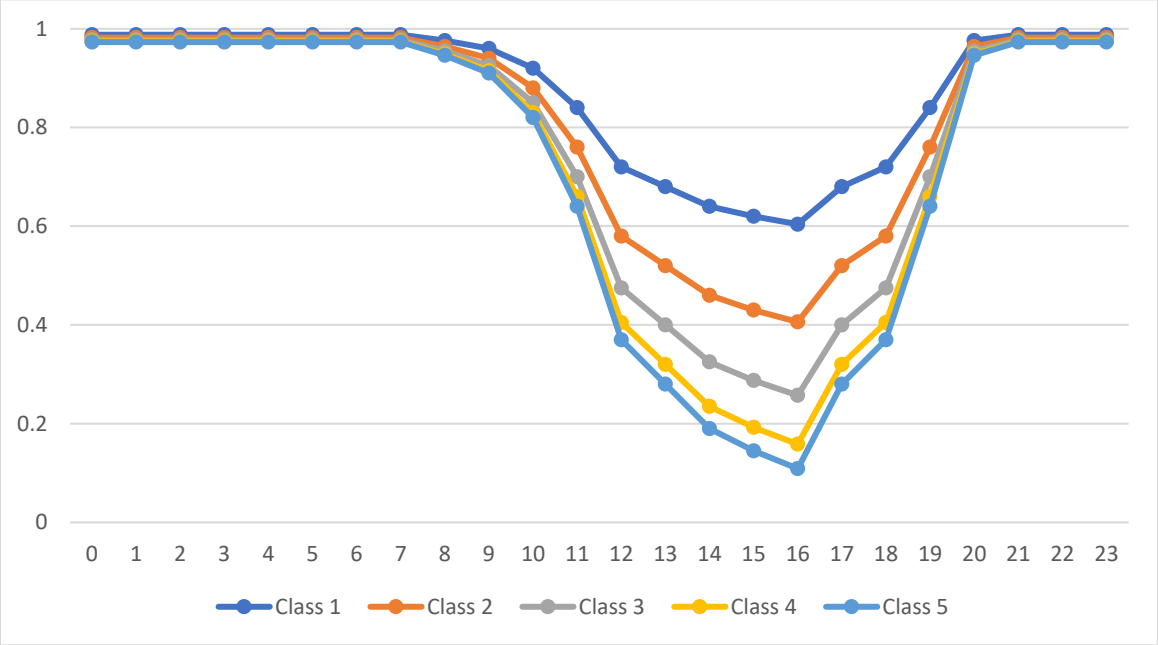

3.3 HYSPLIT Smoke Dispersion Modeling

Smoke dispersion was modeled using HYSPLIT (Stein et al., 2015). The HYSPLIT model uses a hybrid of the Lagrangian and Eulerian approaches and is capable of a range of modeling tasks. Capabilities include modeling of simple air parcel trajectories, transport, dispersion, chemical transformation, and deposition. Dispersion can be modeled using puff or particle mechanisms.

The smoke emissions inventory for 2012 through 2017 from FINN v2.2 was dispersed using HYSPLIT in particle mode using Global Data Assimilation System 0.5 degree (GDAS0P5) meteorological data. Fire emissions from FINN v2.2 were used for the domain covering 6° N to 67° N Latitude, and 51° W to 143° W Longitude. A 50 km resolution receptor grid was used for model output covering the domain shown in Figure 9. The smaller extent of the receptor grid was selected to reduce computational requirements for the dispersion runs, while still reflecting smoke impacts in the domain of interest. The entire year of 2012 was modeled using HYSPLIT, while only the March through September months were modeled for 2013 through 2017 to reflect periods of maximum fire activity.

Several emissions preprocessing steps were taken to facilitate running HYSPLIT across multiple years. Fires were initially clustered by the fire IDs provided by the FINN output. Additional clustering was then performed based on fire density using the DBSCAN method with a search radius of 0.05° (Ester et al., 1996). Finally, smaller fires far from the Texas focus area were screened from the model inputs so as to reduce the total fire number while having a minimal impact on total emissions. Fire screening was performed at varying levels of stringency across the domains shown in Figure 9. Screening applied to each domain is shown in Table 6.

HYSPLIT was run using the BlueSky modeling framework (Larkin et al., 2010), which facilitates smoke emissions modeling and dispersion modeling for fire smoke. The BlueSky Pipeline software used for this modeling was obtained from https://github.com/pnwairfire/bluesky/. The BlueSky Pipeline software has a range of available modules, including fuelbeds, consumption, emissions, localmet, plumerise, timeprofile, dispersion, export, and visualization; for this work, the dispersion, export, and visualization modules were used. Rather than rely on BlueSky pipeline, FINN v2.2 emissions were allocated vertically and temporally using the same profiling approaches described in Section 3.1 for the CAMx model runs to run HYSPLIT and export results

HYSPLIT was configured to run efficiently across the modeling domain using carryover smoke. Key configuration parameters are listed in Table 7. Valid GDAS0P5 meteorological data were not available for March 1 and 10, and August 9, 10, and 12, 2012; August 13, 2013; and March 7, 2014. For these dates, GDAS1 data at 1-degree resolution were used for HYSPLIT dispersion modeling.

Table 6**.** Fire screening domains. Fires smaller than the Fire Site Threshold after clustering were removed from the fire emissions dataset prior to HYSPLIT dispersion modeling.

Domain	Latitude	Longitude	Fire Size Threshold (acres)	Fire Points Removed (%)	Fire Area Removed (%)
Outer Domain	6.0 to 41.0	-57.0 to -124.0	250	75	20
Domain 1	13.0 to 40.0	-64.0 to -120.0	100	51	8
Domain 2	17.0 to 39.0	-75.0 to -118.0	50	35	4
Domain 3	20.0 to 38.0	-82.0 to -116.0	No screening	0	0

Table 7**.** HYSPLIT configuration parameters.

Parameter	Description	Value
KHMAX	Maximum duration (h) for a particle or trajectory	120
NINIT	Particle initialization	1 (=ON)
VERTICAL_EMISLEVELS_REDUCTION_FACTOR	Number of vertical levels	5
TOP_OF_MODEL_DOMAIN	Top of model domain (meters)	10,000
DELT	Minimum integration time step (minutes)	-4.0
NUMPAR	Number of particles released at each emission point per cycle	500
N Levels	Number of levels for HYSPLIT output	3

Figure 9. Receptor domain used for HYSPLIT modeling; the full map area covers 6° N to 41° N Latitude and 57° W to 124° W Longitude. Fire screening was applied in the outer domain, domain 1 (red), and domain 2 (purple). No screening was performed in domain 3 (green).

3.4 Aerosol Optical Depth

The Second IMPROVE equation (Pitchford et al., 2007) was used to calculate model-estimated AOD using output from CAMx and HYSPLIT. The Second IMPROVE equation calculates light extinction (*b*ext) based on relative humidity-adjusted aerosol concentrations and Rayleigh scattering:

$$\begin{aligned} b\text{ext} \approx\ & 2.2 \times f_S(\text{RH}) \times [\text{Small Ammonium Sulfate}] + 4.8 \times f_L(\text{RH}) \times \\ & [\text{Large Ammonium Sulfate}] + 2.4 \times f_S(\text{RH}) \times [\text{Small Ammonium Nitrate}] + \\ & 5.1 \times f_L(\text{RH}) \times [\text{Large Ammonium Nitrate}] + 2.8 \times [\text{Small Organic Mass}] + \\ & 6.1 \times [\text{Large Organic Mass}] + 10 \times [\text{Elemental Carbon}] + 1 \times [\text{Fine Soil}] + \\ & 1.7 \times f_{SS}(\text{RH}) \times [\text{Sea Salt}] + 0.6 \times [\text{Coarse Mass}] + \text{Rayleigh Scattering} + \\ & 0.33 \times [\text{NO2 (ppb)}] \end{aligned} \quad (4)$$

Where extinction and scattering are given in inverse megameters, concentrations are given in micrograms per cubic meter, extinction efficiency is in square meters per gram, and water growth terms (e.g., f(RH)) has no units. Sea salt, small modes of sulfate and nitrate, and large modes of sulfate and nitrate have specific water growth terms (f_{ss}(RH), f_s(RH), and f_l(RH), respectively).

For CAMx, the *b*ext was calculated at each vertical level of the model output using the second IMPROVE equation and meteorological data from the 2012 photochemical modeling episode described above. AOD was calculated by summing the extinction calculated for each layer, scaled by the thickness of the layer.

HYSPLIT dispersion modeling resulted in total $PM_{2.5}$, and fractions of $PM_{2.5}$ specified in Table 8 were applied to total $PM_{2.5}$ (values derived from Akagi et al., 2011 and U.S. Environmental Protection Agency, 2018). Using the speciated $PM_{2.5}$, AOD was calculated using Equation 4. NASA Modern-Era Retrospective analysis for Research and Applications, version 2 (MERRA-2) provides three-hour averaged relative humidity, which has been used to calculate AOD in other contexts, including the MERRA-2 system (Randles et al., 2017). The relative humidity data (tavg3_3d_asm_Nv) was used to estimate RH at each level of HYSPLIT output for use in the second IMPROVE equation. Rayleigh scattering and NO_2 values were not used in the calculation of HYSPLIT AOD because gridded data were not readily available across the study domain. Coarse mass was also not used in the calculation because only $PM_{2.5}$ emissions were used in the HYSPLIT dispersion runs.

The resulting AOD calculated is considered the total column AOD contribution from wildfires. This result can be used to represent total column AOD because smoke is unlikely to be transported above the 10km top of model domain used in the HYSPLIT dispersion model. Typical wildfire smoke plume injection heights rarely exceed 2 km and are not observed above 6 km (Val Martin et al., 2018). While transport may carry smoke above the HYSPLIT domain in rare cases, this is unlikely to substantially impact modeled AOD.

Table 8**.** Fractionated $PM_{2.5}$ assumed for HYSPLIT AOD calculations.

Component	Fraction of PM2.5
Elemental Carbon (EC)	0.0949
Organic Carbon (OC)	0.4618
SO4	0.2857
NO3	0.0286
Sea Salt	0.0645
Fine Soil	0.0645

4. Fire Emissions Estimates

Global-scale simulations for 2016 and 2018 using FINNv2.2 with MODIS and VIIRS fire detections were conducted to assess the effects of fire activity on emissions estimates for different regions of the world. Emissions estimates for North America using FINNv2.2 with MODIS and VIIRS fire detections were developed for 2012 through 2018 to support comparisons with the MAIAC AOD product. In addition, sensitivity studies were conducted to examine the effects of including VIIRS versus using only MODIS fire detections and differences between FINNv1.5 and FINNv2.2. The results of these simulations are described in this section.

4.1 FINN v2.2 Emissions Estimates with MODIS and VIIRS Fire Detections

4.1.1 Global Regions

Fire emissions estimates during 2016 and 2018 were developed for 12 global regions (Antarctica was not included) shown in Figure 10 using FINNv2.2 with MODIS in combination with VIIRS fire detections. Figure 11 shows monthly total CO emissions estimates by global region. It illustrates distinctive temporal patterns in fire activity between global regions, for example agricultural fire activity in Central America and Southern Asia in the spring, and Southern Africa in the late spring through fall, as well as interannual variability of emissions between the 2016 and 2018 fire seasons. The 2018 wildfire season in the U.S. and Canada was particularly pronounced relative to the 2016 season. Figure 12 shows annual total global $PM_{2.5}$ emissions in 2016 and 2018.

Figure 10. FINNv2.2 global regions.

Figure 11. Monthly total CO emissions (Tg/month) during 2016 (solid) and 2018 (dashed) from FINNv2.2 with MODIS and VIIRS active fire detections: (a) North America, (b) Central America, (c) South America, (d) Oceania, (e) Northern Africa, (f) Southern Africa, (g) Western Europe, (h) Eastern Europe, (i) Near East, (j) North Central Asia, (k) East Asia, and (l) Southern Asia. Note differences in scales between plots.

(a)

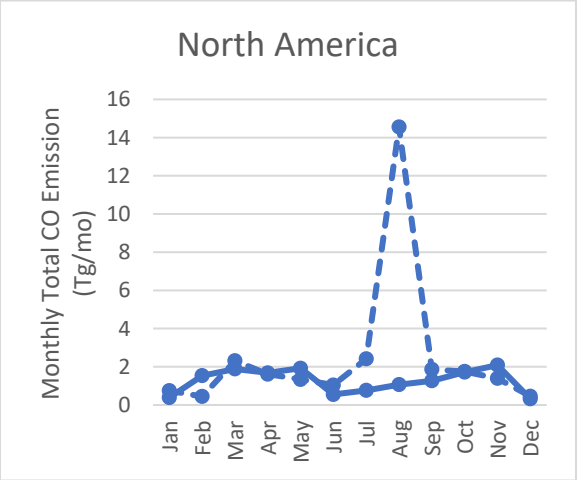

(b)

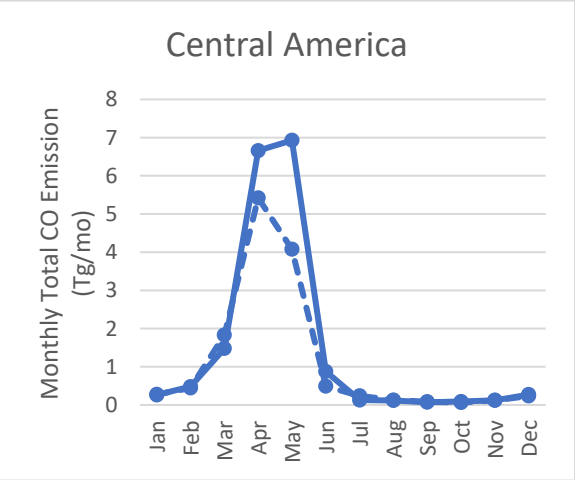

(c)

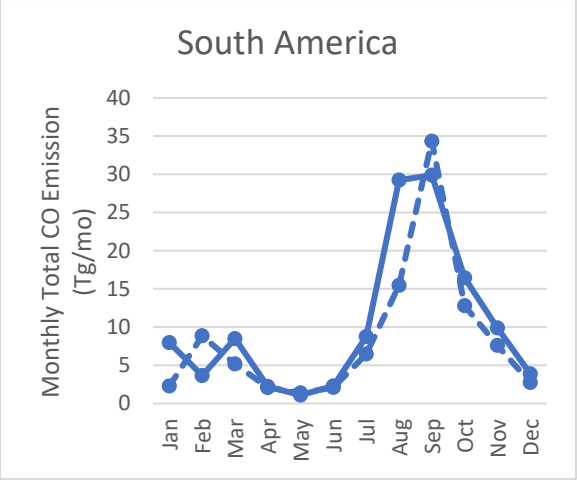

(d)

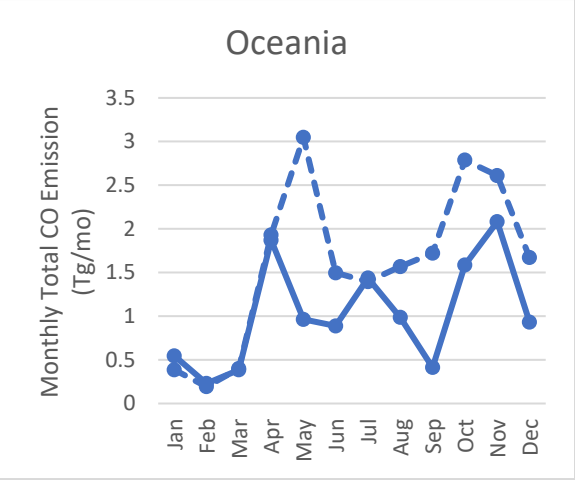

(e)

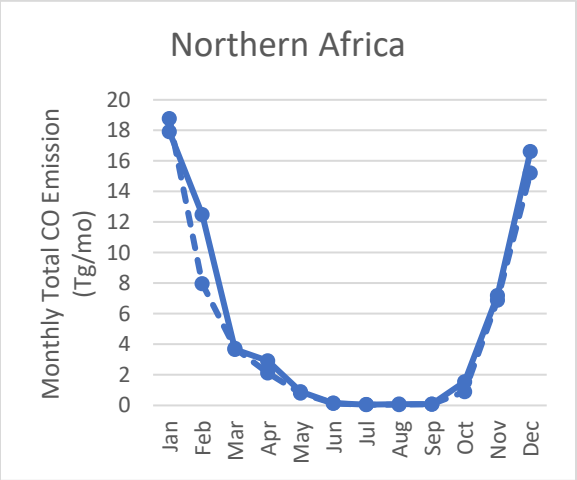
Northern Africa
Monthly Total CO Emission (Tg/mo)
0
2
4
6
8
10
12
14
16
18
20
Jan
Feb
Mar
Apr
May
Jun
Jul
Aug
Sep
Oct
Nov
Dec

(f)

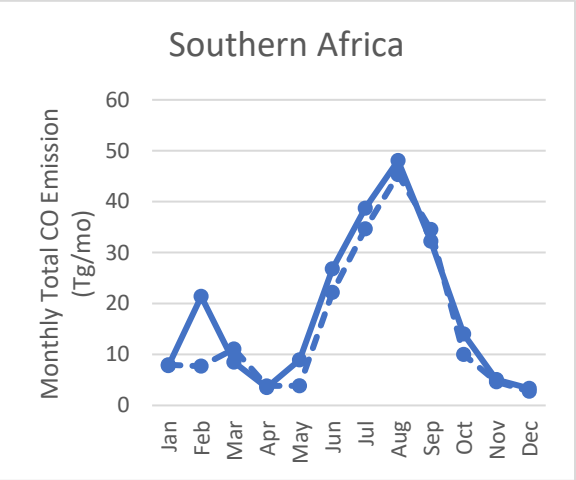
Southern Africa
Monthly Total CO Emission (Tg/mo)
0
10
20
30
40
50
60
Jan
Feb
Mar
Apr
May
Jun
Jul
Aug
Sep
Oct
Nov
Dec

(g)

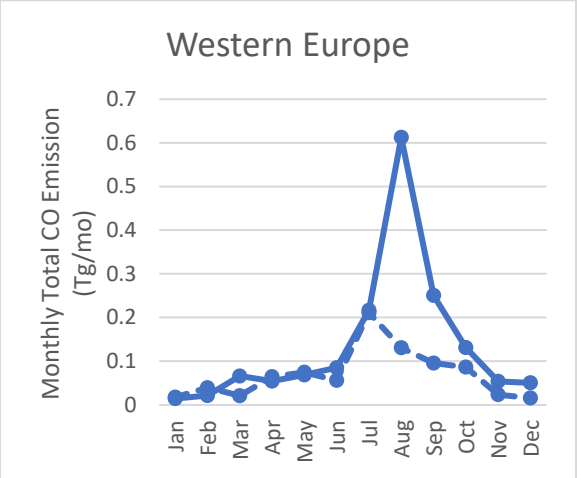
Western Europe
Monthly Total CO Emission (Tg/mo)
0
0.1
0.2
0.3
0.4
0.5
0.6
0.7
Jan
Feb
Mar
Apr
May
Jun
Jul
Aug
Sep
Oct
Nov
Dec

(h)

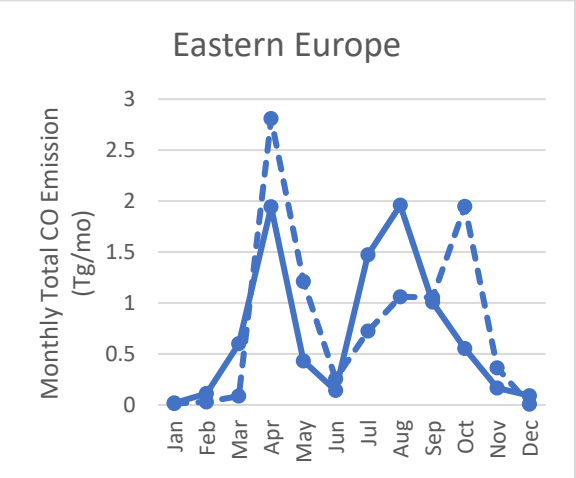
Eastern Europe
Monthly Total CO Emission (Tg/mo)
0
0.5
1
1.5
2
2.5
3
Jan
Feb
Mar
Apr
May
Jun
Jul
Aug
Sep
Oct
Nov
Dec

(i)

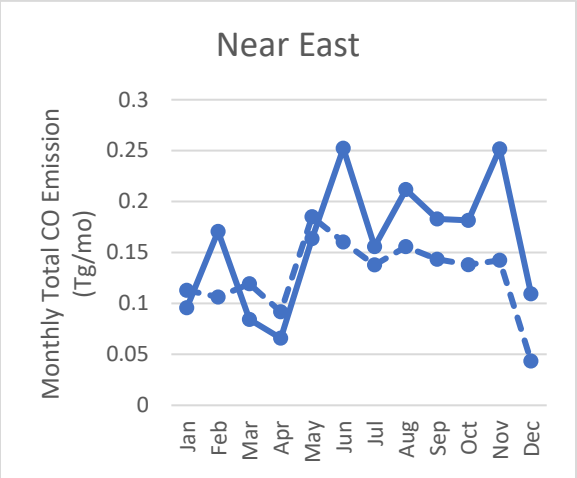
Near East
Monthly Total CO Emission (Tg/mo)
0
0.05
0.1
0.15
0.2
0.25
0.3
Jan
Feb
Mar
Apr
May
Jun
Jul
Aug
Sep
Oct
Nov
Dec

(j)

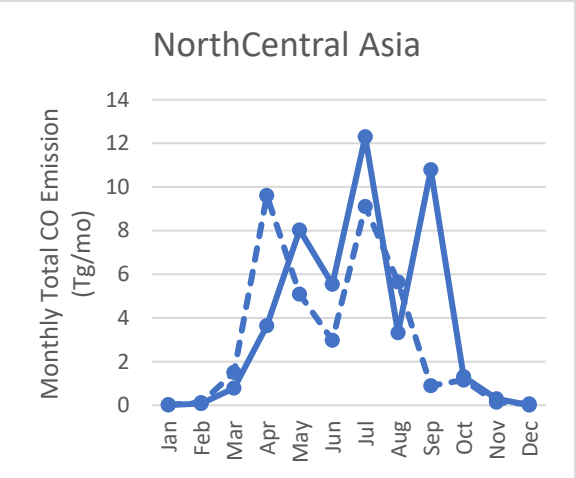
NorthCentral Asia
Monthly Total CO Emission (Tg/mo)
0
2
4
6
8
10
12
14
Jan
Feb
Mar
Apr
May
Jun
Jul
Aug
Sep
Oct
Nov
Dec

(k)

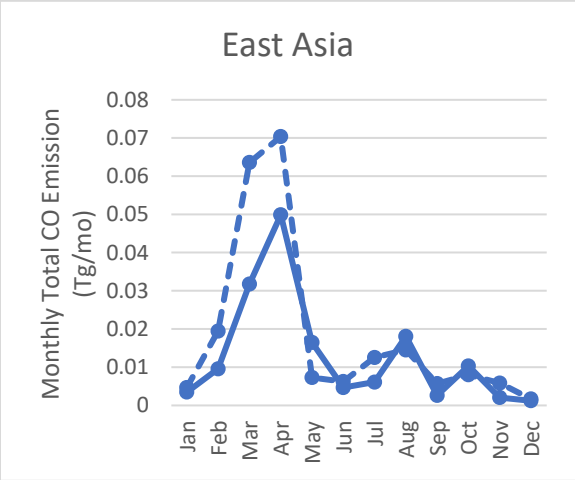
East Asia
Monthly Total CO Emission (Tg/mo)
0.08
0.07
0.06
0.05
0.04
0.03
0.02
0.01
0
Jan
Feb
Mar
Apr
May
Jun
Jul
Aug
Sep
Oct
Nov
Dec

(l)

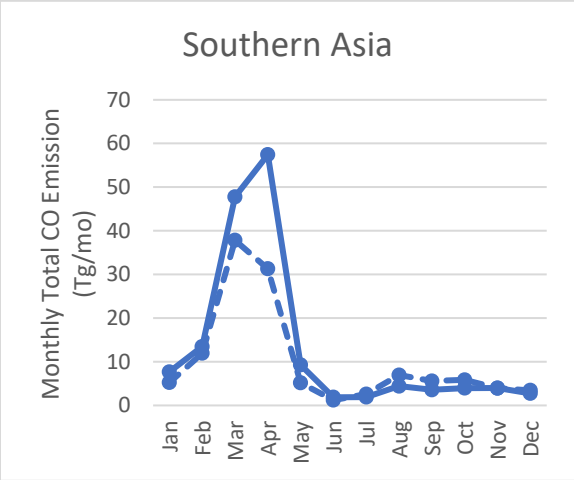
Southern Asia
Monthly Total CO Emission (Tg/mo)
70
60
50
40
30
20
10
0
Jan
Feb
Mar
Apr
May
Jun
Jul
Aug
Sep
Oct
Nov
Dec

Figure 12. Annual total $PM_{2.5}$ emissions (kg/km^2) in (a) 2016 and (b) 2018.

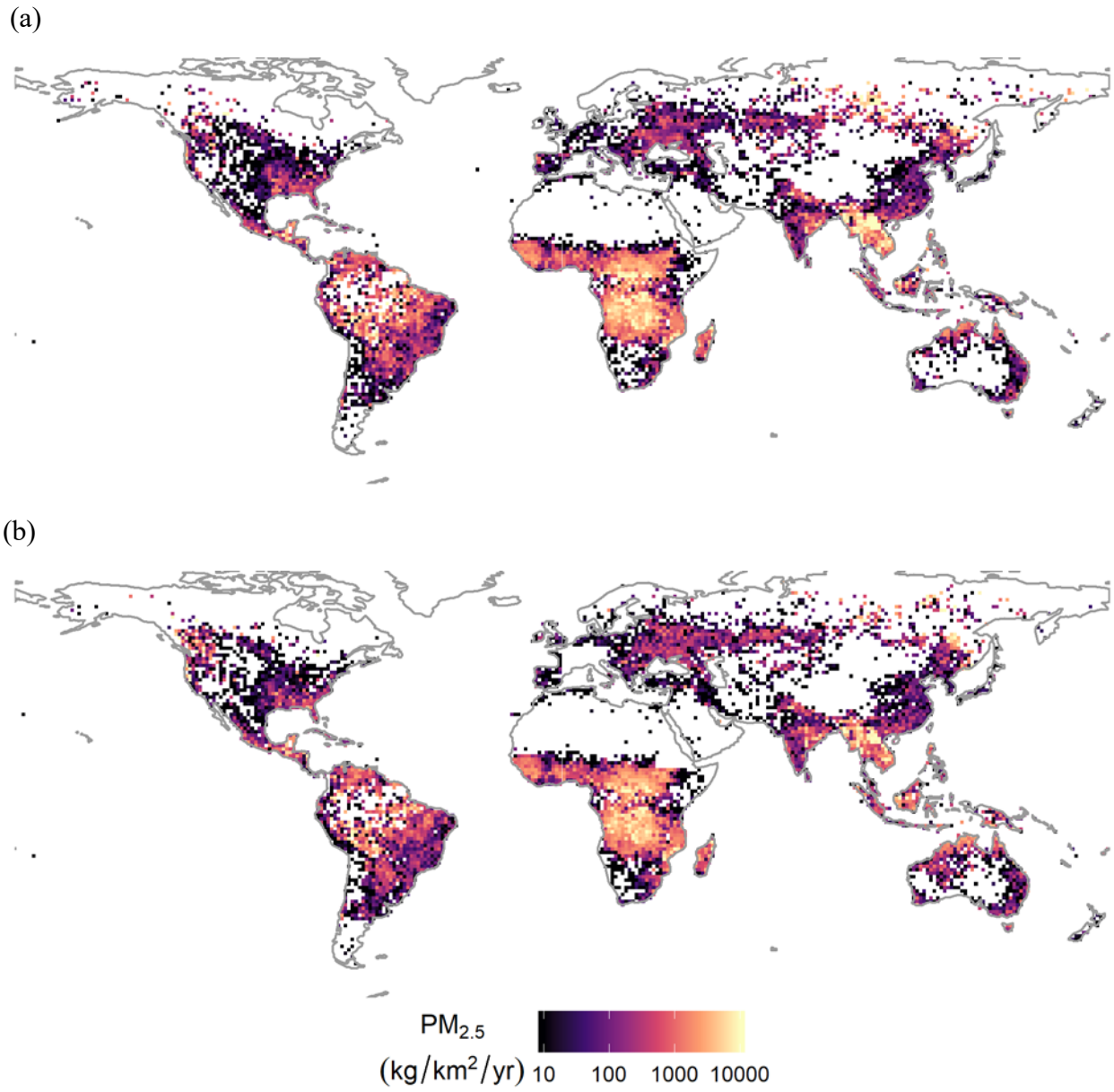

4.1.2 Interannual Trends in U.S. Subregions and Mexico

Monthly total emissions of $PM_{2.5}$ and NO_x during 2012 through 2018 from FINN v2.2 with MODIS and VIIRS active fire detections in Mexico, Texas, the Western US, the Lower Mississippi Valley, and Southeastern US (Figure 13) are shown in Figures 14 and 15, respectively. These regions of the United States typically exhibit high fire activity.

Texas usually experiences two wildfire seasons, winter/spring associated with dry fuels, winds and warming temperatures and late summer/early fall with hot, dry weather conditions. Years with notable peaks include 2013 and 2016, 2017, and in particular 2018, during which the timing

of the fire season began early in the state with high fuel availability, drought and other conducive environmental conditions (Russell, 2018). Mexico exhibits strong spring peaks in emissions that coincide with agricultural fire activity and can affect air quality in Texas. Seasonal and interannual patterns in NO_x and $PM_{2.5}$ emissions are similar within the regions shown.

Figure 13. Mexico and U.S. states grouped by subregion.

Figure 14. Annual trends in monthly total $PM_{2.5}$ emissions (Gg/mo) during 2012 through 2018 for (a) Texas, (b) Mexico, and (c) Western U.S., (d) Lower Mississippi Valley and (e) southeastern U.S. Note differences in scales between plots.

(a)

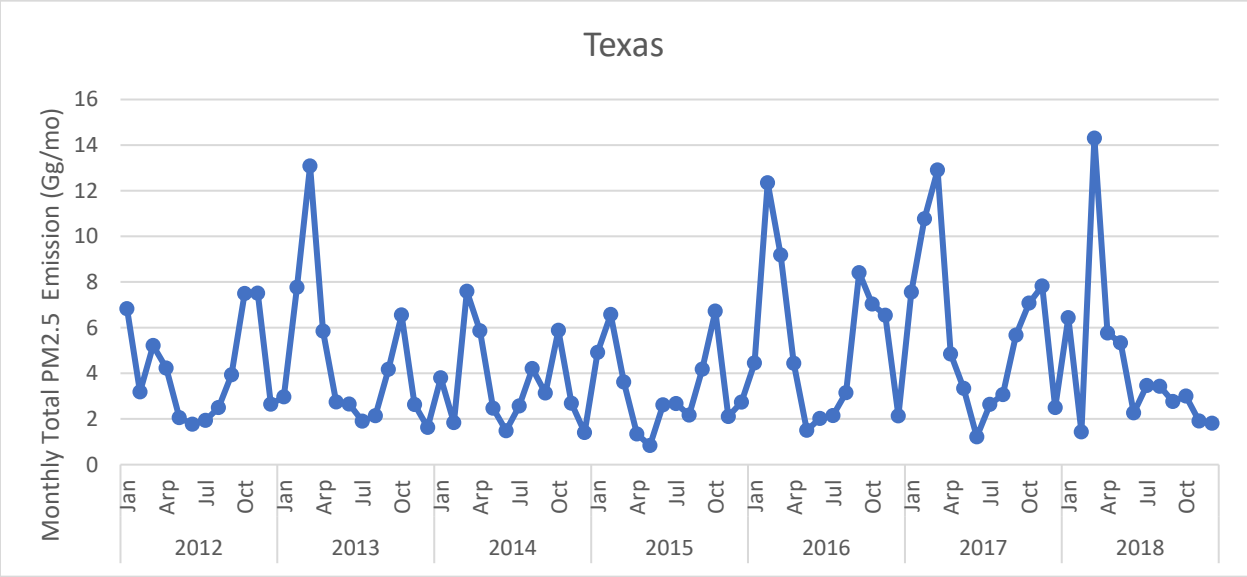

(b)

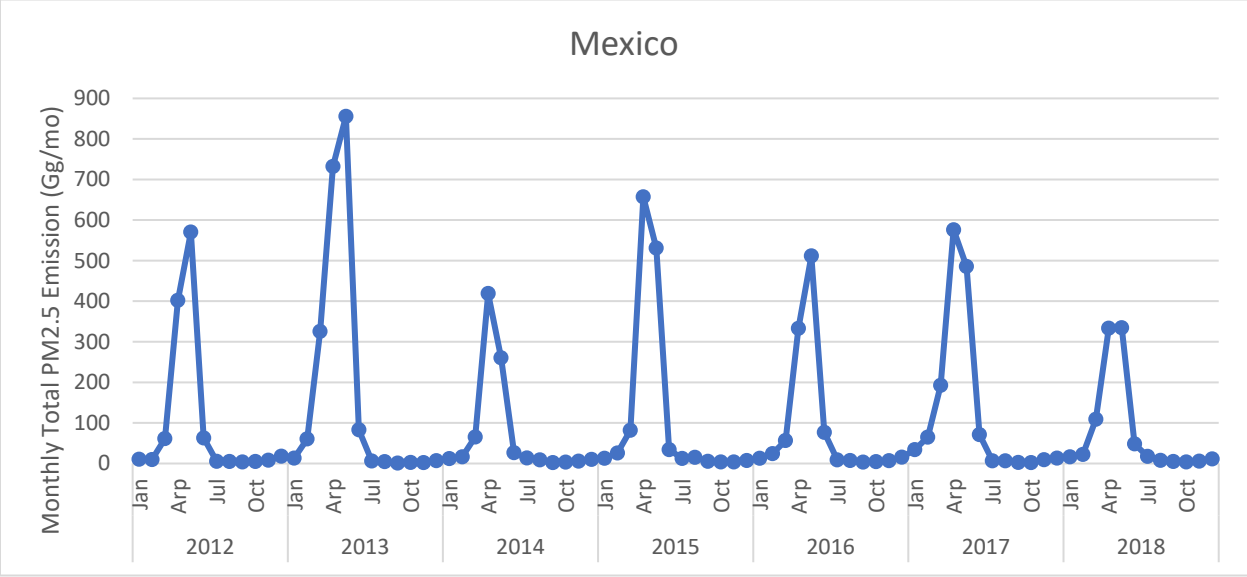

(c)

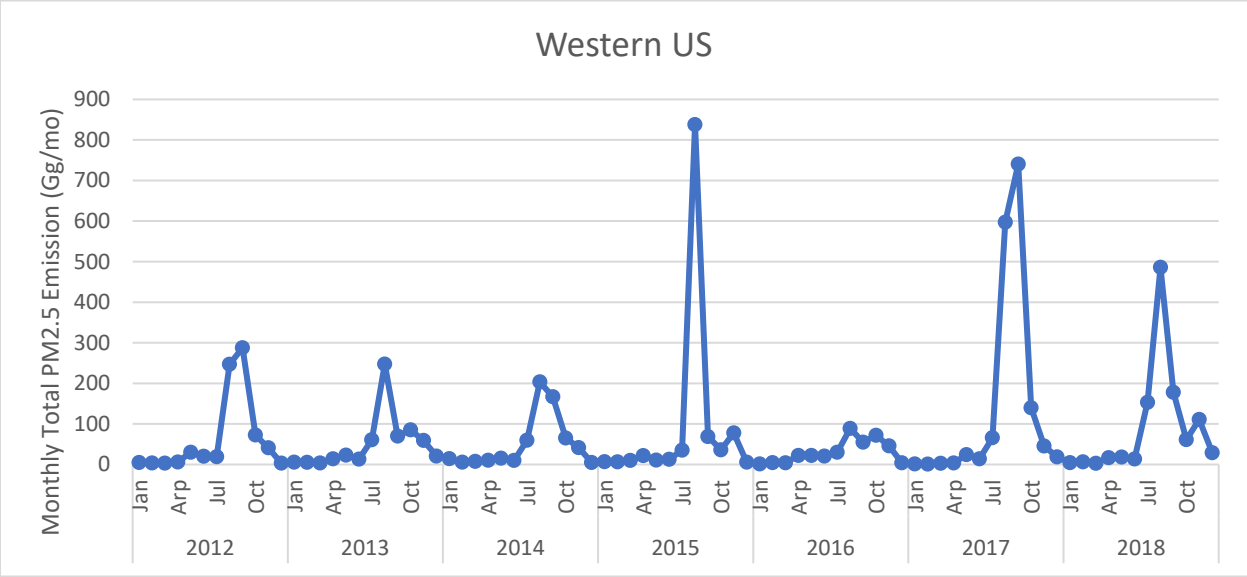
Western US
Monthly Total PM2.5 Emission (Gg/mo)
900
800
700
600
500
400
300
200
100
0
Jan
Arp
Jul
Oct
2012
2013
2014
2015
2016
2017
2018

(d)

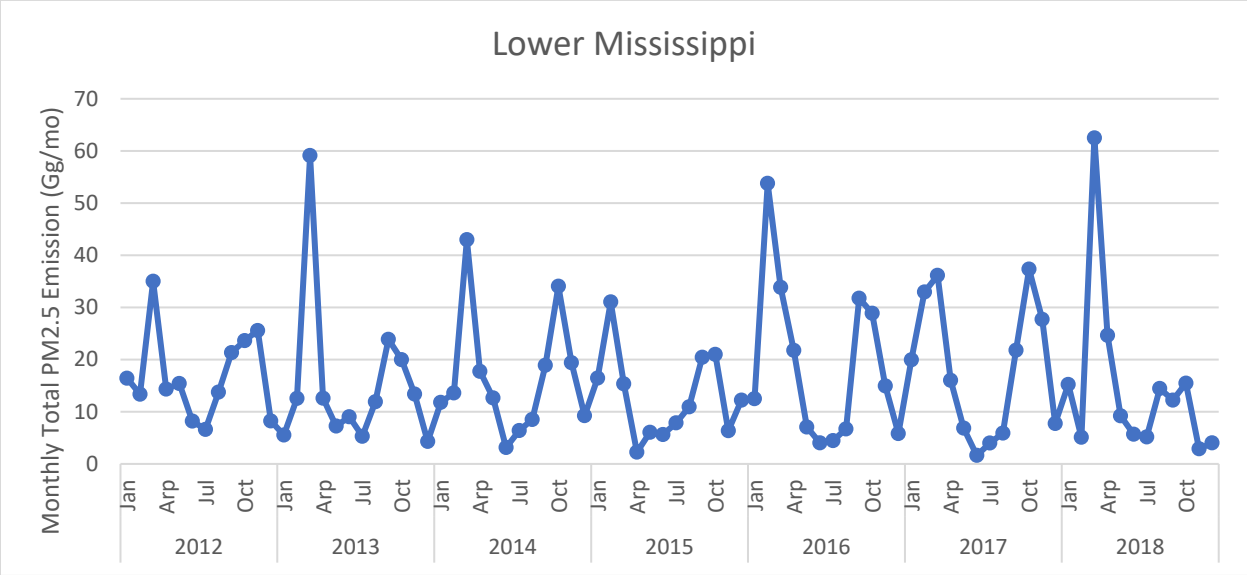
Lower Mississippi
Monthly Total PM2.5 Emission (Gg/mo)
70
60
50
40
30
20
10
0
Jan
Arp
Jul
Oct
2012
2013
2014
2015
2016
2017
2018

(e)

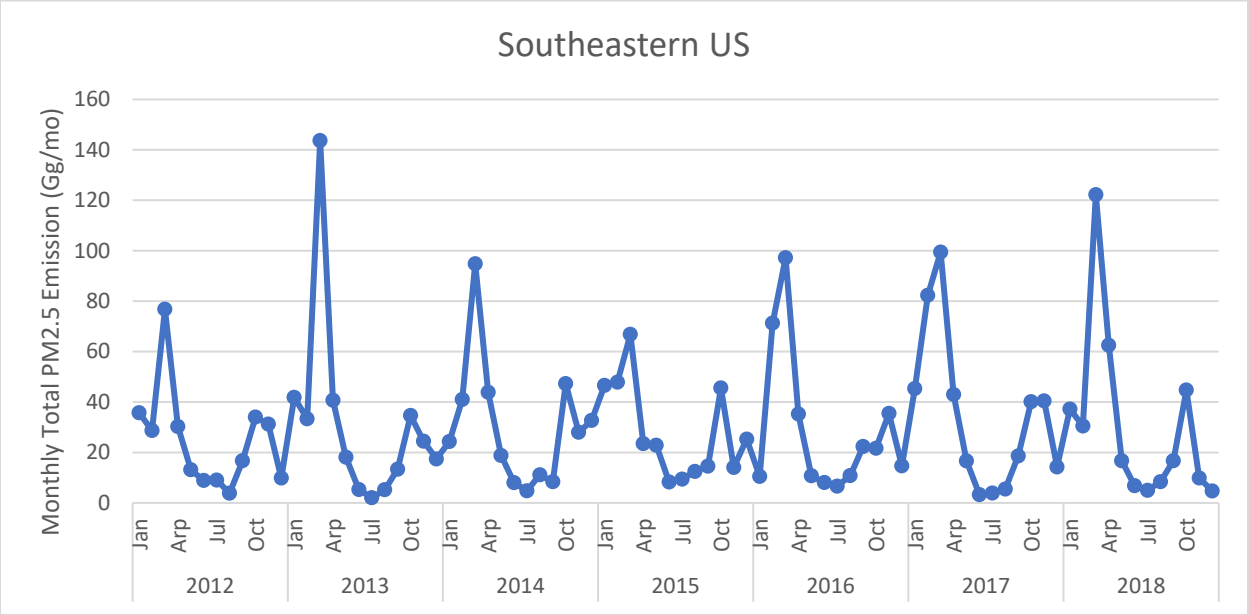
Southeastern US
Monthly Total PM2.5 Emission (Gg/mo)
160
140
120
100
80
60
40
20
0
Jan
Arp
Jul
Oct
2012
2013
2014
2015
2016
2017
2018

Figure 15. Annual trends in monthly total NO_x emissions (Gg/month) during 2012 through 2018 for (a) Texas, (b) Mexico, and (c) Western U.S., (d) Lower Mississippi Valley and (e) southeastern U.S. Note differences in scales between plots.

(a)

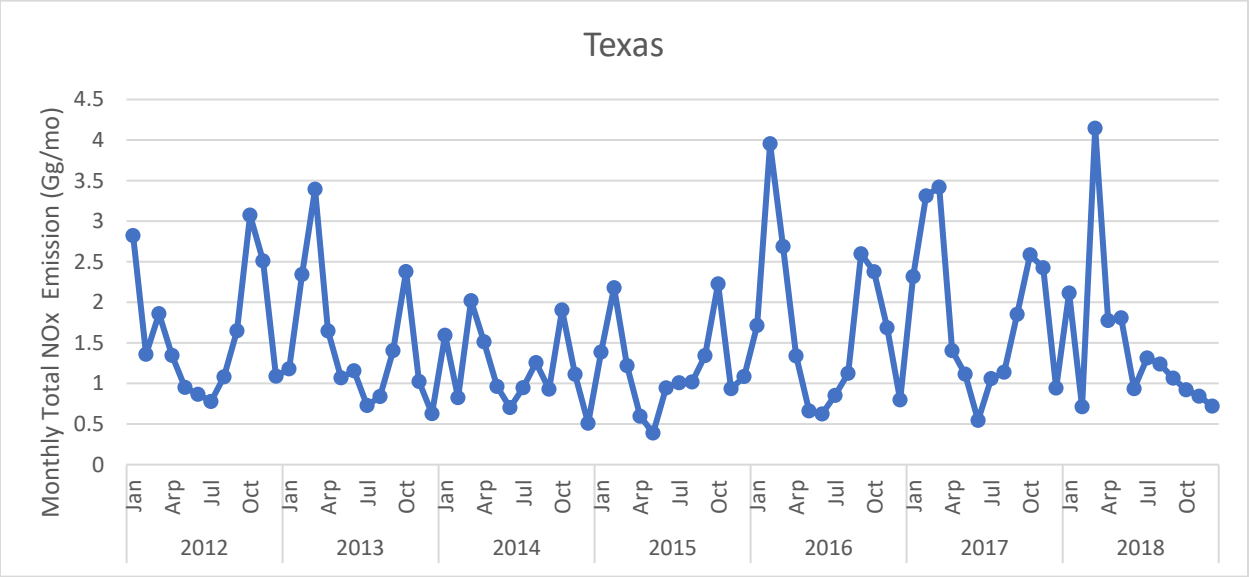

(b)

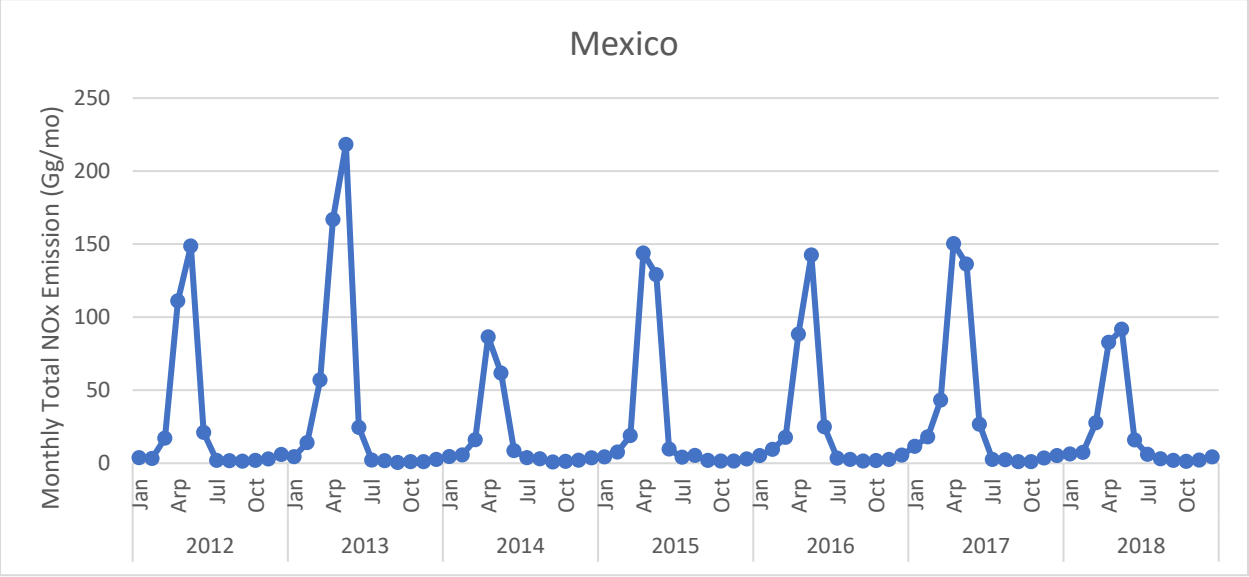

(c)

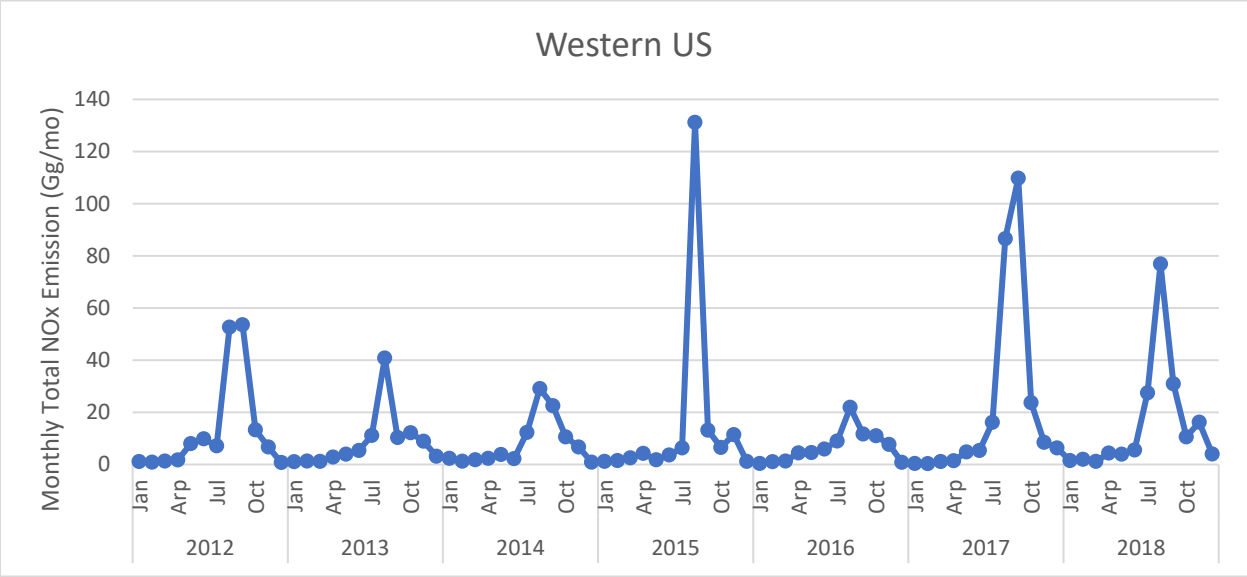
Western US
Monthly Total NOx Emission (Gg/mo)
140
120
100
80
60
40
20
0
Jan
Arp
Jul
Oct
2012
2013
2014
2015
2016
2017
2018

(d)

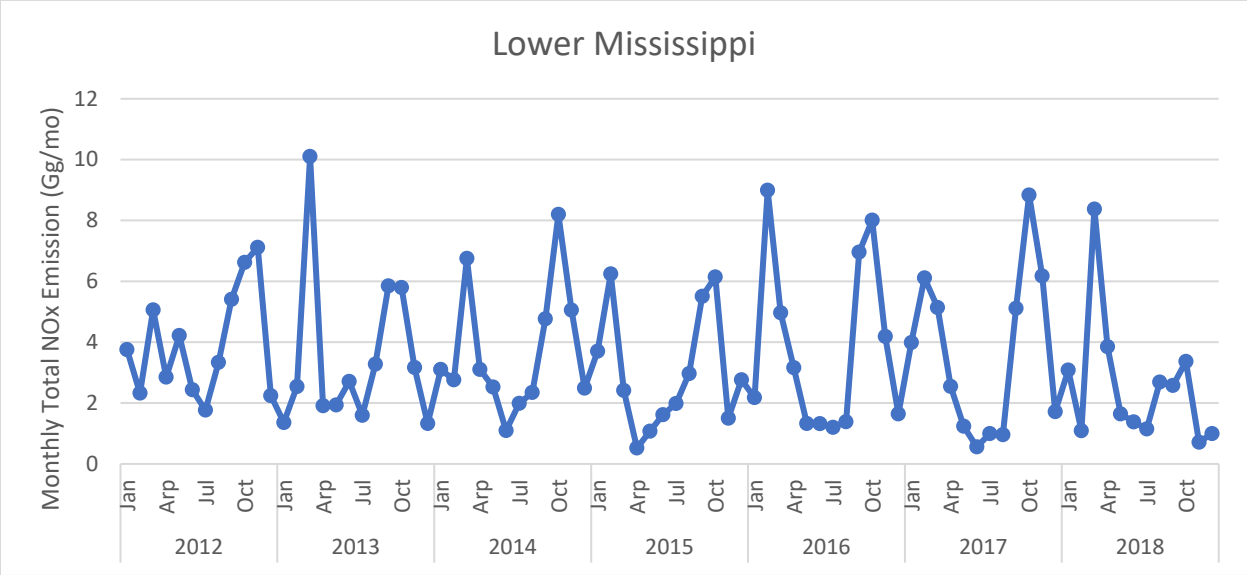
Lower Mississippi
Monthly Total NOx Emission (Gg/mo)
12
10
8
6
4
2
0
Jan
Arp
Jul
Oct
2012
2013
2014
2015
2016
2017
2018

(e)

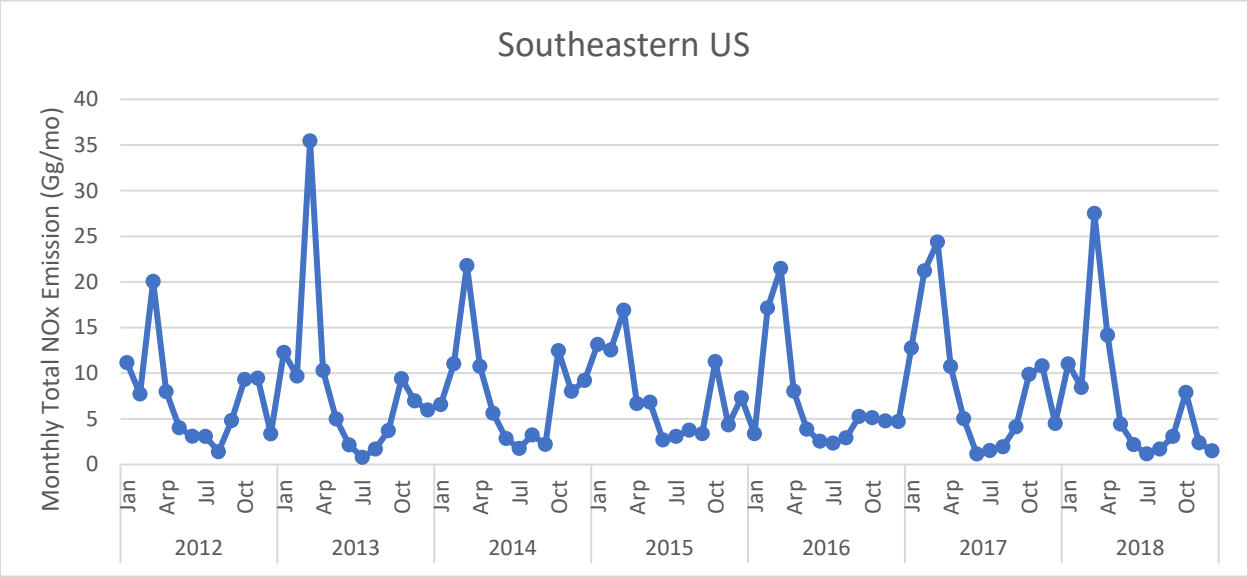

4.2 Sensitivity of Emissions Estimates to VIIRS Active Fire Detections and FINN Version

Simulations were conducted to examine the effects of including VIIRS versus using only MODIS fire detections in FINN v2.2 and differences between FINNv1.5 and FINNv2.2 for the 2016 base year. Results are shown for Texas, the Southeastern U.S. and Lower Mississippi Valley states, and Mexico, and described in detail for Texas.

Figure 16 shows monthly total $PM_{2.5}$, NO_x and NMOC emissions estimates during 2016 in Texas for FINNv.1.5, FINNv2.2 with only MODIS or with MODIS and VIIRS fire detections. Figure 17 illustrates the spatial patterns in total $PM_{2.5}$ emissions for the different model configurations during February 2016, which had the highest monthly emissions of the year. As described in Section 2, several significant changes occurred between FINNv1.5 and v2.2. Overall the changes lead to increases in emissions of $PM_{2.5}$, NO_x and NMOC with v2.2 in Texas. It is difficult to capture the full complexity of the interactions between model parameters that contribute to variations emissions estimates for any given fire event or between different fire events. However, Figure 18 provides a perspective of the contribution of land cover types as well as the differences in parameters that contribute to differences in emissions estimates between model versions.

Area burned increases markedly between FINNv1.5 and FINN v2.2 with MODIS detections only and more substantially when combined with detection from VIIRS. Although this is a consequence of the new algorithm implemented in FINNv2.2 as well as the improved spatial resolution of the VIIRS product when it is used, a transition from the use of MODIS Collections 5 and 6 products for fire detection in FINNv1.5 to the use of MODIS Collection 6 (MCD12Q1) with FINNv2.2 could also contribute to differences in burned area. FINN v2.2 also includes more recent year-specific MODIS land cover type and VCF products than v1.5. Biomass loadings from the FCCS in FINN v.2.2 now supersede North American regional default values, unless the user specifies otherwise.

Emission factors are similar between the model versions with the notable exception of NMOC. All measured NMOC is included in the applied emission factor for FINN v2.2 rather than only the identified NMOC fraction. This change dominates the contribution to differences in these emissions estimates between the model versions.

Figure 18 indicates that grasses, shrublands, and forests are most associated with fire activity and emissions in Texas. Grasslands have a relatively greater contribution to fires in February than in September 2016. Forests provide smaller contributions to total area burned than grasses or shrublands. They provide more substantial contributions to emissions of CO, $PM_{2.5}$, and especially NMOC, but smaller contributions to NO_x emissions in Texas.

Figures 19 shows monthly total $PM_{2.5}$, NO_x and NMOC emissions estimates in 2016 in the Southeastern U.S. and Lower Mississippi Valley for the different model configurations. Figure 20 illustrates the spatial patterns in total $PM_{2.5}$ emissions during March 2016. Figure 21 shows the contribution of land cover types as well as the differences in parameters that contribute to differences in emissions estimates between model versions for these regions. Similar information is provided for Mexico in Figures 22, 23, and 24.

Figure 16. Monthly total (a) $PM_{2.5}$, (b) NO_x and (c) NMOC emissions estimates during 2016 in Texas by FINNv.1.5, FINNv2.2 with MODIS only fire detections, and FINNv2.2 with MODIS and VIIRS fire detections. Note differences in scales between plots.

(a)

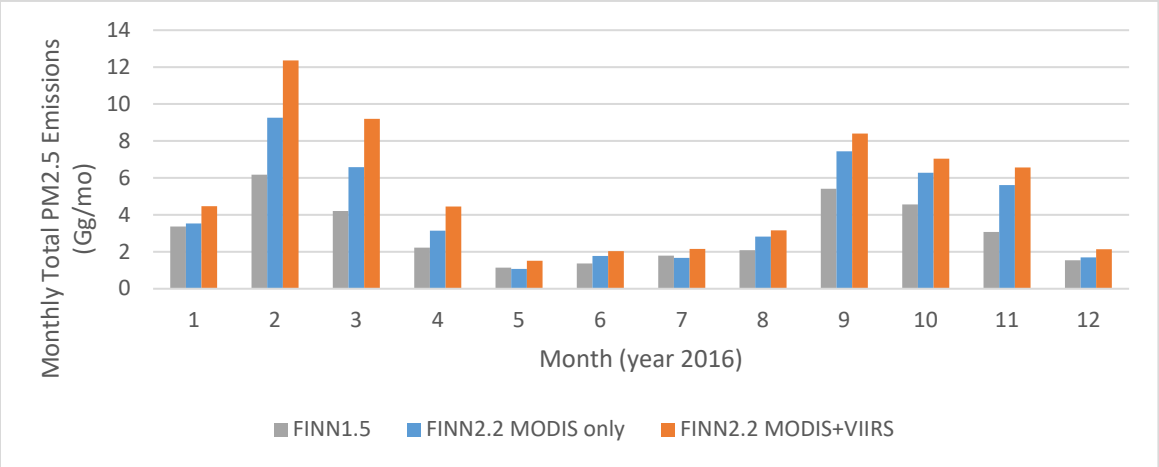

(b)

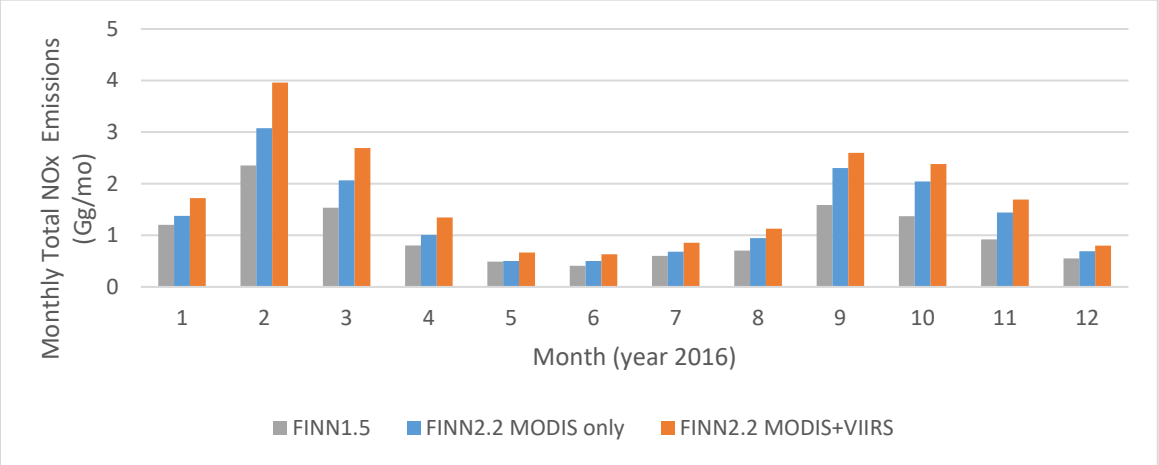

(c)

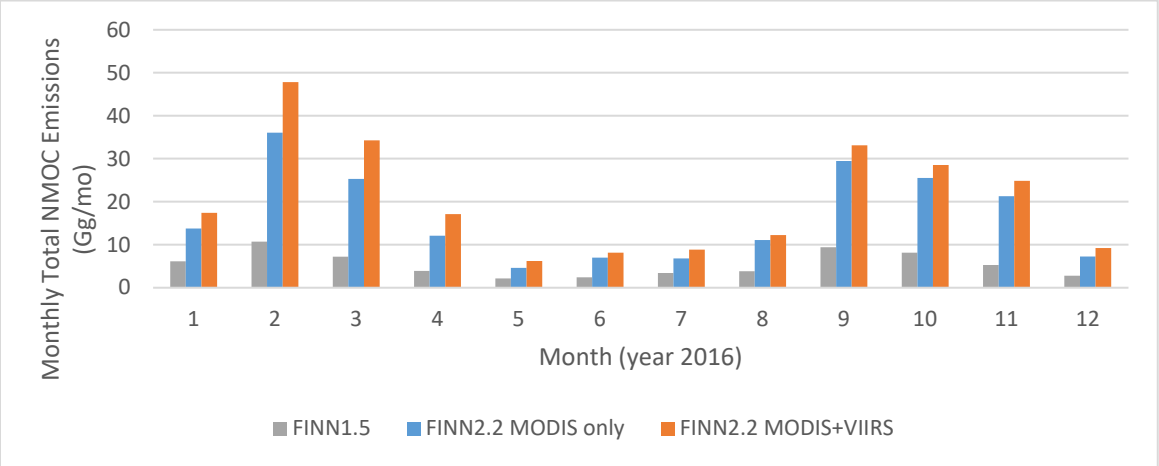

Figure 17. Total $PM_{2.5}$ emissions ($Mg/km^2/mo$) in February 2016 from FINNv.1.5, FINNv2.2 with MODIS only fire detections, and FINNv2.2 with MODIS and VIIRS fire detections.

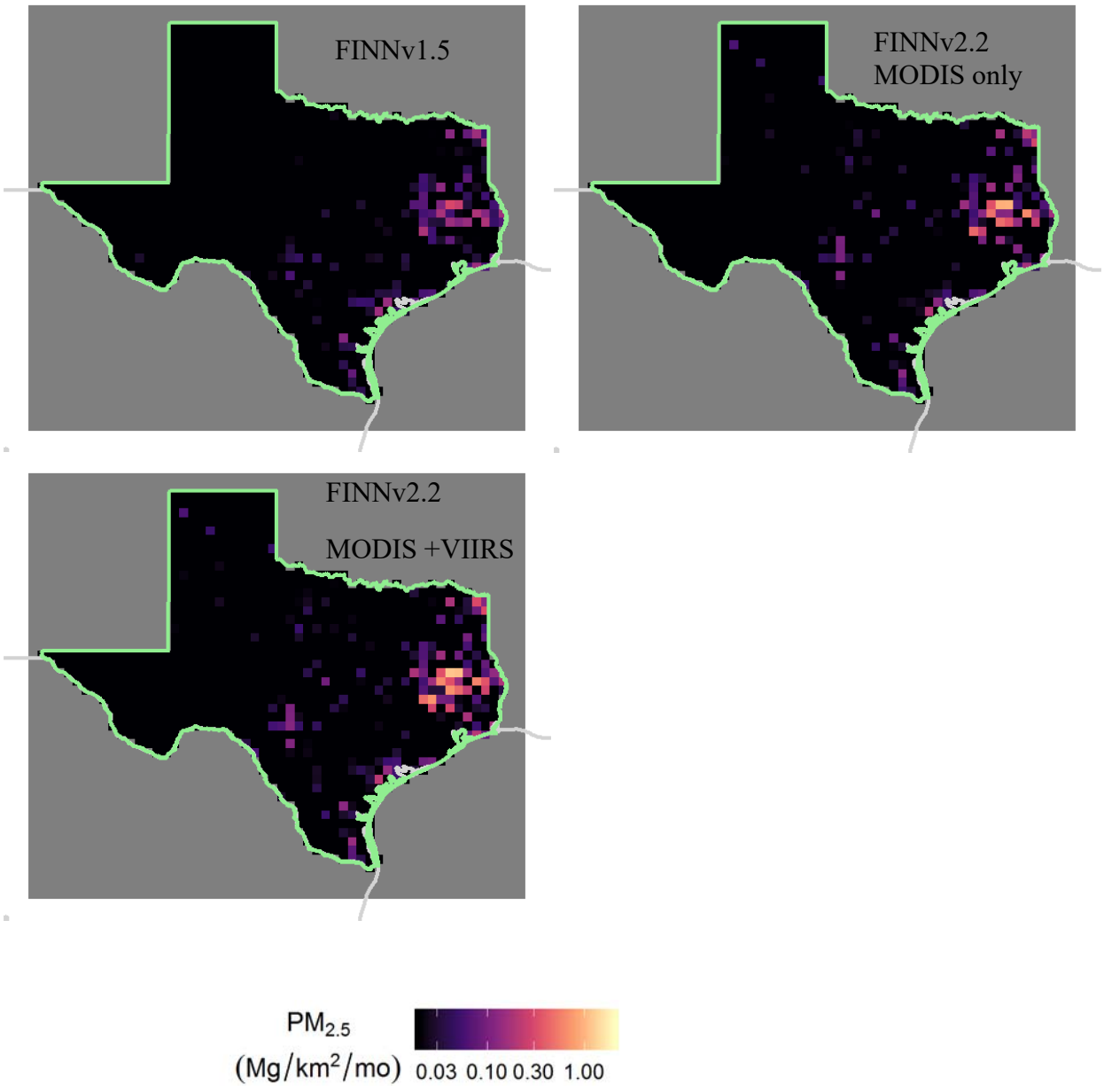

Figure 18. Contribution of land cover type to area burned, biomass loading, and total monthly CO, NMOC, NO_x, and $PM_{2.5}$ emissions in Texas from FINN v2.2 with MODIS only or in combination with VIIRS fire detections during (a) February and (b) September 2016. Contributions are normalized by the values for FINNv1.5. Land cover types shown for Texas include tropical forest, temperate forest, evergreen forest, shrublands, grasses, and croplands. Note differences in scales between plots.

(a)

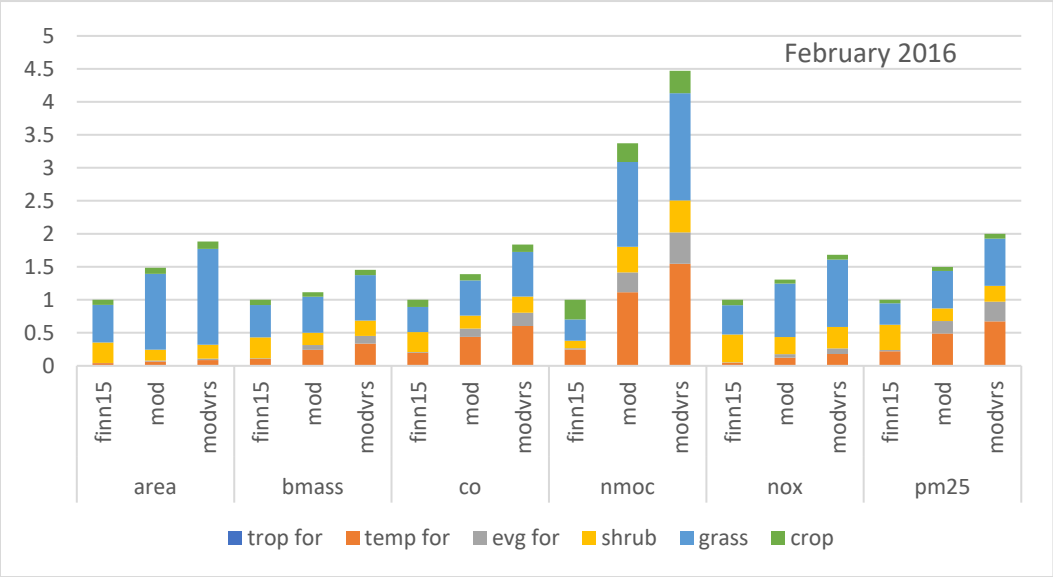

(b)

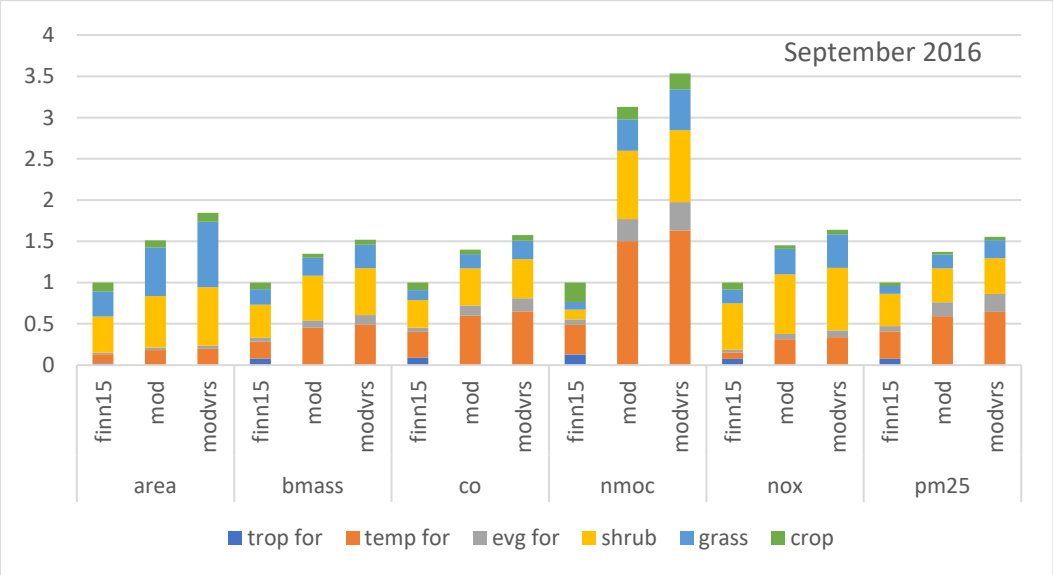

Figure 19. Monthly total (a) $PM_{2.5}$, (b) NO_x and (c) NMOC emissions estimates during 2016 in the Southeastern U.S. and Lower Mississippi Valley by FINNv.1.5, FINNv2.2 with MODIS only fire detections, and FINNv2.2 with MODIS and VIIRS fire detections. Note differences in scales between plots.

(a)

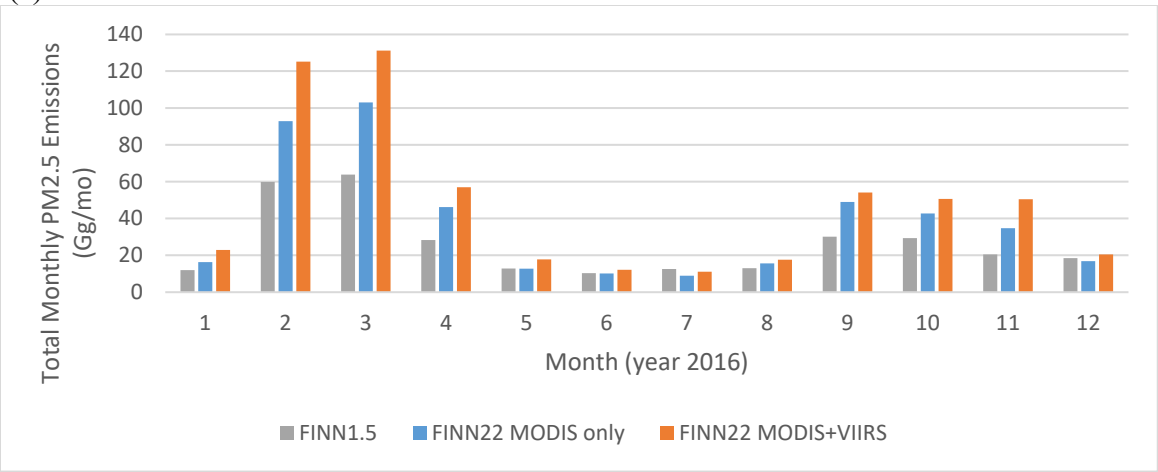

(b)

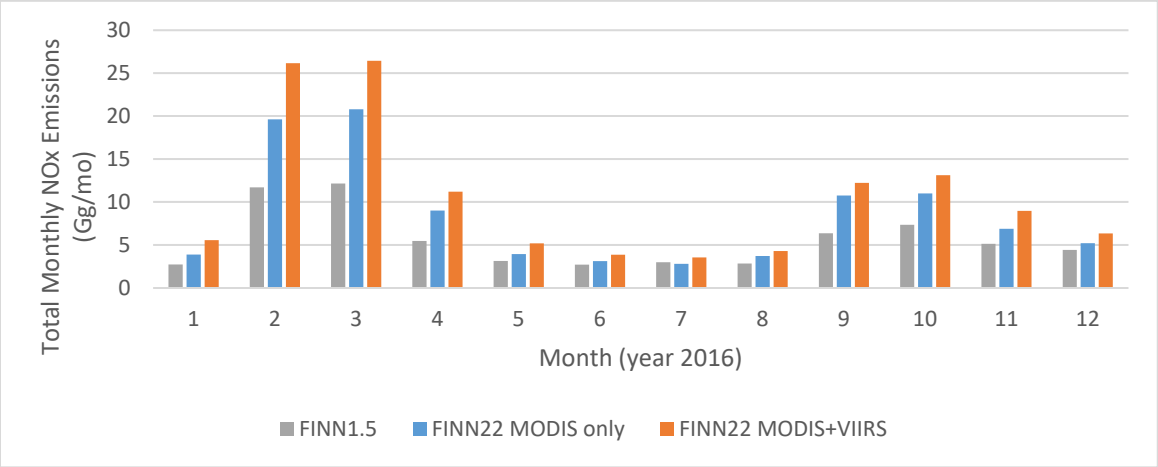

(c)

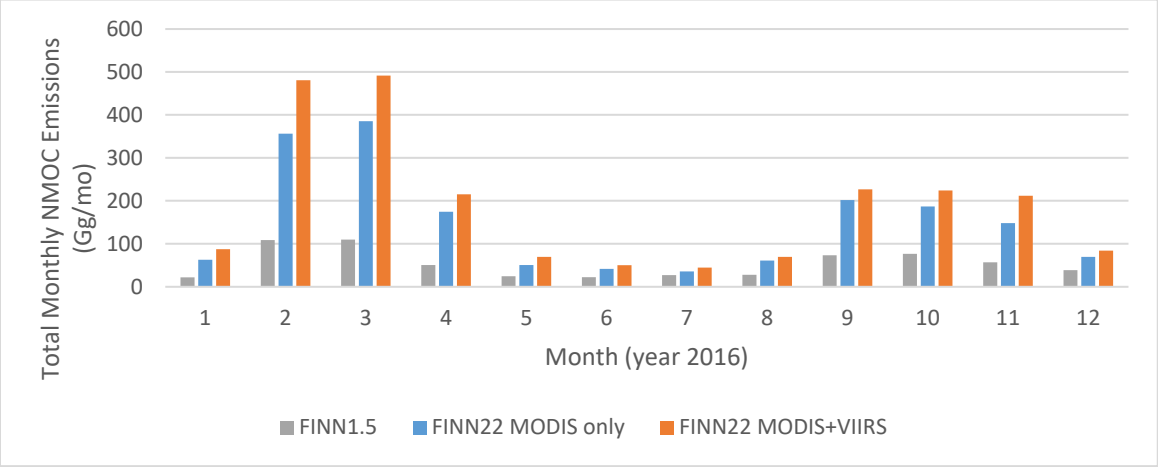

Figure 20. March monthly total $PM_{2.5}$ emissions ($Mg/km^2/mo$) in the Southeastern U.S. and Lower Mississippi Valley from FINNv.1.5, FINNv2.2 with MODIS only fire detections, and FINNv2.2 with MODIS and VIIRS fire detections.

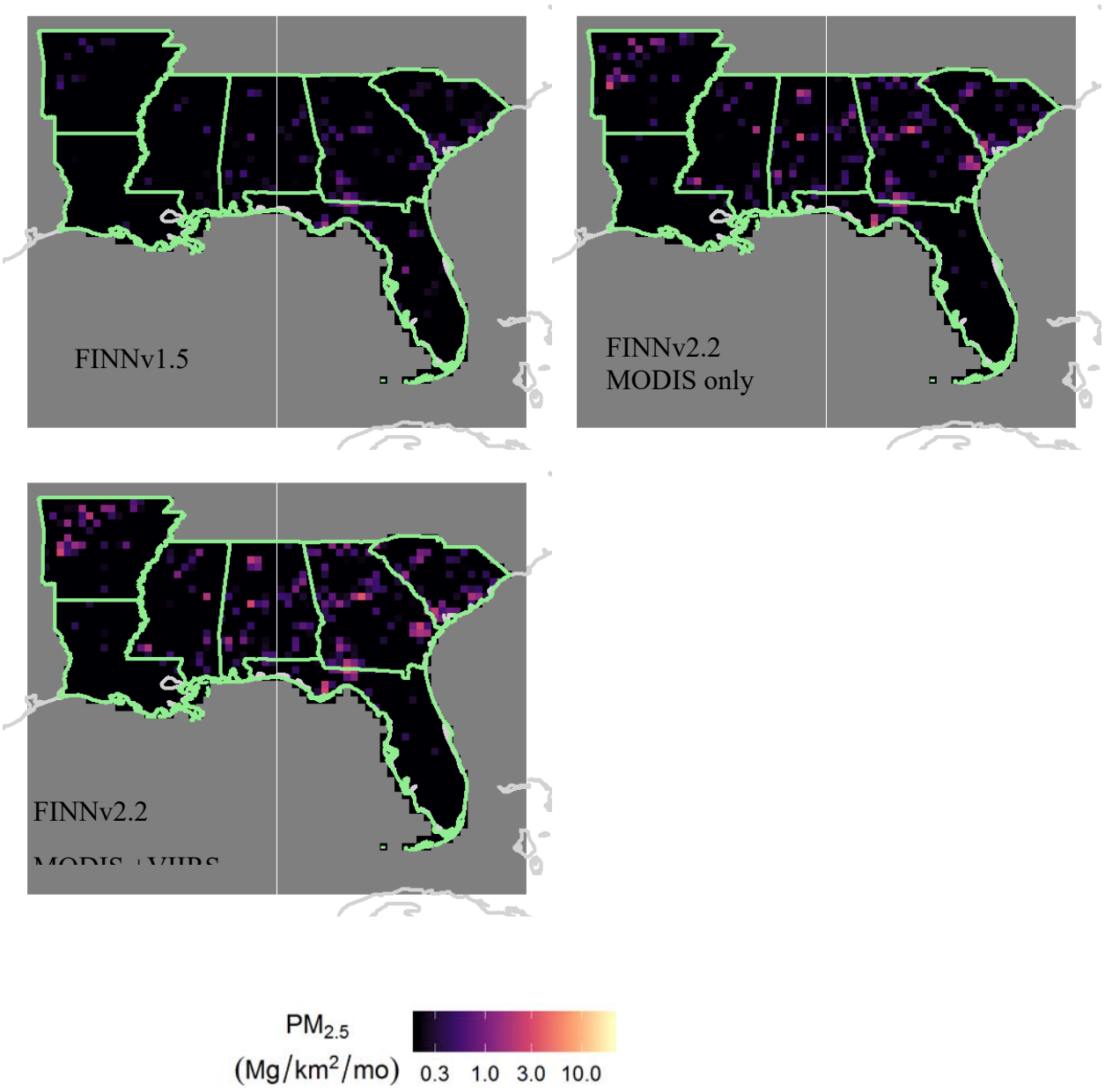

Figure 21. Contribution of land cover type to area burned, biomass loading, and total monthly CO, NMOC, NO_x, and $PM_{2.5}$ emissions in the Southeastern U.S. and Lower Mississippi Valley from FINN v2.2 with MODIS only or in combination with VIIRS fire detections during (a) March and (b) September 2016. Contributions are normalized by the values for FINNv1.5. Land cover types shown include tropical forest, temperate forest, evergreen forest, shrublands, grasses, and croplands. Note differences in scales between plots.

(a)

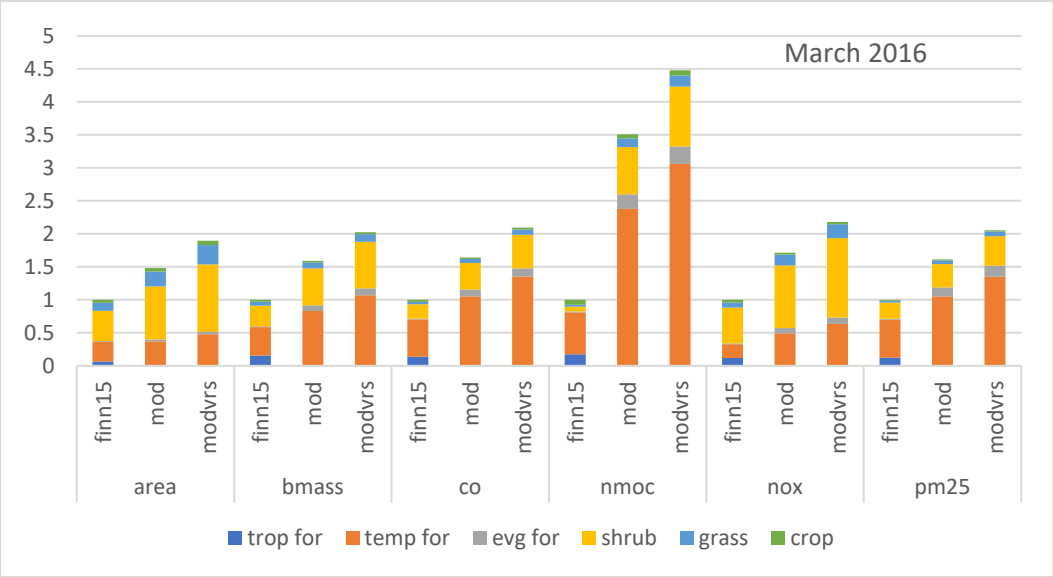

(b)

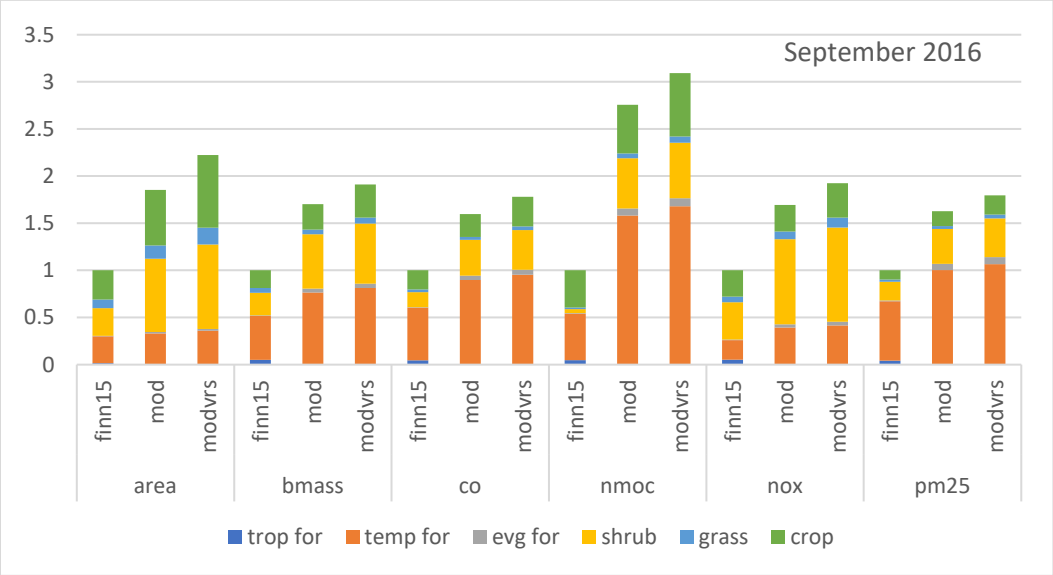

Figure 22. Monthly total (a) $PM_{2.5}$, (b) NO_x and (c) NMOC emissions estimates in 2016 in Mexico by FINNv.1.5, FINNv2.2 with MODIS only fire detections, and FINNv2.2 with MODIS and VIIRS fire detections. Note differences in scales between plots.

(a)

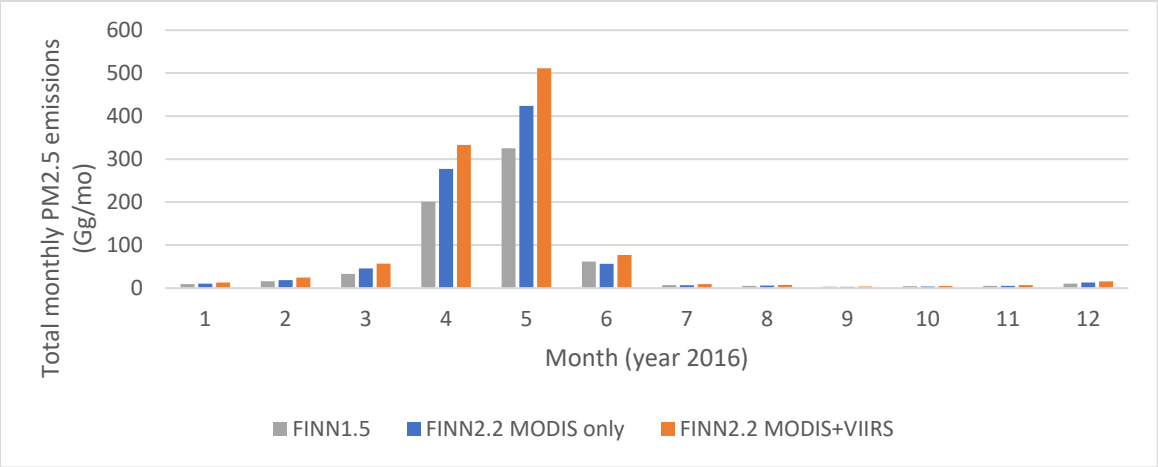

(b)

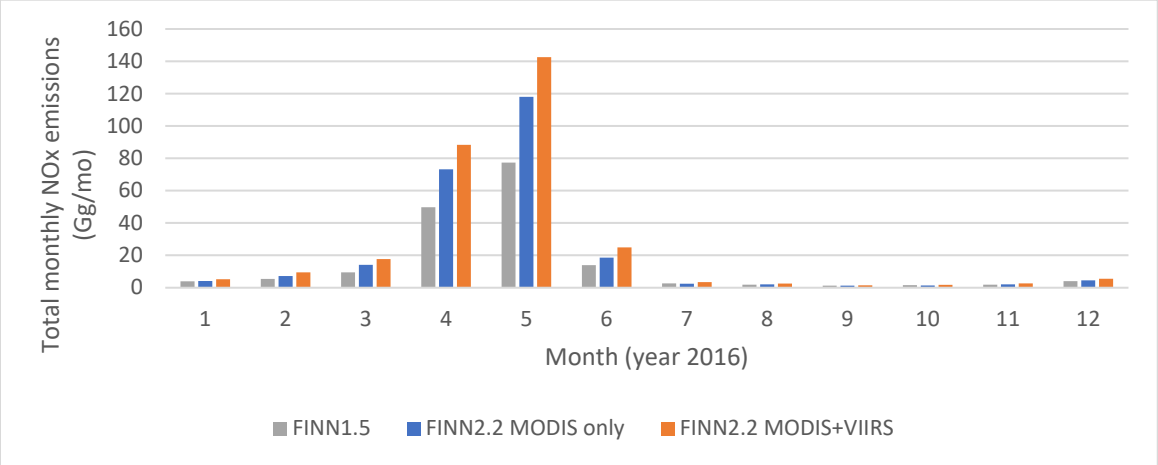

(c)

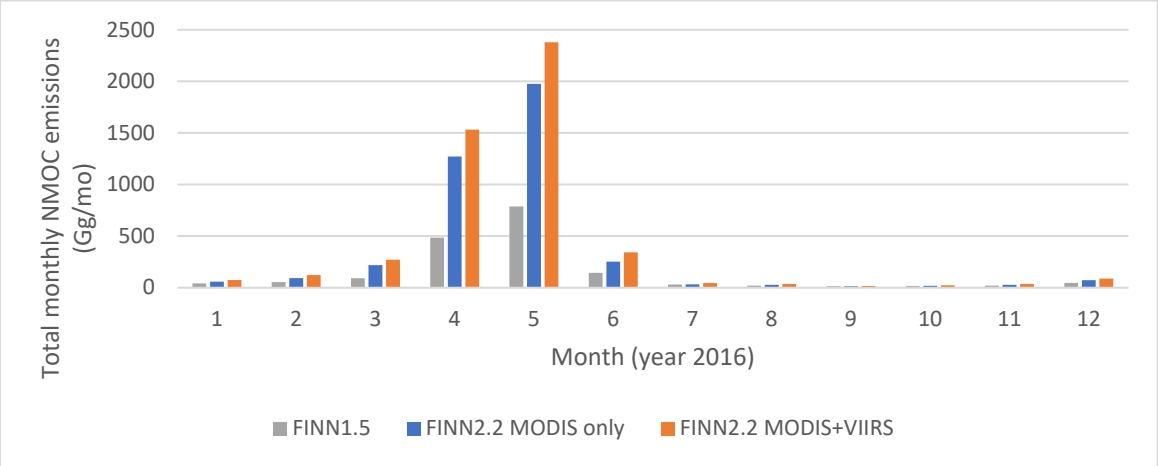

Figure 23. May monthly total $PM_{2.5}$ emissions ($Mg/km^2/mo$) in Mexico from FINNv.1.5, FINNv2.2 with MODIS only fire detections, and FINNv2.2 with MODIS and VIIRS fire detections.

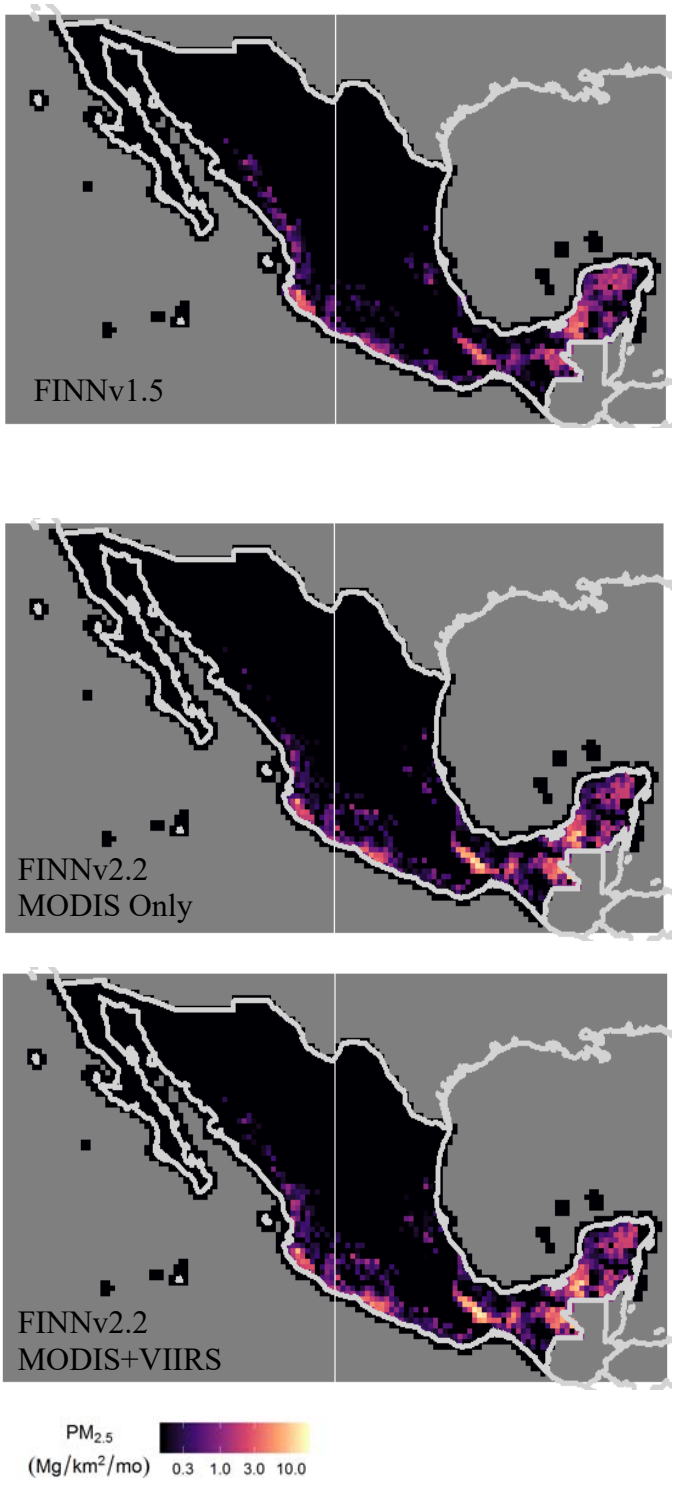

Figure 24. Contribution of land cover type to area burned, biomass loading, and total monthly CO, NMOC, NO_x, and $PM_{2.5}$ emissions in Mexico from FINN v2.2 with MODIS only or in combination with VIIRS fire detections during May 2016. Contributions are normalized by the values for FINNv1.5. Land cover types shown include tropical forest, temperate forest, evergreen forest, shrublands, grasses, and croplands. Note differences in scales between plots.

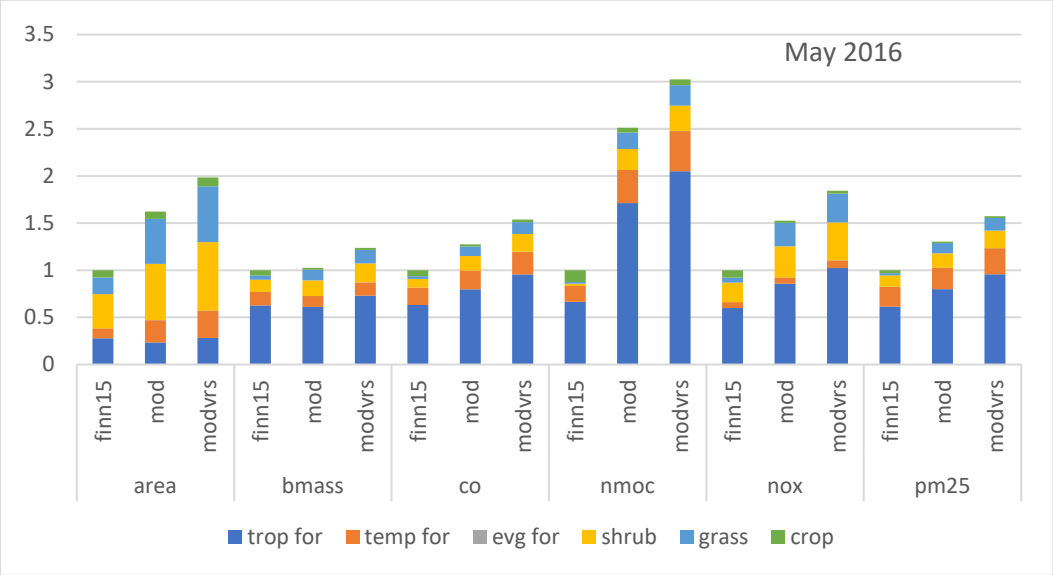

5. Assessment of FINN Performance Using Satellite Observations

Comparisons between modeled aerosols and satellite-observed aerosols were performed to evaluate model performance. Satellite data were obtained and prepared using the approach described in Section 5.1. The model evaluation was performed using both qualitative and quantitative approaches:

1. A qualitative approach involved in-depth assessment of the agreement between modeled aerosols and satellite observations, based on examination of spatial patterns for selected fire events that impacted Texas and daily and monthly trends in aerosols. Graphical evaluation tools such as time series plots, scatter plots, quantile-quantile plots, spatial error plots, soccer plots, and bugle plots will be used.
2. A quantitative approach using statistical measures of agreement between modeled and observed aerosols, including statistics including correlation (R), coefficient of determination (R^2), normalized mean square error (NMSE), bias (FB), and the fraction of data where predictions are within a factor of two of observations (FAC2) (Chang and Hanna, 2004).

Formulas for the quantitative measures of agreement include:

$$R = \frac{\overline{(C_o - \overline{C_o})(C_p - \overline{C_p})}}{\sigma_{C_p}\sigma_{C_o}} \quad (5)$$

$$NMSE = \frac{\overline{(C_o - C_p)^2}}{\overline{C_p}\,\overline{C_o}} \quad (6)$$

$$FB = \frac{(\overline{C_o} - \overline{C_p})}{0.5(\overline{C_p} + \overline{C_o})} \quad (7)$$

FAC2= fraction of data that satisfy

$$0.5 \leq \frac{C_p}{C_o} \leq 2.0 \quad (8)$$

where:

C_p: model prediction,

C_o: satellite observations,

$\bar{C}$: mean of data, and

σ_c: standard deviation of the data

Due to a variety of sources of uncertainty, such as input meteorology or error in satellite retrievals, observations and model results were expected to show substantial divergence. Generally, an air quality dispersion model can be judged to have performed well if the modeled

concentrations agree with surface measurements such that the FAC2 is greater than 50%, the relative mean bias is with about 30% or less, and the normalized mean square error is less than a factor of three (Chang and Hanna, 2004). In this analysis, performance measured were possibly somewhat lower due to the additional uncertainty introduced by the use of satellite observations rather than surface measurements.

5.1 MAIAC Satellite Observations of AOD

The MAIAC AOD data set presents a key new opportunity to assess wildfire smoke emissions. MAIAC has finer spatial resolution than other AOD products from MODIS, is tuned to prevent masking of smoke as cloud (Lyapustin et al., 2012), and effectively retrieves AOD over a broad range of land cover types. For this work, MAIAC AOD data (MCD19A2v006) were obtained from the US Geological Survey Land Processes Distributed Active Archive Center (LP DAAC) data archive.

MODIS images are generally collected twice daily, once in the morning by the instrument onboard the NASA Terra satellite and again in the afternoon by the instrument onboard the NASA Aqua satellite. MAIAC retrievals are calculated from using MODIS images. In addition to AOD retrievals, MAIAC provides metadata on data quality. For data used in this work, AOD retrieval values were screened to ensure that only high-quality pixels were retained in subsequent analysis (Lyapustin et al., 2018). During the QA process, it was noted that the algorithm associated with screening out cloud-influenced data also frequently screens out AOD values over fires (see Section 6.2 for more details). The exclusion of AOD data directly over fires suggests that the analysis of model data versus observed MAIAC AOD data in the subsequent sections is only valid for downwind wildfire plumes, which may bias our comparison values low. MAIAC data are provided in tiled format. Tiles were merged on an hourly basis for subsequent analysis. For areas of overlap within the hour, values were averaged across all available observations. All comparisons with model data were performed using the same hourly between the model and satellite data sets. Table 9 provides the AOD QA definitions and quality flags used to screen AOD retrievals for subsequent use (see Section 6 for additional data quality information).

Table 9**.** AOD QA definitions and quality flags used to screen AOD retrievals for subsequent use. AOD values were retained for retrievals with quality flags shown in bold.

Bits	Type	Codes
0-2	Cloud Mask	**000 – Undefined** **001 – Clear** 010 – Possibly cloudy (detected by AOD filter) 011 – Cloudy (detected by cloud mask algorithm) 101 – Cloud shadow 110 – Hot spot of fire 111 – Water Sediments
3-4	Land-water snow/ice mask	**00 – Land** **01 – Water** 10 – Snow 11 – Ice
5-7	Adjacency mask	**000 – Clear** 001 – Adjacent to clouds 010 – Surrounded by more than 8 cloudy pixels **011 – Adjacent to a single cloudy pixel** 100 – Adjacent to snow 101 – Snow was previously detected in this pixel
8-11	QA for AOD over land and water	**0000 – Best quality** 0001 – Water sediments are detected (water) **0011 – There is one neighboring cloud** 0100 – There is > 1 neighboring clouds 0101 – No retrieval (cloudy or other) 0110 – No retrievals near detected or previously detected snow 0111 – Climatology AOD (0.02): altitude above 4.2 km (Land)/3.5 km (water) 1000 – No retrieval due to sun glint over water 1001 – Retrieved AOD is very low (0.05) due to glint (water) **1010 – AOD within 2 km from the coastline (may be unreliable)** 1011 – Land, research quality: AOD retrieved but CM is possibly cloudy
12	Glint Mask	**0 – No glint** 1 – Glint (glint angle < 40 degrees)
13-14	Aerosol Model	**00 – Background model (regional)** **01 – Smoke detected** **10 – Dust model (dust detected)**
15		**Reserved**

5.2 Assessment of HYSPLIT Dispersion Results

As detailed in Section 3.3, the HYSPLIT dispersion model was applied using FINN v2.2 wildfire $PM_{2.5}$ emissions estimates for 2012 through 2017. The HYSPLIT dispersion model provides estimates of the atmospheric particulate mass and spatial distribution due to wildfires. Through the use of relative humidity measurements and the average composition of wildfire $PM_{2.5}$, we were also able to estimate wildfire AOD from the HYSPLIT $PM_{2.5}$ results (as discussed in Section 3.4). These results allow us to compare HYSPLIT results with both ground-based $PM_{2.5}$ and satellite AOD observations. We also compare HYSPLIT AOD results to CAMx v2.2 AOD results to assess the comparability of these models when applied using the same emissions estimates from FINN v2.2.

5.2.1 HYSPLIT Ground-Based Comparison

For ground-based comparison of HYSPLIT results, we compare total unspeciated $PM_{2.5}$ output from HYSPLIT with total carbon (TC) concentrations at IMPROVE sites in and around Texas. TC is calculated as shown in the U.S. EPS RHR Guidance (2016):

$$TC = \left(Elemental\ Carbon + (1.8 * Organic\ Carbon)\right)\ \ [\frac{\mu g}{m^3}] \qquad (9)$$

TC can be used as a proxy for the biomass burning portion of $PM_{2.5}$ because wildfire particulate matter is comprised of up to 80% organic carbon (Clarke et al., 2007; US EPA RHR Guidance, 2016; McClure and Jaffe, 2018). Also, because IMPROVE sites are in generally low population areas, concentrations of TC are less likely to be influenced by anthropogenic emissions. Therefore, TC at IMPROVE sites is expected to correlate more closely than total $PM_{2.5}$ with $PM_{2.5}$ from wildfires. The comparison of IMPROVE TC and HYSPLIT wildfire $PM_{2.5}$ allows us to assess our ability to reproduce wildfire $PM_{2.5}$ at the surface. We used TC data from 10 sites in and around Texas (including New Mexico, Oklahoma, Arkansas, and Louisiana). Table 10 shows a list of the IMPROVE sites used and their EPA codes. Each selected site was required to have complete data for 2012 through 2017. When comparing HYSPLIT $PM_{2.5}$ to IMPROVE TC, we only considered cases with non-zero estimated wildfire $PM_{2.5}$ from the HYSPLIT model. The daily sum HYSPLIT $PM_{2.5}$ concentrations were compared with the 24-hour filter-based measurement of TC. Note that these are comparisons of coarse resolution grid average model estimates with point measurements.

Figure 25 shows a histogram of the correlation coefficient found when comparing HYSPLIT $PM_{2.5}$ concentrations to IMPROVE TC concentrations. Summer months were chosen for this comparison to better relate wildfire values of $PM_{2.5}$ and TC. This shows, on average, a correlation coefficient of 0.54 for HYSPLIT $PM_{2.5}$ versus IMPROVE TC. Additionally, Figure 26 shows a detailed comparison of HYSPLIT $PM_{2.5}$ to IMPROVE TC at two sites. Both the Big Bend and Wichita Mountains sites show good correlations between the wildfire $PM_{2.5}$ estimated by the HYSPLIT model and observed TC at the IMPROVE ground site. Values of HYSPLIT $PM_{2.5}$ are significantly higher than TC values due to the comparison approach. Since organic carbon can be up to 80% of the of the wildfire particulate matter composition, and elemental carbon is typically an order of magnitude lower than organic carbon in wildfire events, it is not surprising that the HYSPLIT $PM_{2.5}$ mass is substantially higher than the IMPROVE TC. Inclusion of other $PM_{2.5}$ components from IMPROVE would likely result less bias between HYSPLIT and IMPROVE, but would also be expected to reduce the correlation between the two

due to the impact of other sources at IMPROVE sites. The modest correlation (R^2 = 0.27 to 0.34) between the HYSPLIT $PM_{2.5}$ and IMPROVE TC suggests that the HYSPLIT dispersion model has modest predictive ability to estimate wildfire $PM_{2.5}$ concentrations near the surface with the FINN v2.2 emissions inventory.

5.2.2 HYSPLIT vs. MAIAC Observed AOD Comparison

To further assess the performance of the HYSPLIT dispersion modeling using FINN v2.2 fire emissions inventories, we compared the HYSPLIT AOD results with MAIAC satellite observations and CAMx model outputs (also using FINN v2.2 fire emissions inventories). For the comparison of HYSPLIT versus MAIAC AOD, we resampled MAIAC data from its original resolution up to the HYSPLIT's 50 km resolution. With the modeled concentrations and observations compiled with the same spatial resolution, we can compare the two by domain-wide statistics (i.e., calculating statistics over the whole domain for a given hour) or grid cell-based statistics (i.e., calculating statistics for each grid cell during a specific period time). Due to the sporadic availability of MAIAC data, we have done grid cell statistics over monthly time periods. This ensures, for the most part, that there are enough data points to calculate relevant statistical parameters. Additionally, if any grid cells have less than 20 data points, the statistics are not used due to low data availability. Most grid cells and domain-wide statistics are calculated using the EPA Atmospheric Model Evaluation Tool (AMET) software that was adapted for use with HYSPLIT, MAIAC, and CAMx inputs. The factor of two observations (FAC2) statistic does not come standard with the AMET tool, and was calculated separately as an indicator of the normalized frequency of predications falling with a factor of two (between -50% and +100%) of the observations. This value is calculated as a 1 or 0 metric; either AOD values are within a factor of two of each other (FAC2 = 1), or they are not within a factor of two (FAC2 = 0). This suggests that average FAC2 values will fall between 0 and 1, with a higher fraction of data falling within a factor of two between the data sets as FAC2 increases. Statistics were calculated for HYSPLIT versus MAIAC during the HYSPLIT run time period (January – December 2012, and March – September for 2013-2017).

Table 11 shows the standard model comparison statistics (R, R^2, Fraction Bias [FB], Normalized Mean Square Error [NMSE], and FAC2) for HYSPLIT versus MAIAC data by month. Monthly data are averaged for all years. These statistics show a low correlation between the modeled HYSPLIT AOD and observed MAIAC AOD. Figures 27-28 also show a fairly low correlation between domain-wide HYSPLIT and MAIAC data (average R^2 of 0.15). Additionally, Figures 29-30 show that the FB of HYSPLIT vs. MAIAC values are biased significantly low, while the NMSE values are biased high. This suggests that the error between HYSPLIT and MAIAC values is large, with the HYSPLIT values biased low compared to MAIAC values. Bugle and Q-Q plots shown in Figures 31-32 provide the same result. The large difference between MAIAC and HYSPLIT AOD is not surprising because the MAIAC AOD includes total column contributions from all sources, including dust, anthropogenic aerosol, biogenic secondary organic aerosol, wildfire aerosols, etc., whereas the HYSPLIT values only represents the wildfire $PM_{2.5}$ in the atmospheric column. We expect the HYSPLIT and MAIAC AOD to be well correlated when atmospheric PM is primarily due to wildfire emissions, but not well correlated under non-fire dominated conditions (i.e., most of the time).

Figure 33 shows a time series of HYSPLIT vs. MAIAC correlation coefficients for 2012–2017 with FINN v2.2 fire emission inventory. In Section 4.1.2, it is mentioned that Texas experiences

two wildfire seasons; (1) in the spring, associated with agricultural burning in central/south America and the southern U.S., and (2) during late summer/early fall when weather conditions are hot and dry, causing natural wildfires. These periods correlate well with Figure 34 and Figure 35, which show an increased correlation between MAIAC and HYSPLIT during the spring and late summer/early fall months. This is expected for times when wildfire influence is more prevalent.

5.2.3 HYSPLIT vs. CAMx v2.2 Wildfire-Only Comparison

We also compare HYSPLIT output with CAMx v2.2 results. This comparison allows us to evaluate differences in model results since both models use the same fire emissions inventories (FINN v2.2). Because CAMx v2.2 data were run for April 29th through October 1st, 2012 we are able to evaluate the performance of each model during the active wildfire season. Additionally, CAMx output was calculated at the 4 km nest grid space shown in Figure 6. To adequately compare CAMx and HYSPLIT results, we resampled CAMx data up to the 50 km grid space used by HYSPLIT. We also calculate CAMx v2.2 wildfire-only AOD values by subtracting a "no fire" run of CAMx from the total CAMx v2.2 AOD values. This allows us to compare strictly wildfire AOD values between CAMx and HYSPLIT and avoid the issues noted in the MAIAC versus HYSPLIT analysis.

Table 12 and Figures 36-37 provide a similar analysis to that done for MAIAC versus HYSPLIT data above. Model comparison statistics for monthly CAMx v2.2 wildfire-only vs. HYSPLIT are shown in Table 12. Figures 38-41 show the correlation, FB, NMSE, and other model comparison statistics to illustrate the difference between HYSPLIT and CAMx v2.2 wildfire-only results. From these plots and statistics, we see that HYSPLIT and CAMx v2.2 wildfire-only results show, on average, a modest correlation coefficient (R ~0.5) and low FB between the two models (with HYSPLIT values biased slightly low). The soccer plot in Figure 42 also shows that most of the error and bias between HYSPLIT and CAMx v2.2 wildfire-only values lie within the outer goal, suggesting less than a factor of two difference on average. However, in the scatter plot shown in Figure 42, we do see some values where HYSPLIT is biased high compared to CAMx. This is due to a change from spring to summer where HYSPLIT is biased slightly high in the spring/early summer months to being biased slightly low during the late summer months (see FB values in Table 12). This change could be due to the types of fires that are burning during each season and/or the type of modeling done in HYSPLIT versus CAMx ($PM_{2.5}$-only or multi-species, respectively). Also, FAC2 values show that approximately half of the data between HYSPLIT and CAMx are within a factor of two for all months in 2012. From these statistics we assert that the HYSPLIT and CAMx v2.2 wildfire-only AOD results are in reasonable agreement given largely different modeling methodologies and grid structure.

Table 10. IMPROVE Sites used for TC analysis with HYSPLIT $PM_{2.5}$. The IMPROVE site code is shown on the left, and the EPA site code is shown on the right.

Names	State	Sites	EPA Code	Latitude	Longitude
Big Bend	TX	BIBE1	480430101	29.3	-103.2
Bosque del Apache	NM	BOAP1	350539000	33.9	-106.9
Caney Creek	AR	CACR1	051130003	34.5	-94.1
Guadalupe Mountains	TX	GUMO1	481099000	31.8	-104.8
Salt Creek	NM	SACR1	350059000	33.5	-104.4
Stilwell	OK	STIL1	400719010	35.8	-94.7
Upper Buffalo Wilderness	AR	UPBU1	051019000	35.8	-93.2
White Mountain	NM	WHIT1	350279000	33.5	-105.5
Wheeler Peak	NM	WHPE1	350559000	36.6	-105.5
Wichita Mountains	OK	WIMO1	400319000	34.7	-98.7

Figure 25. Correlation between HYSPLIT $PM_{2.5}$ concentrations and IMPROVE TC concentrations for 10 IMPROVE sites in and around Texas. July through September values were chosen to better compare with wildfire season.

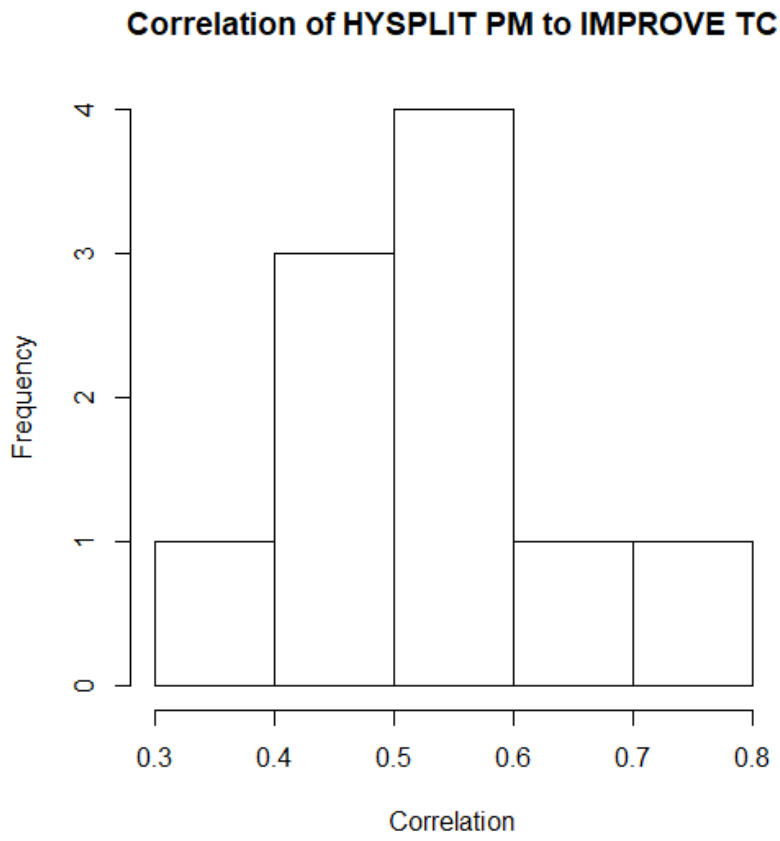

Figure 26. Comparison of daily sum HYSPLIT $PM_{2.5}$ to IMPROVE TC at Big Bend, TX (left), and Wichita Mountains, OK (right), for 2012 through 2017. Linear regression equations and R^2 values for each comparison are shown at the top of the figure.

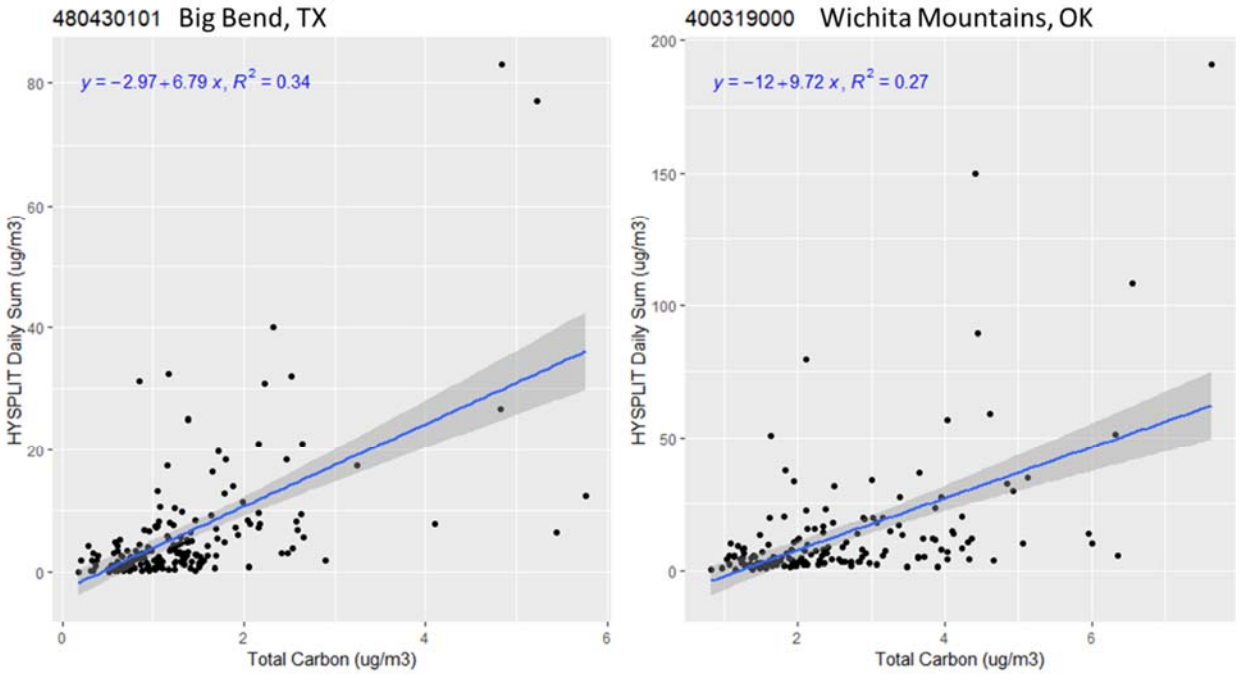

Table 11**.** MAIAC vs. HYSPLIT AOD model comparison statistics. Monthly values are averaged over all years in which monthly data is available (2012 – 2017). Values are provided with ± one standard deviation.

Month	N	Mean MAIAC AOD	Mean HYSPLIT AOD	R	R^2	FB (%)	NMSE	FAC2
1	526	0.062 ± 0.019	0.002 ± 0.004	0.089 ± 0.225	0.058 ± 0.091	-188 ± 15	201 ± 438	0.019 ± 0.135
2	402	0.075 ± 0.026	0.002 ± 0.003	0.125 ± 0.213	0.061 ± 0.094	-190 ± 12	156 ± 192	0.016 ± 0.126
3	476	0.098 ± 0.032	0.006 ± 0.009	0.218 ± 0.251	0.110 ± 0.138	-182 ± 20	178 ± 553	0.028 ± 0.162
4	454	0.121 ± 0.039	0.007 ± 0.010	0.322 ± 0.295	0.190 ± 0.207	-185 ± 14	287 ± 1352	0.015 ± 0.118
5	431	0.137 ± 0.042	0.007 ± 0.008	0.350 ± 0.285	0.204 ± 0.196	-187 ± 10	97 ± 331	0.008 ± 0.090
6	432	0.137 ± 0.047	0.003 ± 0.003	0.252 ± 0.235	0.119 ± 0.133	-192 ± 5	115 ± 242	0.002 ± 0.044
7	327	0.144 ± 0.054	0.003 ± 0.004	0.155 ± 0.216	0.071 ± 0.107	-193 ± 6	190 ± 825	0.002 ± 0.042
8	340	0.135 ± 0.042	0.009 ± 0.015	0.203 ± 0.267	0.112 ± 0.154	-182 ± 18	137 ± 1149	0.021 ± 0.130
9	402	0.099 ± 0.041	0.007 ± 0.011	0.191 ± 0.233	0.091 ± 0.131	-178 ± 19	88 ± 327	0.030 ± 0.165
10	610	0.071 ± 0.021	0.004 ± 0.004	0.046 ± 0.192	0.039 ± 0.062	-179 ± 17	148 ± 523	0.027 ± 0.163
11	592	0.068 ± 0.017	0.004 ± 0.004	0.016 ± 0.211	0.045 ± 0.084	-178 ± 19	114 ± 260	0.034 ± 0.180
12	386	0.062 ± 0.018	0.001 ± 0.001	0.141 ± 0.230	0.072 ± 0.095	-193 ± 7	245 ± 409	0.006 ± 0.079

Figure 27. Domain-wide HYSPLIT AOD values (mean model AOD - left) and MAIAC AOD values (mean observed AOD – bottom) for 2012–2017. Linear regression equations and R^2 values for each comparison are shown at the top of the figure.

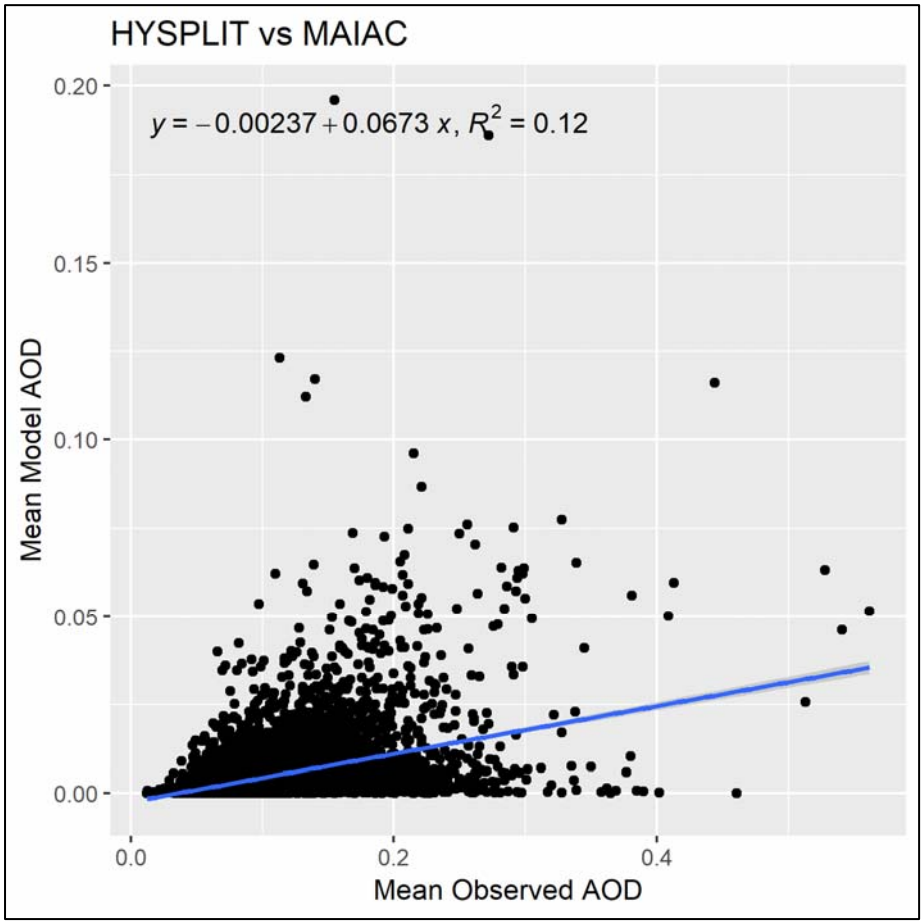

Figure 28. Domain-wide HYSPLIT vs. MAIAC AOD correlation coefficients for 2012 - 2017.

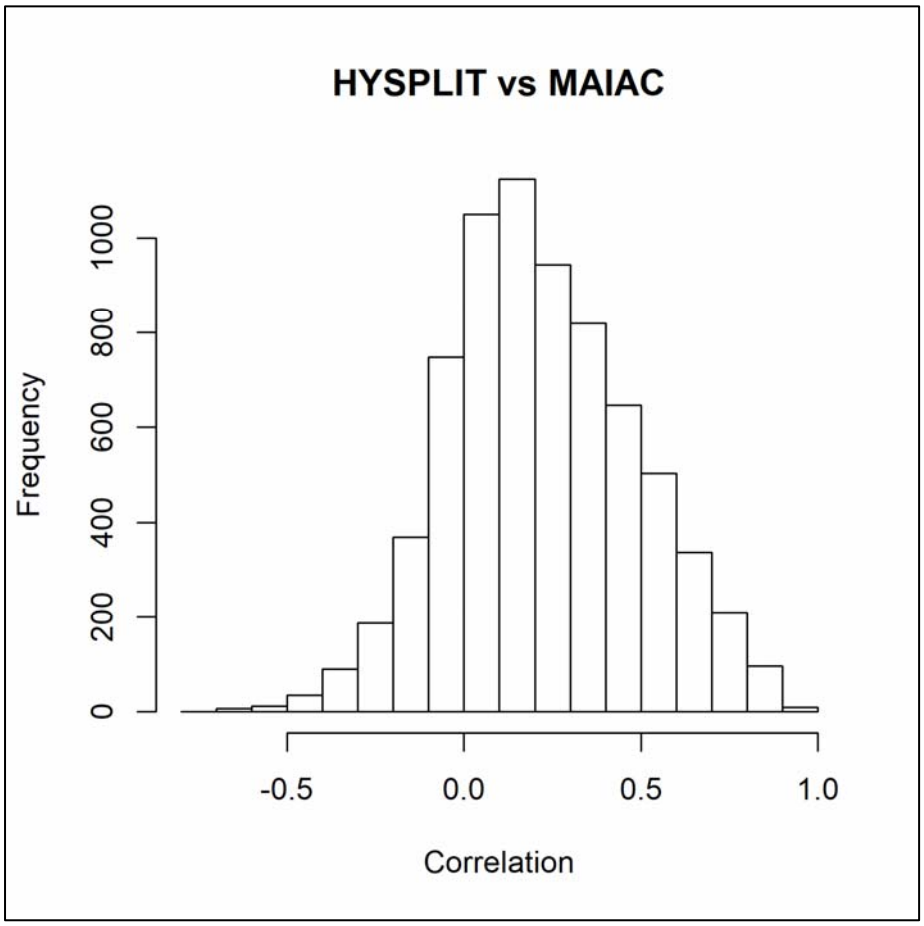

Figure 29. Domain-wide FB histogram of HYSPLIT vs. MAIAC AOD values for 2012-2017.

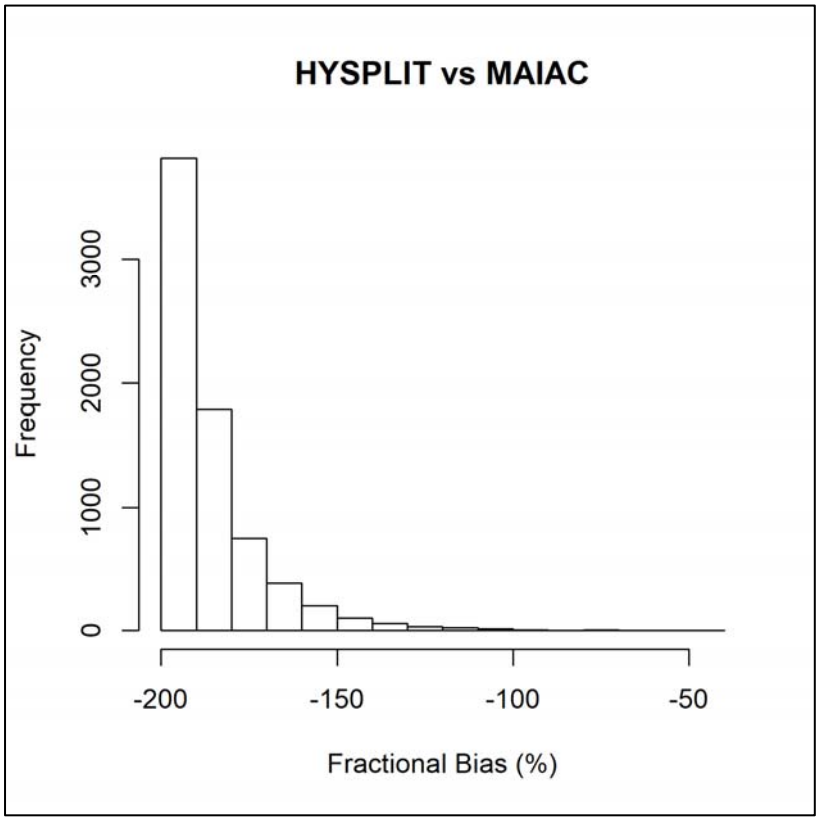

Figure 30. Domain-wide NMSE histogram of HYSPLIT vs. MAIAC AOD values for 2012-2017.

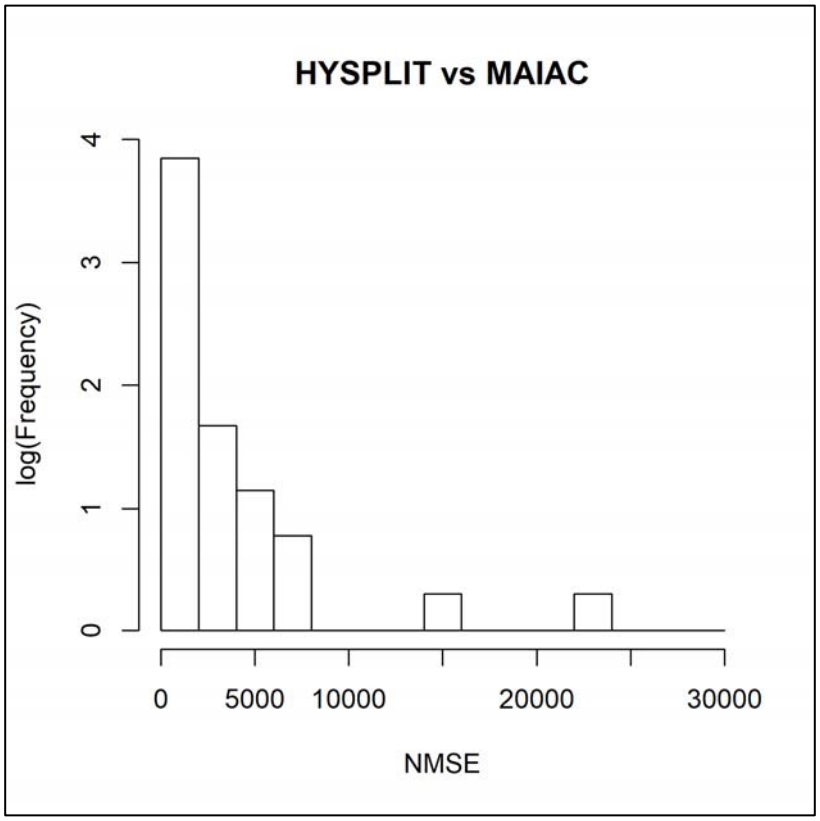

Figure 31. Domain-wide bugle plots of HYSPLIT vs. MAIAC AOD values for 2012-2017 are shown. The fractional bias bugle plot is shown on the left, while the fraction error bugle plot is shown on the right.

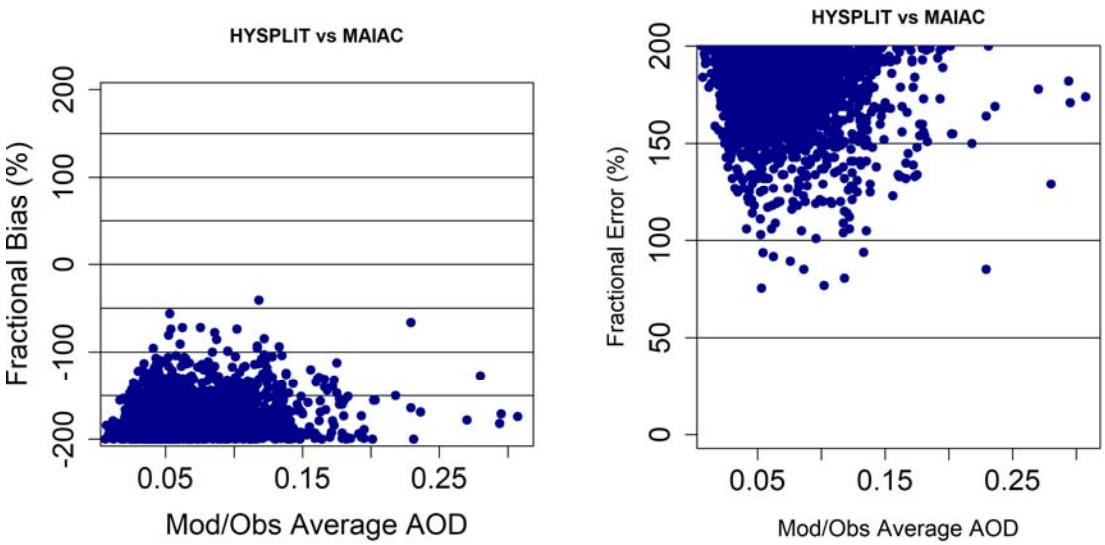

Figure 32. Domain-wide Q-Q plots of HYSPLIT (mean model AOD - left) and MAIAC (mean observational AOD - right) AOD values for 2012-2017.

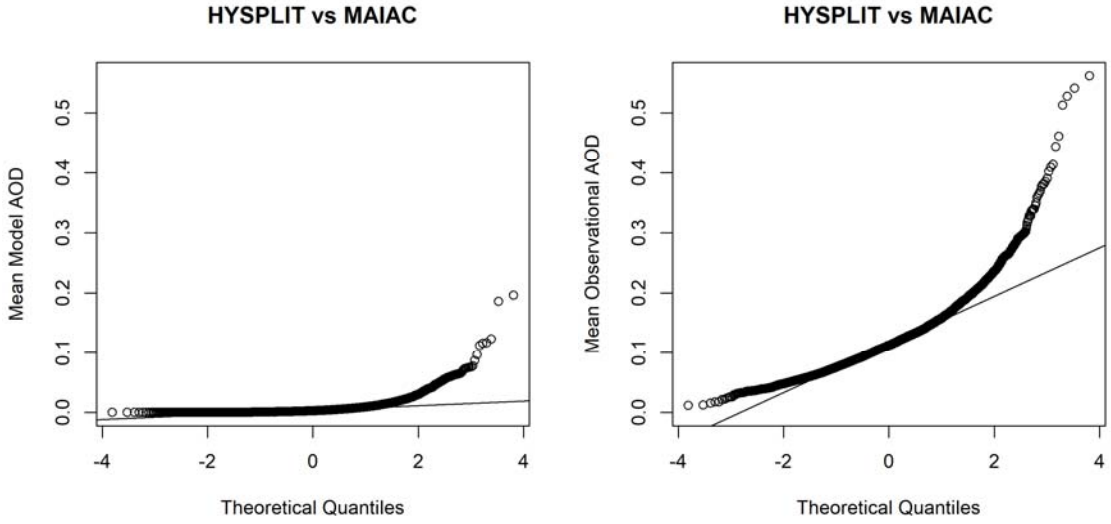

Figure 33. A domain-wide soccer plot of normalized mean error vs. normalized mean bias for HYSPLIT vs. MAIAC AOD data during 2012-2017. Values are colored by the maximum HYSPLIT AOD value in the domain to assess the influence of wildfire smoke on bias and error between the two datasets.

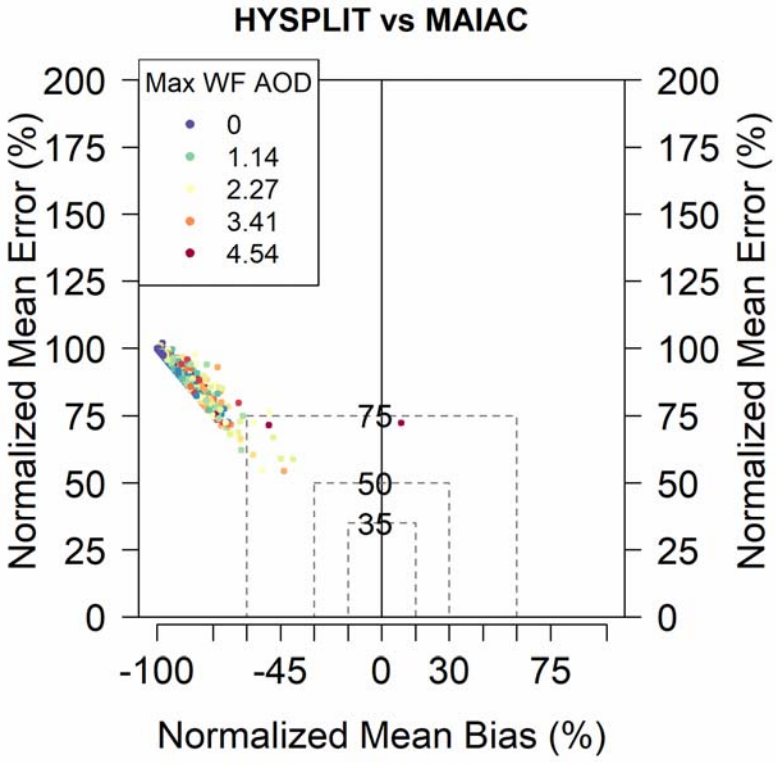

Figure 34. HYSPLIT vs. MAIAC Correlation Coefficient for 2012-2017 shown in top panel. The red line indicates a 3 day moving average of hourly correlation coefficients. Daily sum FINN v2.2 $PM_{2.5}$ fire emissions are shown in the bottom panel.

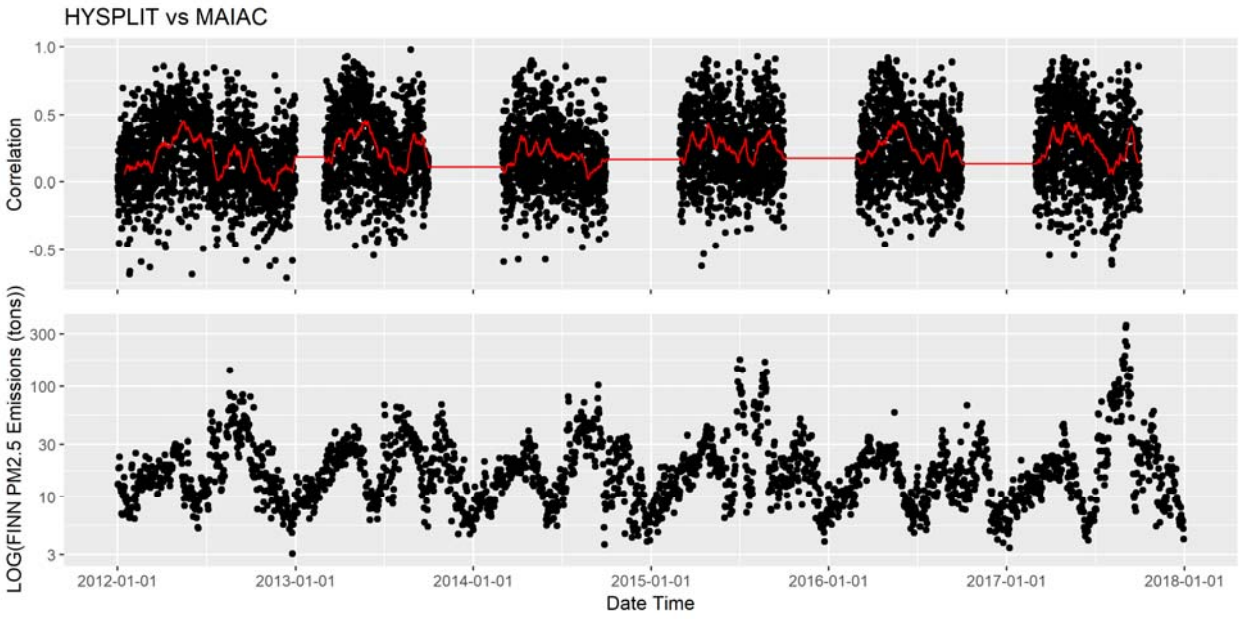

Figure 35. Monthly HYSPLIT vs. MAIAC Correlation Coefficients are shown on the left. Monthly FINN v2.2 emissions are shown on the right for 2012-2017.

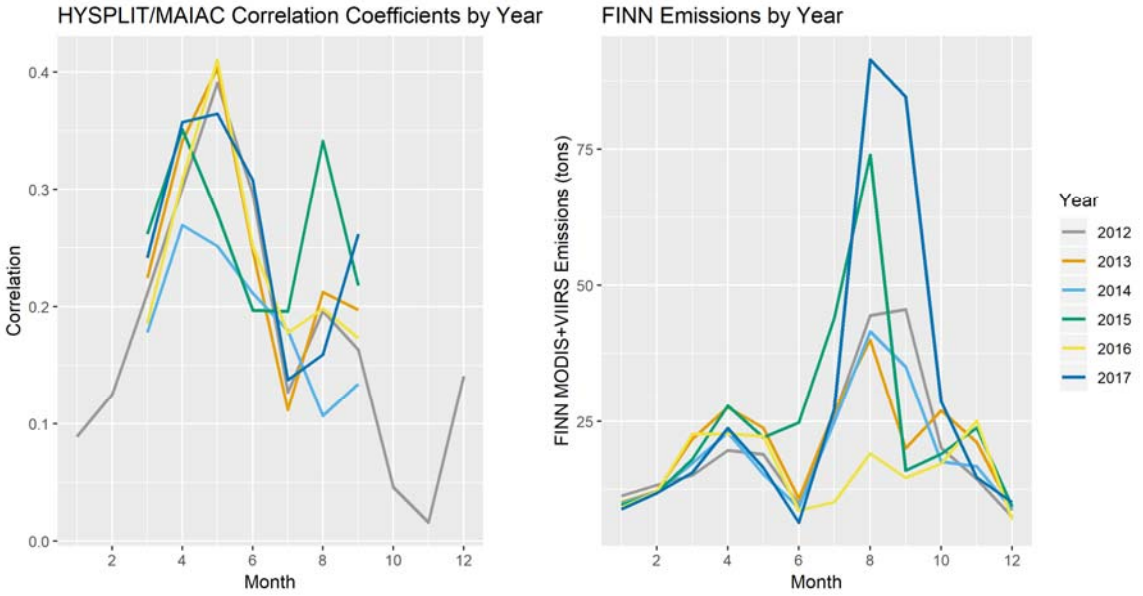

Table 12**.** HYSPLIT vs. CAMx v2.2 WF-only AOD Model Comparison Statistics are shown. Monthly values are averaged hourly data for 2012. Values are provided with ± one standard deviation.

Month	N	Mean CAMx2 WF AOD	Mean HYSPLIT AOD	R	R^2	FB (%)	NMSE	FAC2
5	322	0.007 ± 0.003	0.019 ± 0.020	0.221 ± 0.309	0.144 ± 0.151	33 ± 73	8 ± 11	0.443 ± 0.497
6	322	0.006 ± 0.003	0.008 ± 0.004	0.260 ± 0.256	0.133 ± 0.144	9 ± 41	1 ± 1	0.583 ± 0.493
7	322	0.002 ± 0.001	0.003 ± 0.002	0.314 ± 0.251	0.161 ± 0.152	33 ± 43	3 ± 4	0.363 ± 0.481
8	322	0.006 ± 0.004	0.005 ± 0.003	0.359 ± 0.236	0.184 ± 0.149	-19 ± 41	1 ± 1	0.470 ± 0.499
9	322	0.017 ± 0.012	0.011 ± 0.007	0.497 ± 0.223	0.297 ± 0.170	-47 ± 48	1 ± 1	0.367 ± 0.482

Figure 36. Domain-wide HYSPLIT AOD values (mean model AOD - left) and CAMx v2.2 WF-only AOD values (mean observed AOD – bottom) for 2012. Linear regression equations and R^2 values for each comparison are shown at the top of the figure.

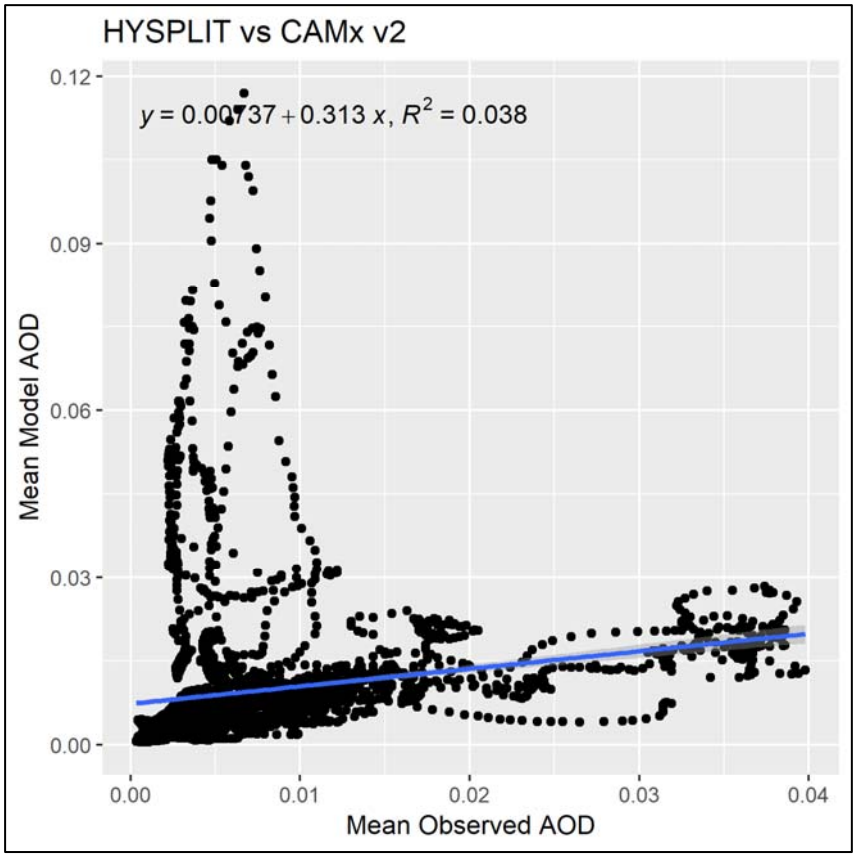

Figure 37. Domain-wide HYSPLIT vs. CAMx v2.2 WF-only AOD correlation coefficients for 2012.

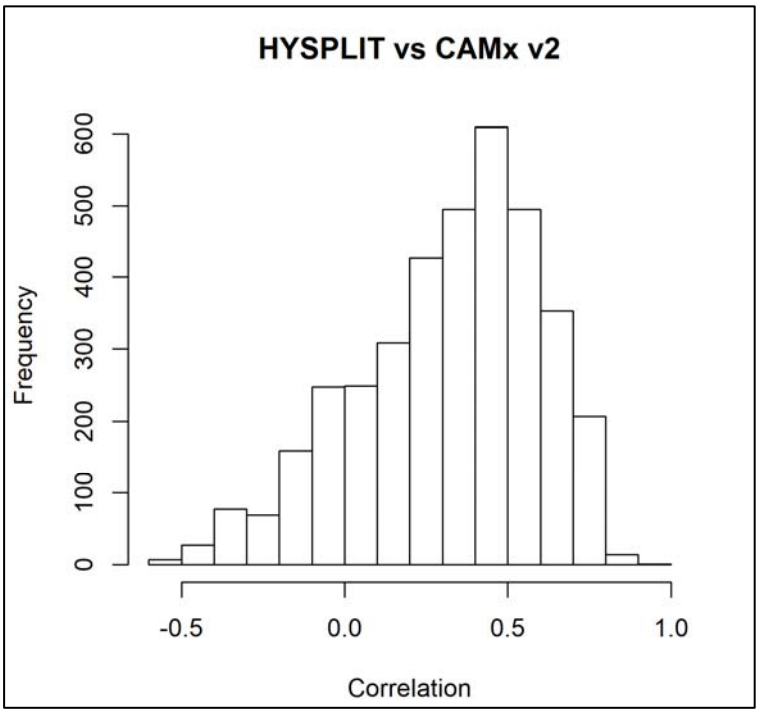

Figure 38. Domain-wide FB histogram of HYSPLIT vs. CAMx v2.2 WF-only AOD values for 2012.

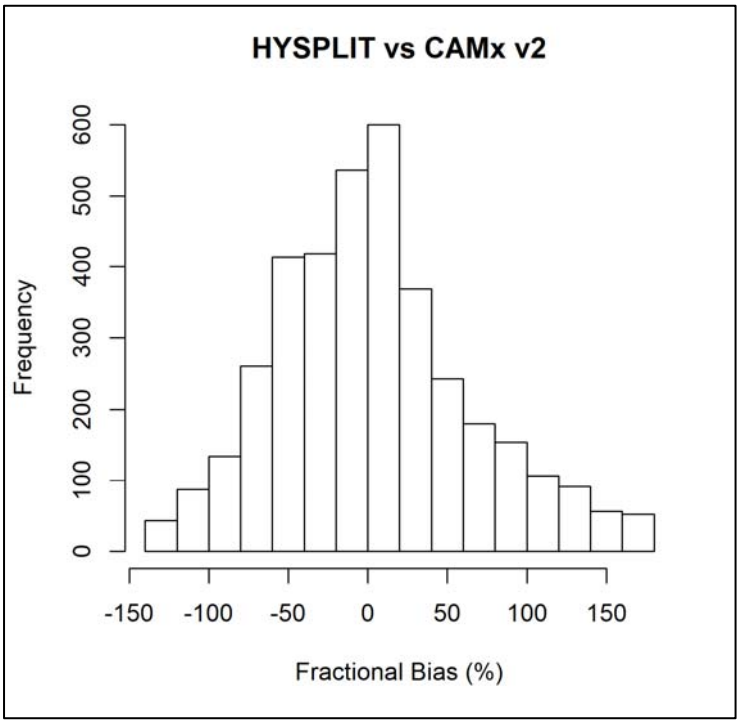

Figure 39. Domain-wide NMSE histogram of HYSPLIT vs. CAMx v2.2 WF-only AOD values for 2012.

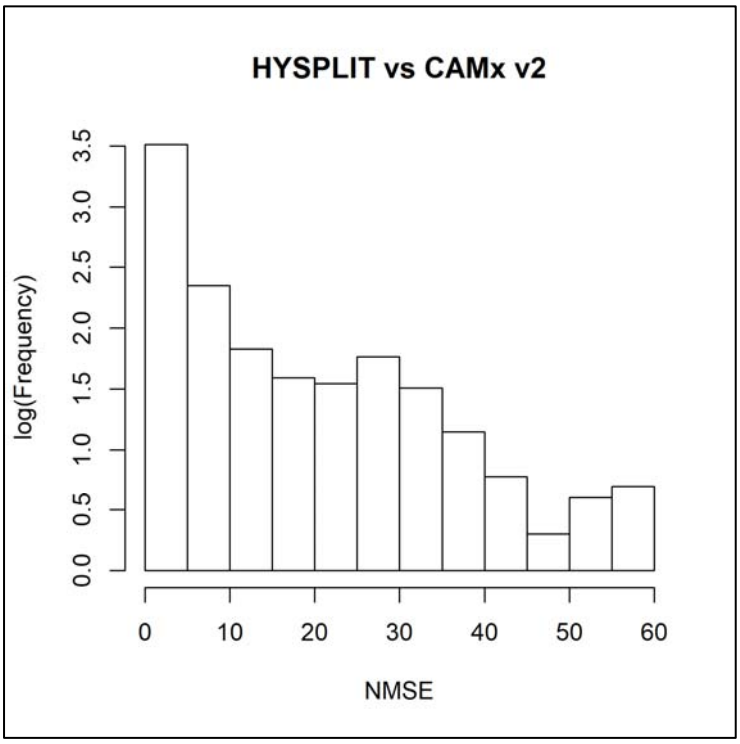

Figure 40. Domain-wide bugle plots of HYSPLIT vs. CAMx v2.2 WF-only AOD values for 2012. The fractional bias bugle plot is shown on the left, while the fraction error bugle plot is shown on the right.

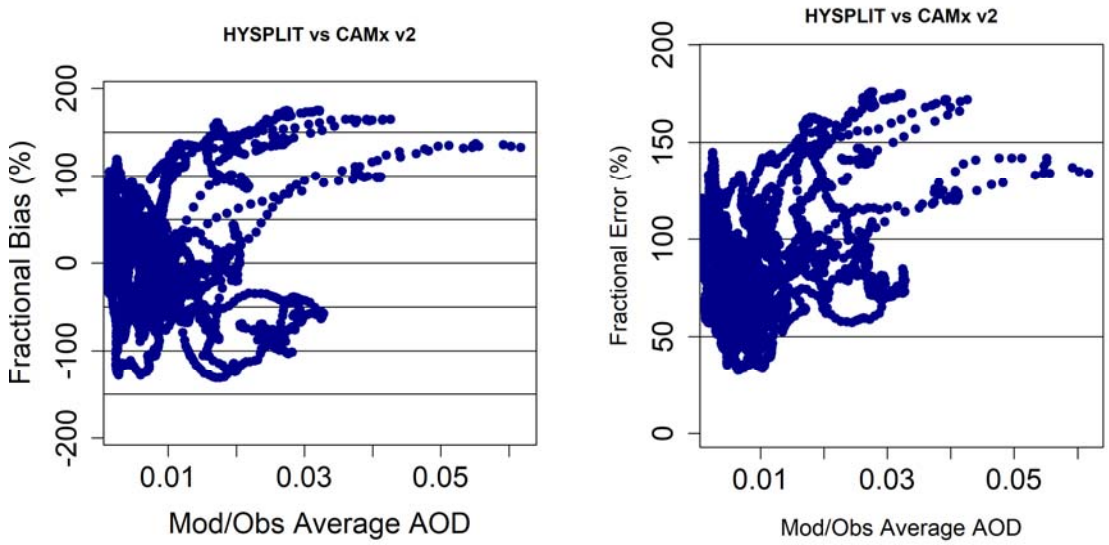

Figure 41. Domain-wide Q-Q plots of HYSPLIT (mean model AOD – left) and CAMx v2.2 (mean observational AOD – right) WF-only AOD values for 2012.

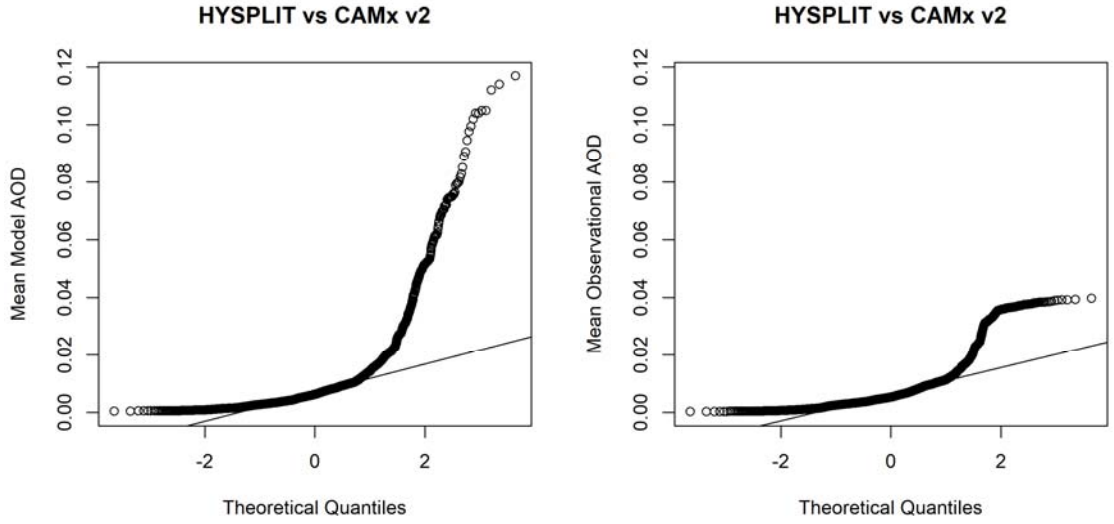

Figure 42. A domain-wide soccer plot of normalized mean error vs. normalized mean bias for HYSPLIT vs. CAMx v2.2 WF-only AOD data during 2012. Values are colored by the maximum HYSPLIT AOD value in the domain to assess the influence of wildfire smoke on bias and error between these two datasets.

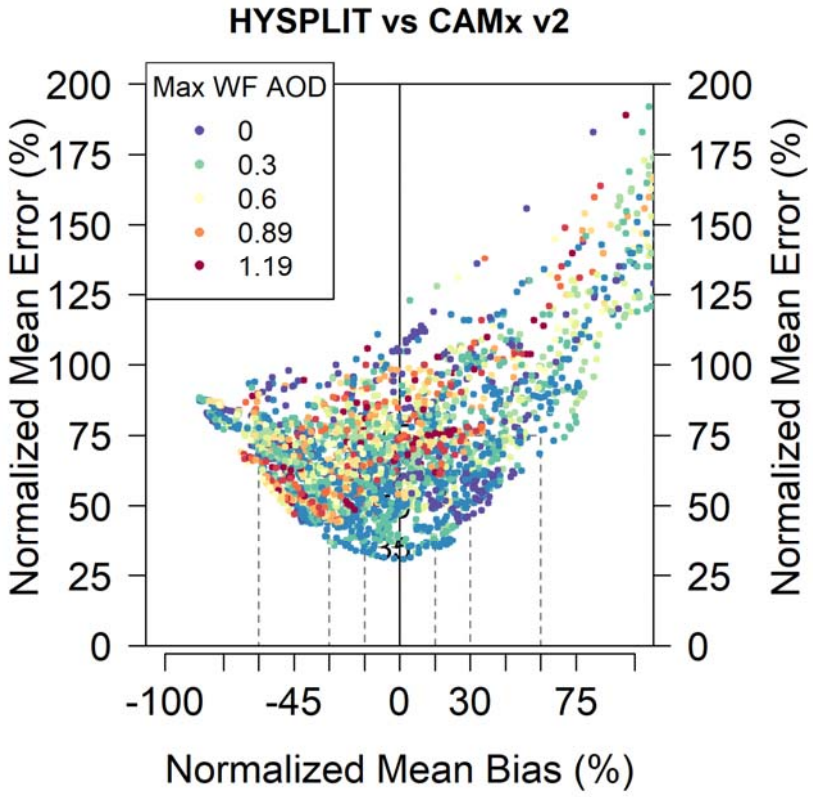

5.3 Assessment of CAMx Model Results

We assessed the CAMx model results by comparing total CAMx AOD versus MAIAC observed AOD values. While total CAMx results include wildfire influence from the addition of the FINN v1.5 or v2.2 fire emission inventories, CAMx also includes other non-fire related sources for a total column AOD that can be compared objectively with MAIAC observed values. CAMx wildfire-only results (as described in Section 5.2.3) were also compared with HYSPLIT results during wildfire-influenced periods to assess the ability of the model to accurately represent fire influences.

As the comparison of HYSPLIT versus CAMx v2.2 wildfire-only were already discussed in Section 5.2.3, we will not discuss them again here. We will briefly note that a comparison of HYSPLIT versus CAMx v1.5 wildfire-only AOD was conducted, and results were nearly identical to the results with CAMx v2.2 (see Appendix B for additional figures and tables). In Section 5.3.1, we discuss the difference in the CAMx v2.2 and v1.5 in comparison with MAIAC observed values to assess how changes made to CAMx v2.2 influences overall results. CAMx data are compared with HYSPLIT and MAIAC data during the period in which the CAMx

model was run—April 29 through October 1, 2012—within the 4 km nested grid space shown in Figure 6.

5.3.1 CAMx vs. MAIAC comparison

CAMx v2.2 total AOD are compared to observed MAIAC AOD values to assess overall model performance. In a similar to fashion to the comparisons discussed in Sections 5.2.2 and 5.2.3, Table 13 and Figures 43-48 provide domain-wide statistical comparisons between CAMx v2.2 and MAIAC AOD for 2012. Based on the statistics shown in Table 13, we find that CAMx is often biased high (FB values) for all months; however, NMSE values remain low during all time periods. Additionally, FAC2 values show that MAIAC and CAMx values are within a factor of two around 50% of the time. The scatter plot in Figure 43 shows a relative low bulk domain-wide correlation between MAIAC and CAMx AODs. The soccer and bugle plots in Figure 46 shows a relatively low error between the two datasets, with a decreasing error at higher AOD values. This suggests that although low AOD values between the CAMx and MAIAC datasets are not well correlated, at high higher AOD values (high smoke, dust, etc.), these events are well corroborated. These bulk statistics were also tested for total CAMx v1.5 AOD versus MAIAC and were found to be very similar. Figures and tables for CAMx v1.5 versus MAIAC results can be found in Appendix C.

When comparing MAIAC versus CAMx v2.2 results, on average, higher FAC2 results were seen over water compared with land. This could be due to more accurate (or biased high) MAIAC AOD retrievals over a surface that is less cloudy and has less seasonal reflectivity changes compared with land. An example of this is shown in Figure 49. This figure shows the average monthly FAC2 values for MAIAC versus CAMx v2.2 in each grid cell within the 4 km nested grid area. However, when compared with R^2 values in each grid cell for the same month, we see a similar frequency of higher R^2 values over land and sea (with slightly more high R^2 values over land) – see Figure 50.

Overall, we find that total CAMx modeled AOD values are biased high when compared with MAIAC-observed AOD values. Additionally, CAMx values are closer to the respective MAIAC AOD values over water, but the correlation between the two datasets in similar for land or sea. Finally, we see most of the variability in CAMx and MAIAC values at low AODs; the bias and error between the two dataset decreases with increasing AOD.

5.3.2 CAMx v2.2 versus CAMx v1.5

To assess the changes in CAMx v2.2 versus v1.5, we compare total CAMx results from both versions with MAIAC observed AOD. Figure 51 shows a time series of hourly, domain-averaged MAIAC and total CAMx data for 2012. As mentioned in Section 5.3.1, CAMx values are biased high compared with MAIAC values. Also, while low MAIAC AODs do not compare well with CAMx modeled AODs, higher MAIAC AOD values are better reproduced. Additional information in this figure shows that CAMx v2.2 values are individually slightly higher overall than the previous CAMx v1.5 AODs for the same time period, but follow the same general pattern. When comparing bulk total CAMx AODs from v2.2 and v1.5 versus MAIAC values (see Figure 52), we see again that the two version of CAMx show an almost identical correlation and slope, with individual values being slightly higher in the CAMx v2.2 compared with v1.5.

To compare CAMx results for wildfire events specifically, we can estimate when and where we see wildfire influence using CAMx wildfire-only AODs (discussed in in Section 5.2.3). If we filter all CAMx total and MAIAC data for times when the CAMx wildfire-only values are above the 75th percentile, we can assume that these times are likely affected by wildfire smoke. Since the CAMx wildfire-only product is already subset for wildfires, we choose the 75th percentile to capture times when wildfire AOD is elevated, but not so high that we filter out a significant portion of the data. This suggests that when the 75th percentile of CAMx wildfire-only AODs cutoff is applied to coinciding total CAMx and MAIAC data, we are filtering for wildfire "likely" events in those datasets. Figure 53 shows the results of this analysis. During wildfire events, the bulk CAMx v2.2 performs slightly better than CAMx v1.5—in both correlation and slope—to the observed MAIAC AOD values. Additionally, it appears that CAMx overestimated the MAIAC-observed AOD values slightly more in CAMx v2.2 versus v1.5 during the wildfire events. This is consistent with the previous bulk comparison. While the bulk comparison of the two CAMx version is very similar, we will also compare case studies in Section 5.4 to further explore variability in CAMx v2.2 versus v1.5 at hourly time scales.

Table 13. MAIAC vs. CAMx v2.2 AOD model comparison statistics. Monthly values are averaged hourly data for 2012. Values are provided with ± one standard deviation.

Month	N	Mean MAIAC AOD	Mean CAMx2 AOD	R	R^2	FB (%)	NMSE	FAC2
5	6710	0.179 ± 0.066	0.266 ± 0.038	0.137 ± 0.294	0.104 ± 0.142	48 ± 37	0.517 ± 0.510	0.587 ± 0.492
6	6613	0.169 ± 0.068	0.275 ± 0.040	0.164 ± 0.290	0.110 ± 0.150	57 ± 34	0.569 ± 0.513	0.567 ± 0.495
7	5436	0.155 ± 0.082	0.244 ± 0.031	0.061 ± 0.264	0.073 ± 0.100	60 ± 43	0.778 ± 0.856	0.379 ± 0.485
8	7430	0.152 ± 0.054	0.248 ± 0.027	0.120 ± 0.256	0.079 ± 0.095	56 ± 33	0.576 ± 0.533	0.534 ± 0.499
9	10635	0.123 ± 0.056	0.265 ± 0.042	0.202 ± 0.257	0.106 ± 0.129	82 ± 33	1.197 ± 1.148	0.267 ± 0.442

Figure 43. Domain-wide CAMx v2.2 AOD values (mean model AOD - left) and MAIAC AOD values (mean observed AOD – bottom) for 2012. Linear regression equations and R^2 values for each comparison are shown at the top of the figure.

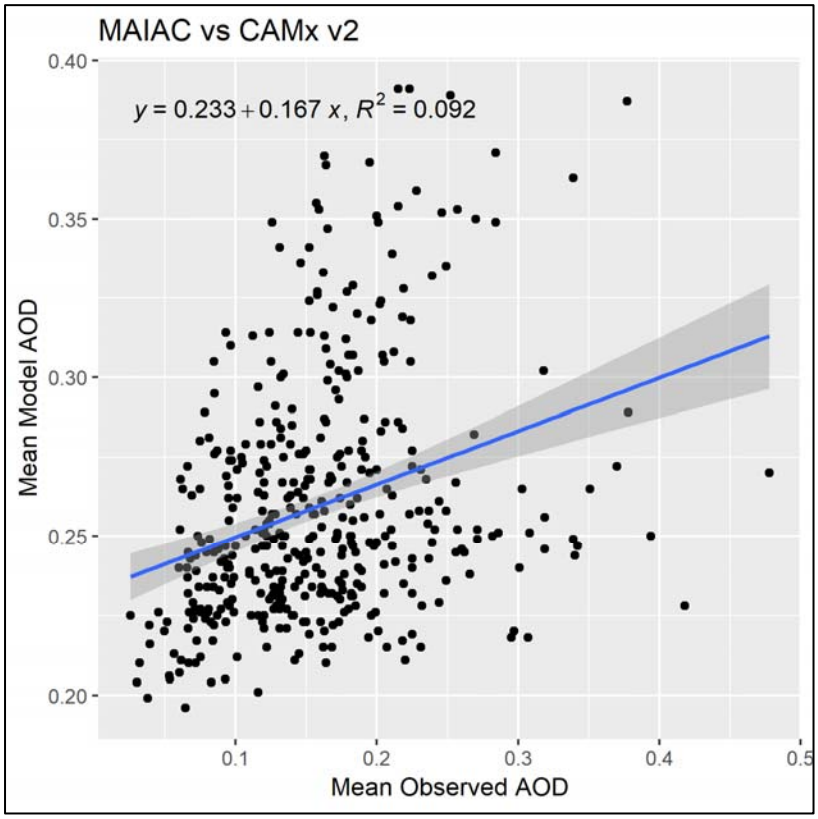

Figure 44. Domain-wide FB histogram of MAIAC vs. CAMx v2.2 AOD values for 2012.

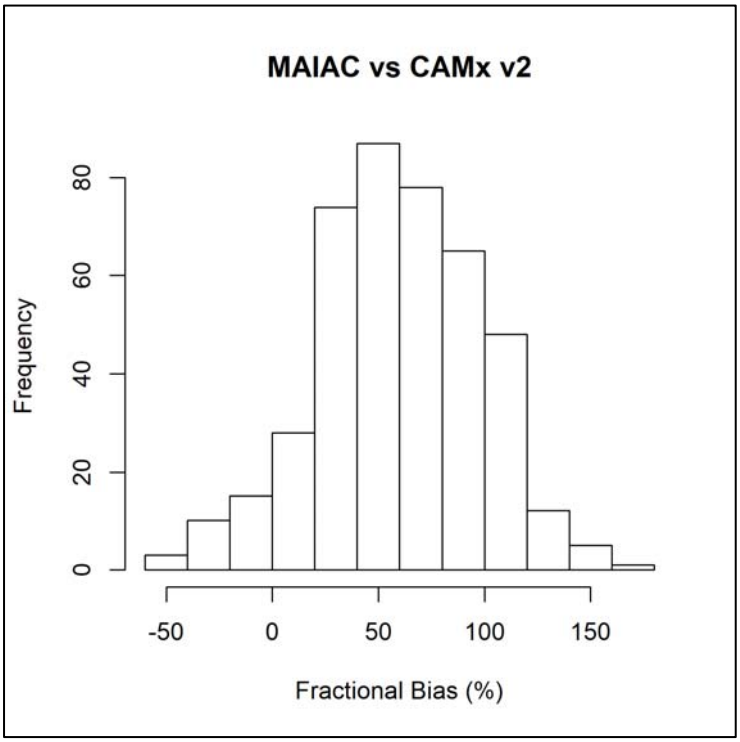

Figure 45. Domain-wide NMSE histogram of MAIAC vs. CAMx v2.2 AOD values for 2012.

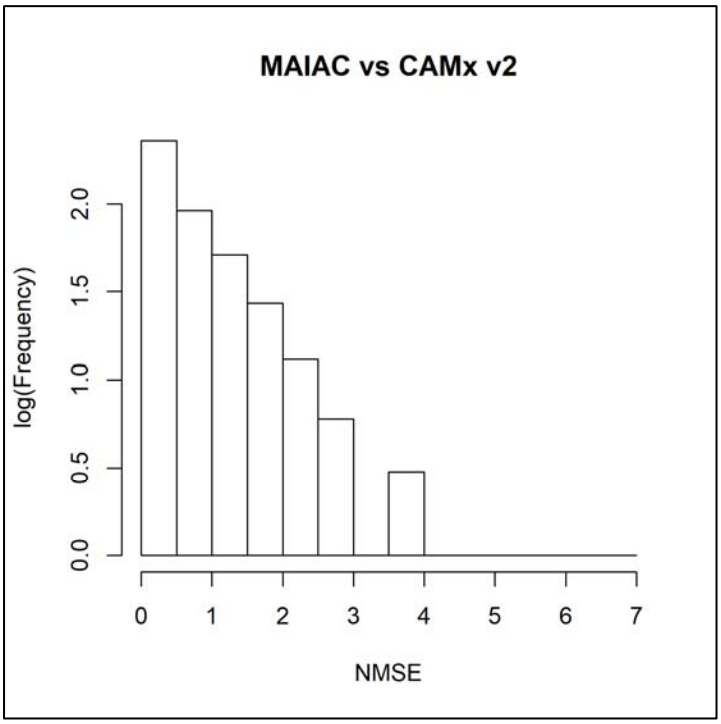

Figure 46. Domain-wide bugle plots of MAIAC vs CAMx v2.2 AOD values for 2012. The fractional bias bugle plot is shown on the left, while the fraction error bugle plot is shown on the right.

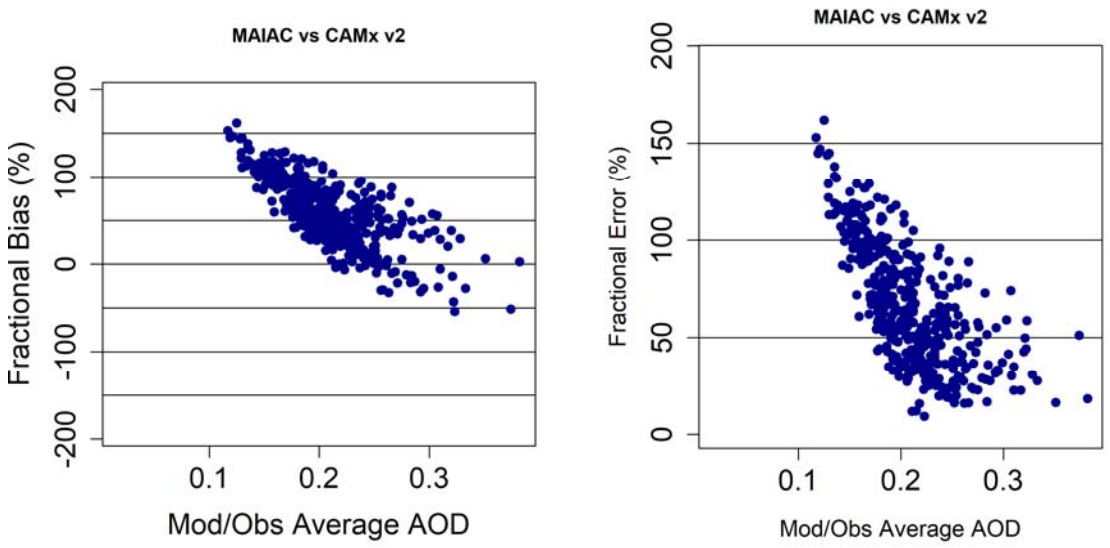

Figure 47. Domain-wide Q-Q plots of CAMx v2.2 (mean model AOD - left) and MAIAC (mean observational AOD - right) AOD values for 2012.

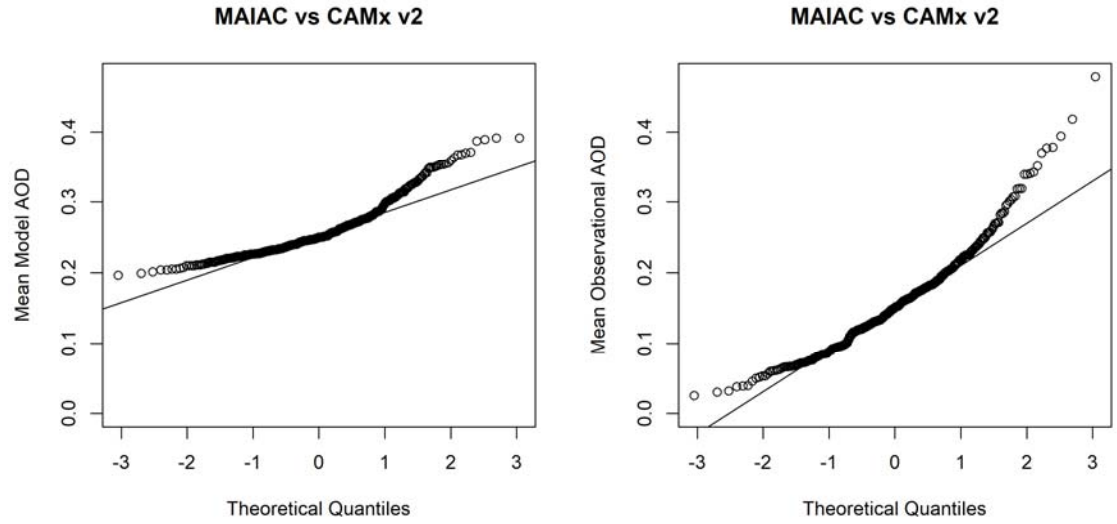

Figure 48. A domain-wide soccer plot of normalized mean error vs. normalized mean bias for MAIAC vs. CAMx v2.2 AOD data during 2012. Values are colored by the maximum CAMx v2.2 WF-only AOD value in the domain to assess the influence of wildfire smoke on bias and error between these two datasets.

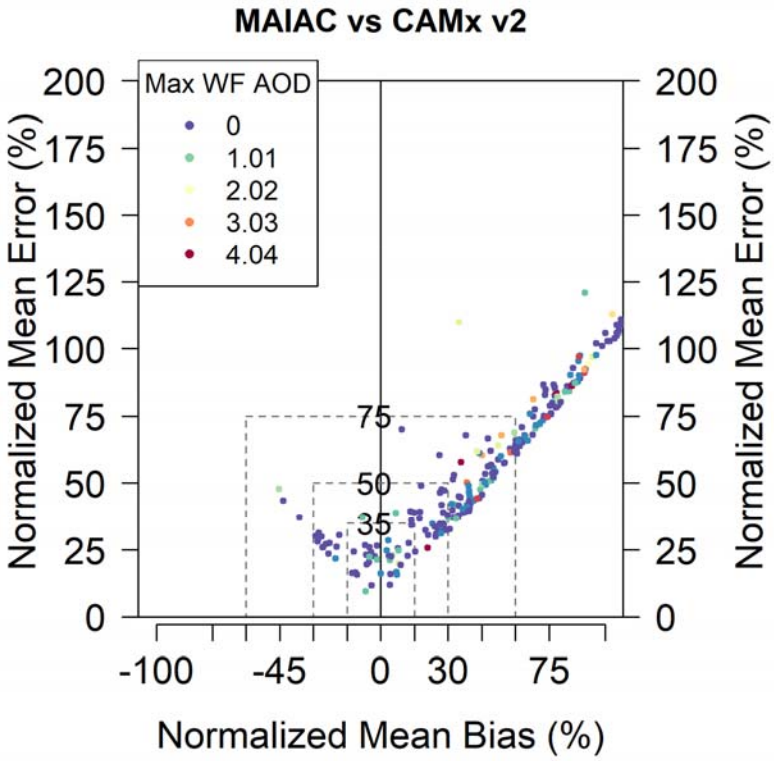

Figure 49. MAIAC vs. CAMx v2.2 monthly average cell-based FAC2 values for June 2012.

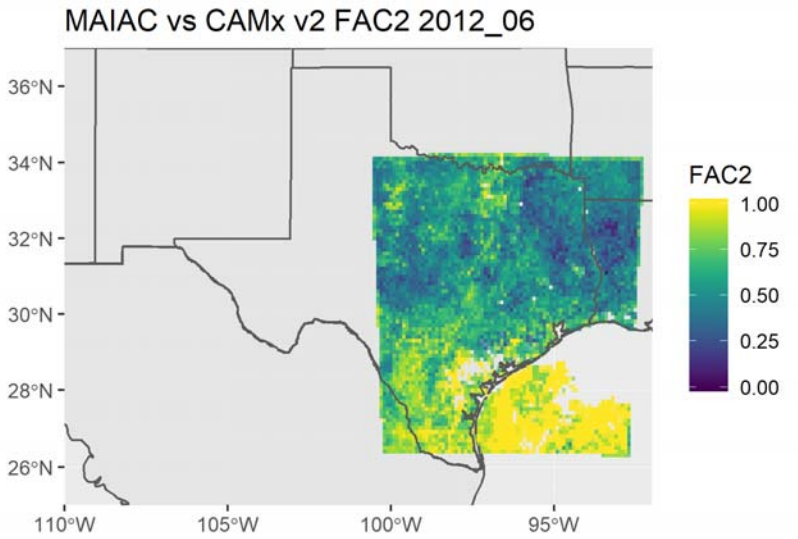

Figure 50. MAIAC vs. CAMx v2.2 monthly average cell-based R^2 values for June 2012.

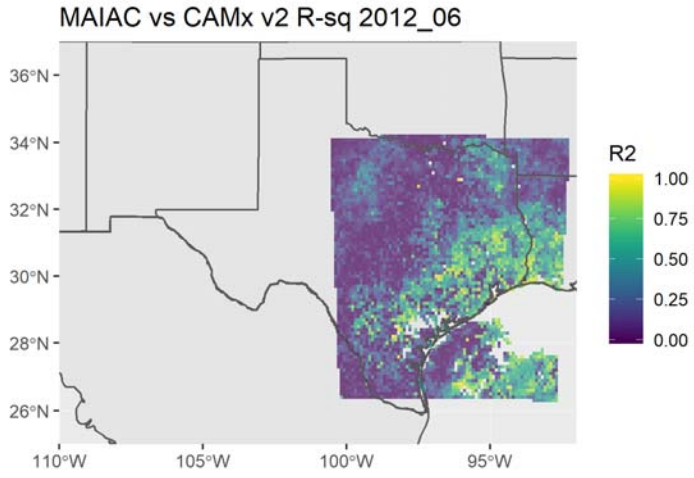

Figure 51. MAIAC (green) versus total CAMx v2.2 (red) and total CAMx v1.5 (blue) hourly domain-averaged AOD for 2012.

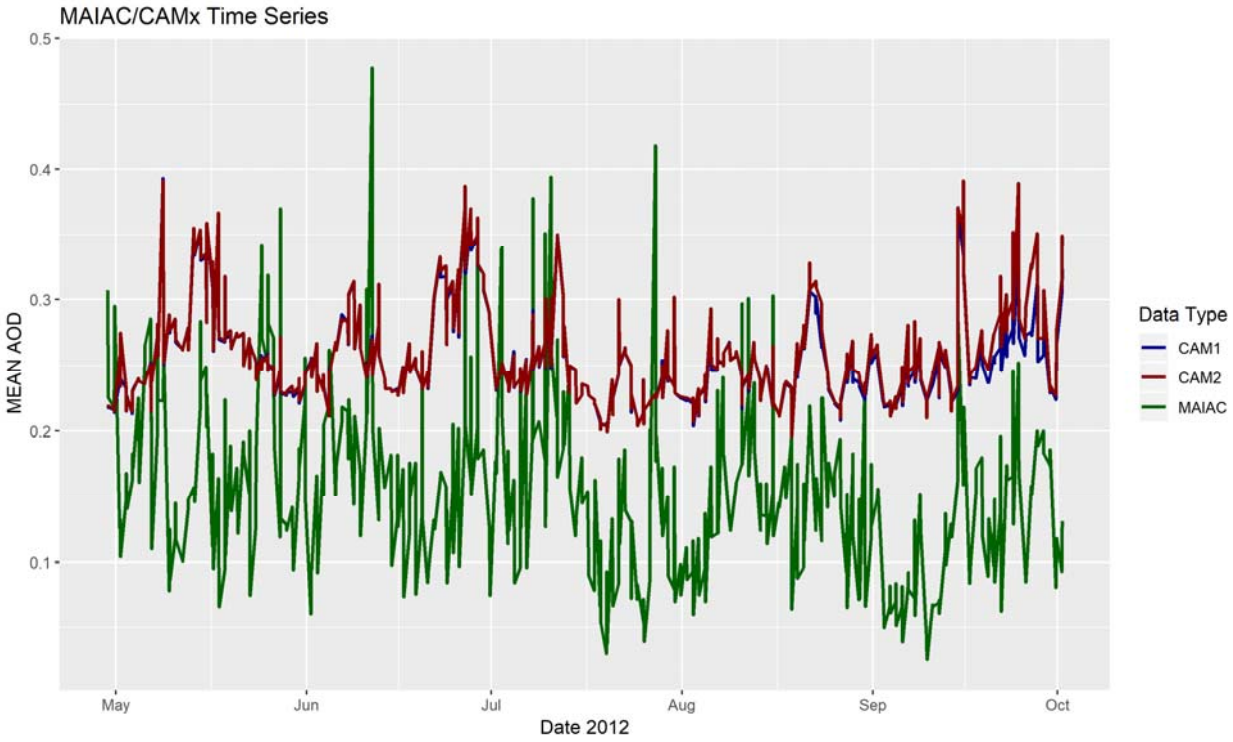

Figure 52. MAIAC observed AOD (bottom) vs. CAMx v2.2 (left, blue) and CAMx v1.5 (left, green) for all hourly 2012 values.

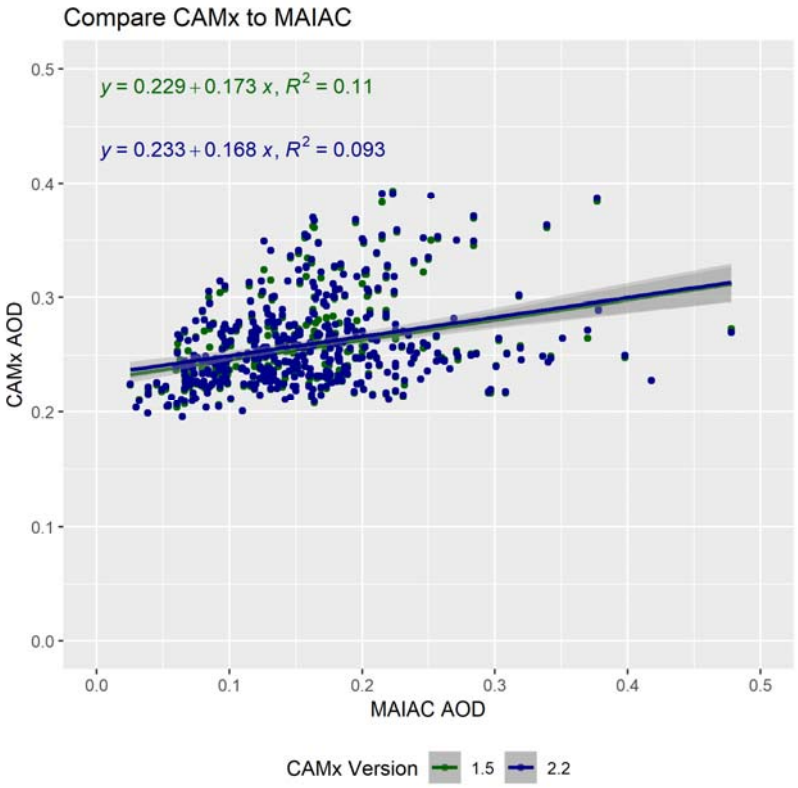

Figure 53. MAIAC observed AOD (bottom) vs. CAMx v2.2 (left, blue) and CAMx v1.5 (left, green) values for hourly WF-only events (filtered by CAMx WF-only 75th percentile) in 2012.

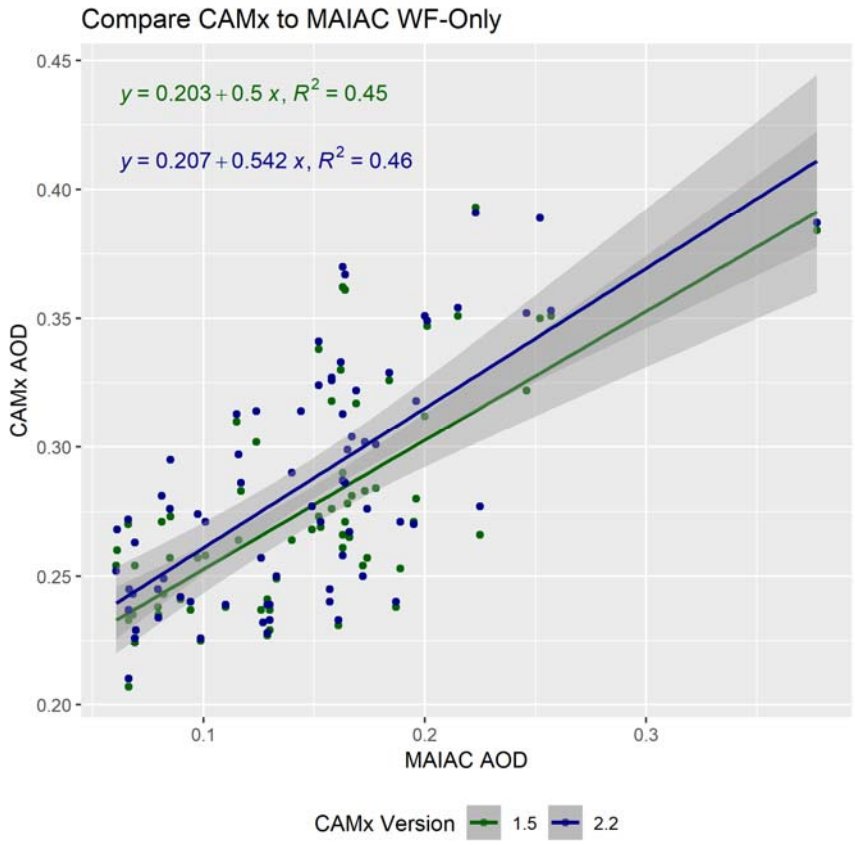

5.4 Case Studies

5.4.1 Case Study Selection

Case studies were chosen to aid in the assessment of the FINN v2.2 fire emissions inventory by comparing the modeled wildfire AOD from HYSPLIT, CAMx v1.5, and CAMx v2.2 with observed AOD from the MAIAC satellite product. Event time windows were chosen based on visible satellite imagery (MODIS Aqua and Terra) and the Hazard Mapping System (HMS) smoke and fire product. When fires were detected and smoke was visible in both of these products within the 4 km nested modeling grid shown in Figure 6, we were able to adequately compare MAIAC AOD with the HYSPLIT and FINN v2.2 or v1.5-derived model products. This assessment precludes many days where clouds or high wildfire smoke levels masked the MAIAC AOD signal, narrowing our possible case studies to days that were relatively cloud-free and/or regions surrounding the highest wildfire smoke locations. Additionally, the MAIAC product only provides observed AOD values once or twice per day. This further narrows our case study potential to hours when the MODIS polar orbiting satellites would take measurements over the 4 km nested area (approximately 15:00-19:00 UTC, or Z, which corresponds to 10:00-14:00 CST). Therefore, we have chosen case studies from dates and times that (1) are relatively unbiased from cloud influence, and (2) have an adequate amount of MAIAC data to compare with the modeled products.

Case studies for a week-long smoke episode from September 19-26, 2012, are provided in Figures 54-68 below. Additionally, a case study from June 27, 2012, is also characterized in Figures 69-71. We provide a side-by-side comparison for each event of hourly HYSPLIT, CAMx v2.2, and MAIAC AOD values. Additionally, we explore the differences in CAMx v2.2 and CAMx v1.5 versus MAIAC AOD values during each event to assess the performance of the FINN v2.2 fire emissions inventory compared with v1.5.

5.4.2 Week-Long Case Study for September 19-26, 2012

Figure 54 shows a side-by-side comparison of the first event (September 19, 2012) during the week-long case study of fires in Texas by illustrating HYSPLIT, CAMx v2.2 wildfire-only, and MAIAC AOD values during a satellite pass-over hour (in this case for 17:00 Z). For all subsequent figures, HYSPLIT data will be shown at a 50 km resolution, while CAMx and MAIAC data will be shown at a 4 km resolution consistent with the 4 km nested grid box in Figure 6. This comparison provides a good example of how well HYSPLIT, CAMx v2.2 wildfire-only, and MAIAC AOD values compare spatially during a wildfire event. Fire plumes are more visible in the CAMx v2.2 wildfire-only results, but the overall pattern of AOD is reflected in both the modeled (HYSPLIT) and observed (MAIAC) views. In this case, we see a general pattern of high AOD in north-central Texas (near the fires) and lower AOD in western Louisiana. In order to assess the performance of CAMx v2.2 versus CAMx v1.5, we plotted the wildfire-only values from each model versus the MAIAC observed data in Figure 55. CAMx wildfire-only data points provide a good estimation of where and how severely wildfire smoke might be affecting an area. Since the MAIAC AOD values are a total column aggregate of AOD (i.e., including dust, anthropogenic particulate matter, biogenic SOA, wildfire smoke, etc.) we filter out CAMx and MAIAC co-located points that value CAMx wildfire-only AODs below a background threshold (what we assume to be non-fire affected points). This threshold changes slightly from fire to fire depending on the intensity, but range from 0.05 to 0.2 throughout all cases shown in this section. We also subset the AOD comparison by the areas most affected by wildfire smoke influence. For this case, we subset the AOD data for an area around the fires at 95° to 100° W Longitude, and 30° to 34° N Latitude. Both the background AOD cutoff and subset area values are provided in the figure captions for each subsequent case. In this case (Figure 55), we see that CAMx v2.2 values are better correlated (R^2=0.35 vs. R^2=0.17) and provide a closer representation (slope closer to 1.0) of the MAIAC observed values during this wildfire event.

Figure 56 shows the second event from the week-long case study; September 20, 2012, at 19:00 Z. In this case, we see fires in Southeastern Texas and Western Louisiana. These fires are clearly visible in the CAMx v2.2 wildfire-only data and slightly less so in the HYSPLIT data. In the MAIAC data, the fires are shown as smaller areas of higher AOD values when compared with the CAMx figure, but are still visible. We also see slightly higher values of MAIAC AOD over North-Central Texas. These are corroborated in the HYSPLIT and CAMx v2.2 figures (note that the CAMx v2.2 values are similar to the MAIAC values, even though the color scales diverge due to very high CAMx wildfire AOD values in Louisiana). These high fire-related AOD values coming from the north-northwest are from large wildfires in the Northwest U.S. Additionally, we investigate total CAMx v2.2 and v1.5 AOD in Figure 57. Here, CAMx v2.2 again provides a slightly better correlation (R^2=0.15 vs. R^2=0.12) and closer representation to the observed MAIAC values. Looking at the wildfire-only CAMx values in Figure 58, we see a much higher

correlation with MAIAC AOD values in the CAMx v2.2 (R^2=0.38) versus v1.5 (R^2=0.005), and a positive slope in the CAMx v2.2 results compared to a negative slope in the v1.5 values.

Figure 59 shows the third event on September 21, 2012, at 18:00 Z. Fires in this case are mostly in Western Louisiana and Eastern Texas. HYSPLIT, CAMx wildfire-only, and MAIAC AOD values all show a sweeping west-southwest to east-northeastern pattern of higher AOD values. Within the area near the fires (shown in Figure 60), neither model shows much association with the MAIAC-observed AOD values; however, the CAMx v2.2 wildfire-only values show some correlation (R^2=0.10) with the observations, whereas the CAMx v1.5 values show no correlation.

Figure 61 shows the fourth event on September 22, 2012, at 18:00 Z. On this day, there are significant impacts on AOD values in Texas from wildfires in the Northwest U.S., and a smaller fire at the Oklahoma/Arkansas border. It is important to note that the CAMx wildfire-only values are similar to the observed MAIAC AOD values, even though the color scale diverge between these two plots. The HYSPLIT plot also shows a sweeping northerly and westerly flow of higher AOD values in addition to a hotspot near the Oklahoma/Arkansas border. For the CAMx/MAIAC comparison in Figure 62, although there are less direct comparison points between the CAMx/MAIAC data (especially for the fire near the Oklahoma/Arkansas border), we still see a slightly better correlation between the CAMx v2.2 wildfire-only AOD values (R^2=0.13) than the CAMx v1.5 values (R^2=0.048). It is important to note that the CAMx v2.2 does overestimate the AOD values by a factor of three compared to the CAMx v1.5. This is consistent with overall higher CAMx values reported in version 2.2 versus 1.5 mentioned in Section 5.3.

Figure 63 shows the fifth event on September 23, 2012, at 18:00 Z. Although there is much less MAIAC data available for this time period, we are still able to compare values for the fires in Western Louisiana that are visible in the HYSPLIT, CAMx, and MAIAC plots. Comparing the CAMx v2.2 and v1.5 values in Figure 64, we see a similar correlation with MAIAC AOD values between v2.2 (R^2=0.12) and v1.5 (R^2=0.17), but a closer representation of MAIAC values (slope closer to 1) in v2.2.

Figure 65 shows the sixth event on September 24, 2012, at 17:00 Z. Fires are predominately in Eastern Texas and Western Louisiana. In all three plots, we see higher AOD values near the fires and lower AOD values further west. In the CAMx comparison with MAIAC in Figure 66, we again see a better correlation with MAIAC data from v2.2 (R^2=0.15 vs. R^2=0.008), but an overestimation in the absolute AOD value.

Figure 67 shows the seventh event on September 26, 2012, at 19:00 Z. This case is primarily effected by a large fire in Western Louisiana. We see consistent, qualitative AOD structure from the models and the observed plots. When we focus in on the fire influenced area in Figure 68 and compare CAMx v2.2 and v1.5, we see that while the correlations between model and observed AOD are similar for each version (R^2=0.12 in v2.2 and R^2=0.18 in v1.5), the CAMx v1.5 gets closer to the observed values, while CAMx v2.2 overestimates. For the week-long case study, we suggest that while CAMx v2.2 AOD values correlate better with observed values overall and on most days than CAMx v1.5 AOD, in some cases, CAMx v1.5 performs better and has less overestimation (as previously stated in Section 5.3).

5.4.3 June 27, 2012 Case Study

Our final case study for June 27, 2012, is shown in Figure 69 shows another instance of fires in Eastern Texas. All three plots show a similar AOD spatial pattern, with higher values in the east due to the fire. In Figure 70, the total CAMx AOD from v1.5 and v2.2 are compared with MAIAC observed AOD. While correlations and absolute value of AOD between v1.5 and v2.2 are similar (e.g., R^2=0.43 in v1.5 and R^2=0.41 in v2.2), we see a slightly better slope (16% higher) in the v2.2 values versus the v1.5 values. This suggests that we are seeing a slightly better estimate of observed values in v2.2. In Figure 71, we can also compare wildfire-only CAMx values to MAIAC observed AOD. Although there are very few points that are associated with this event and the correlation are strongly influenced by a few high data points, we still see a better correlation and slope from v2.2 despite some overestimation associated with the latter CAMx version.

5.4.4 Case Study Summary

Overall, the case studies show that HYSPLIT and CAMx are able to qualitatively reproduce areas of high AOD caused by fires when compared with the observed values from MAIAC. Additionally, it appears that CAMx v2.2 wildfire-only AODs correlate better with the observed MAIAC AOD values than CAMx v1.5. We do see some cases of over estimation of AOD in CAMx v2.2 compared with v1.5.

Figure 54. HYSPLIT (left), CAMx v2.2 wildfire-only (middle), and MAIAC (right) AOD values for September 19, 2012 at 17:00 Z. HYSPLIT data is at 50 km resolution, while CAMx and MAIAC data is at 4 km resolution. Light grey area indicates areas outside of the boundaries of MAIAC/CAMx data. Dark grey indicates areas with no AOD values within the HYSPLIT, CAMx, and MAIAC boundaries. Note the difference in AOD scaling for each figure.

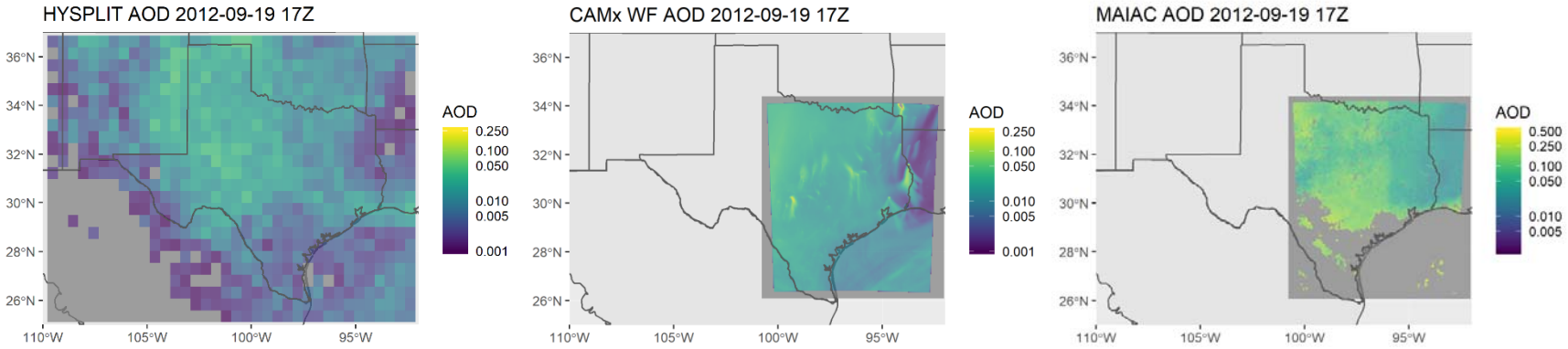

Figure 55. CAMx v2.2 wildfire-only AOD values (shown in blue) and CAMx v1.5 wildfire-only AOD values (shown in green) plotted versus MAIAC observed AOD on September 19, 2012, at 17:00 Z. The background cut-off for CAMx is 0.05. The subset area is 95°-100° W Longitude and 30°-34° N Latitude. Linear regression equations and R^2 values for each comparison are shown at the top of the figure in the respective model color.

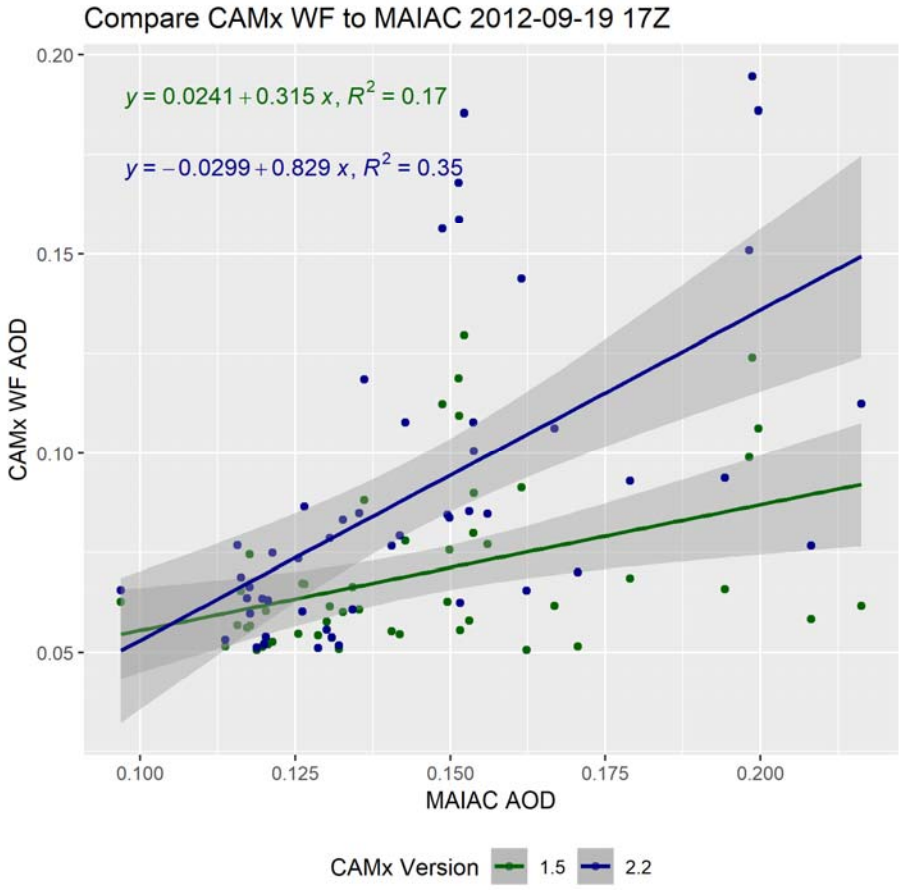

Figure 56. HYSPLIT (left), CAMx v2.2 wildfire-only (middle), and MAIAC (right) AOD values for September 20, 2012, at 19:00 Z. HYSPLIT data is at 50 km resolution, while CAMx and MAIAC data is at 4 km resolution. Light grey indicates areas outside of the boundaries of MAIAC/CAMx data. Dark grey indicates areas with no AOD values within the HYSPLIT, CAMx, and MAIAC boundaries. Note the difference in AOD scaling for each figure.

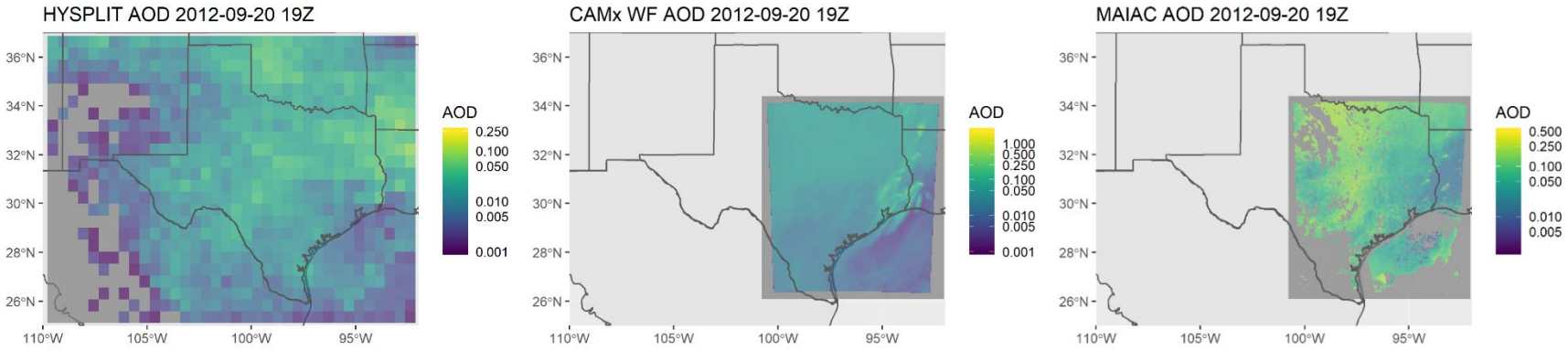

Figure 57. CAMx v2.2 AOD values (shown in blue) and CAMx v1.5 wildfire-only AOD values (shown in green) versus MAIAC observed AOD on September 20, 2012, at 19:00 Z. Linear regression equations and R^2 values for each comparison are shown at the top of the figure in the respective model color.

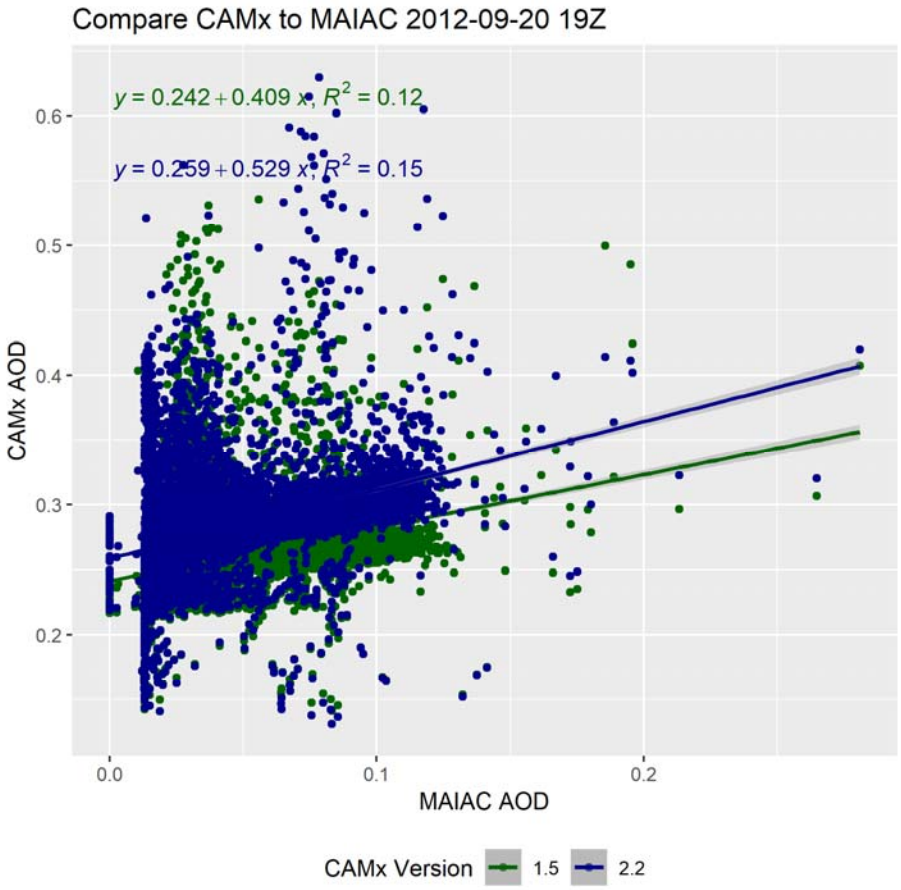

Figure 58. CAMx v2.2 wildfire-only AOD values (shown in blue) and CAMx v1.5 wildfire-only AOD values (shown in green) are plotted versus MAIAC observed AOD on September 20, 2012, at 19:00 Z. The background cut-off for CAMx is 0.1. The subset area is 90°-95° W Longitude and 29°-34° N Latitude. Linear regression equations and R^2 values for each comparison are shown at the top of the figure in the respective model color.

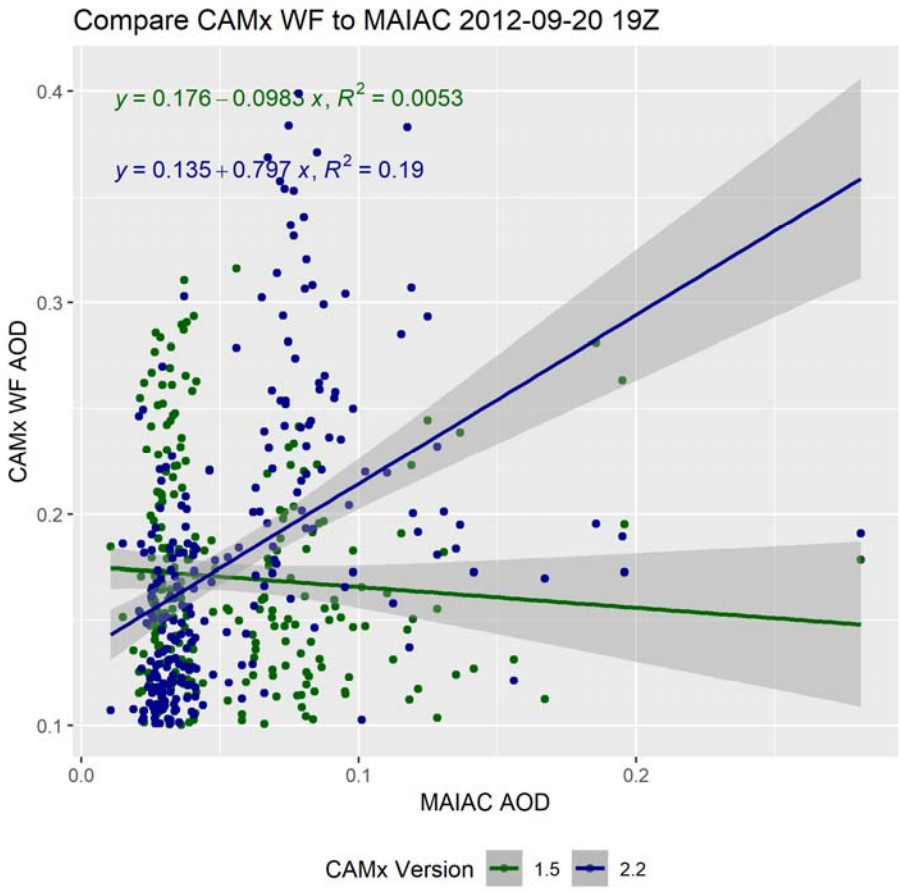

Figure 59. HYSPLIT (left), CAMx v2.2 wildfire-only (middle), and MAIAC (right) AOD values are shown for September 21, 2012, at 18:00 Z. HYSPLIT data is at 50 km resolution, while CAMx and MAIAC data is at 4 km resolution. Light grey area indicates area outside of the boundaries of MAIAC/CAMx data. Dark grey indicates areas with no AOD values within the HYSPLIT, CAMx, and MAIAC boundaries. Note the difference in AOD scaling for each figure.

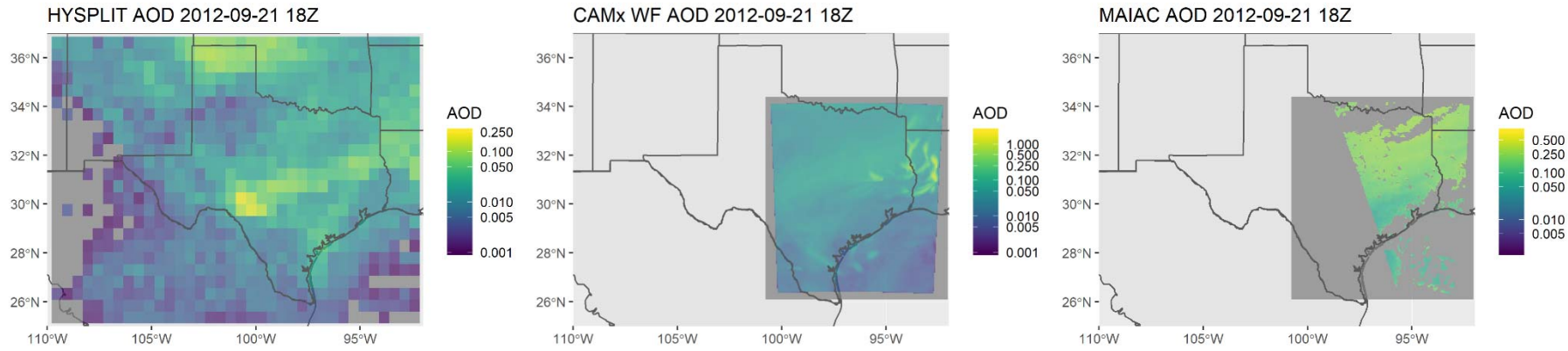

Figure 60. CAMx v2.2 wildfire-only AOD values (shown in blue) and CAMx v1.5 wildfire-only AOD values (shown in green) are plotted vs. MAIAC observed AOD on September 21, 2012, at 18:00 Z. The background cut-off for CAMx is 0.2. The subset area is 90°-100° W Longitude and 29°-34° N Latitude. Linear regression equations and R^2 values for each comparison are shown at the top of the figure in the respective model color.

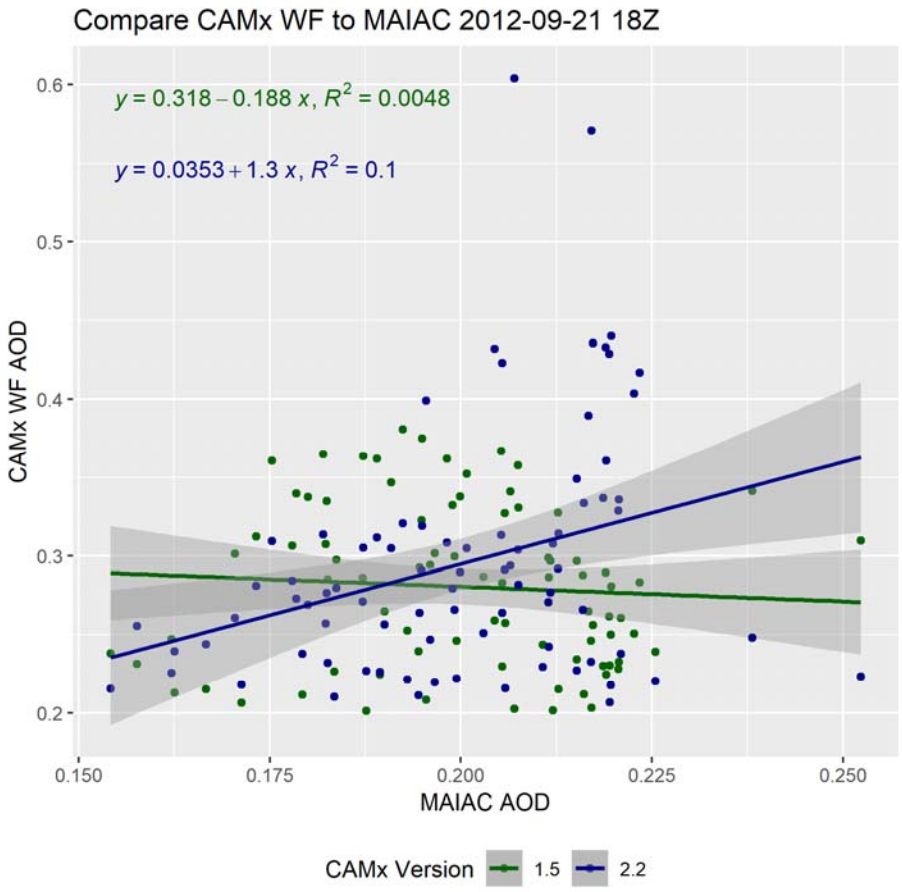

Figure 61. HYSPLIT (left), CAMx v2.2 wildfire-only (middle), and MAIAC (right) AOD values are shown for September 22, 2012, at 18:00 Z. HYSPLIT data is at 50 km resolution, while CAMx and MAIAC data is at 4 km resolution. Light grey area indicates area outside of the boundaries of MAIAC/CAMx data. Dark grey indicates areas with no AOD values within the HYSPLIT, CAMx, and MAIAC boundaries. Note the difference in AOD scaling for each figure.

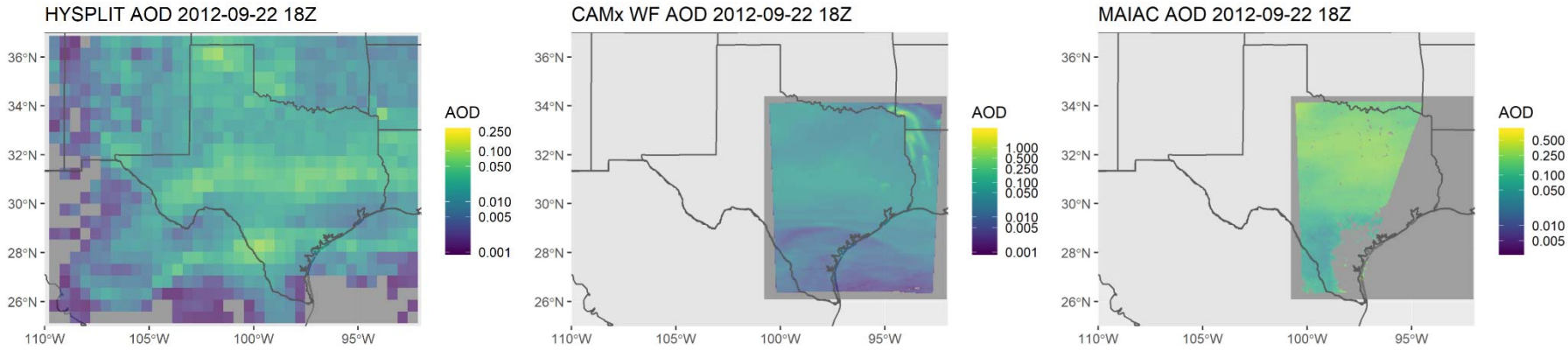

Figure 62. CAMx v2.2 wildfire-only AOD values (shown in blue) and CAMx v1.5 wildfire-only AOD values (shown in green) are plotted vs. MAIAC observed AOD on September 22, 2012, at 18:00 Z. The background cut-off for CAMx is 0.2. The subset area is 92°-101° W Longitude and 29°-34° N Latitude. Linear regression equations and R^2 values for each comparison are shown at the top of the figure in the respective model color.

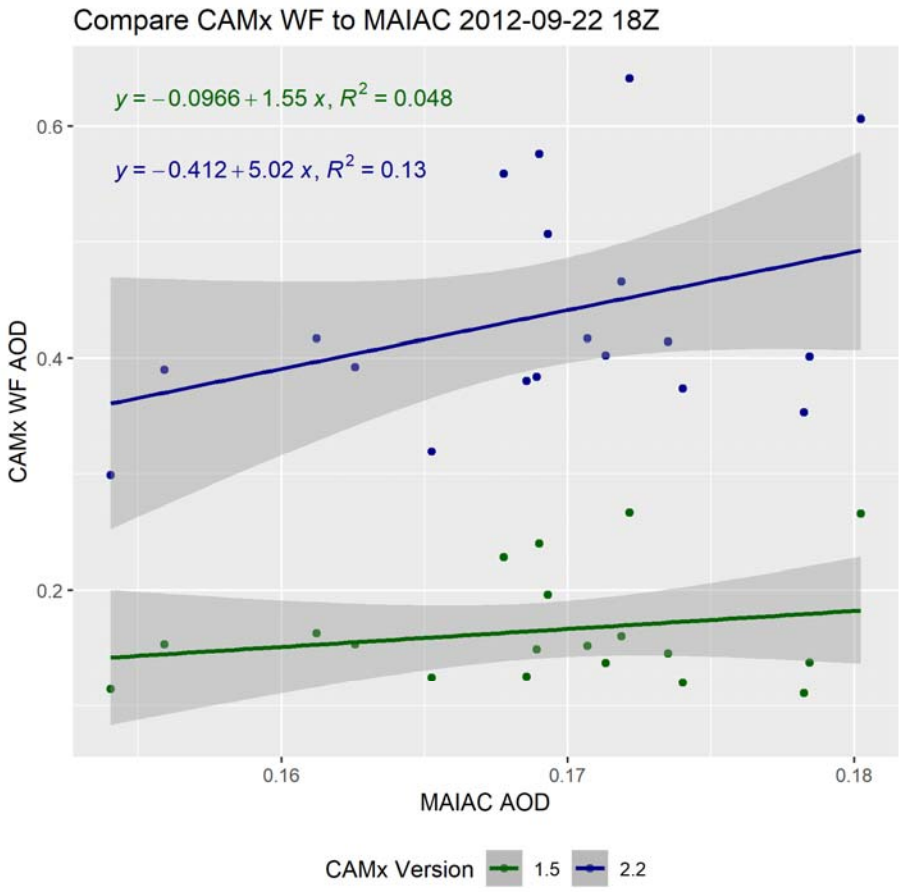

Figure 63. HYSPLIT (left), CAMx v2.2 wildfire-only (middle), and MAIAC (right) AOD values are shown for September 23, 2012, at 18:00 Z. HYSPLIT data is at 50 km resolution, while CAMx and MAIAC data is at 4 km resolution. Light grey area indicates area outside of the boundaries of MAIAC/CAMx data. Dark grey indicates areas with no AOD values within the HYSPLIT, CAMx, and MAIAC boundaries. Note the difference in AOD scaling for each figure.

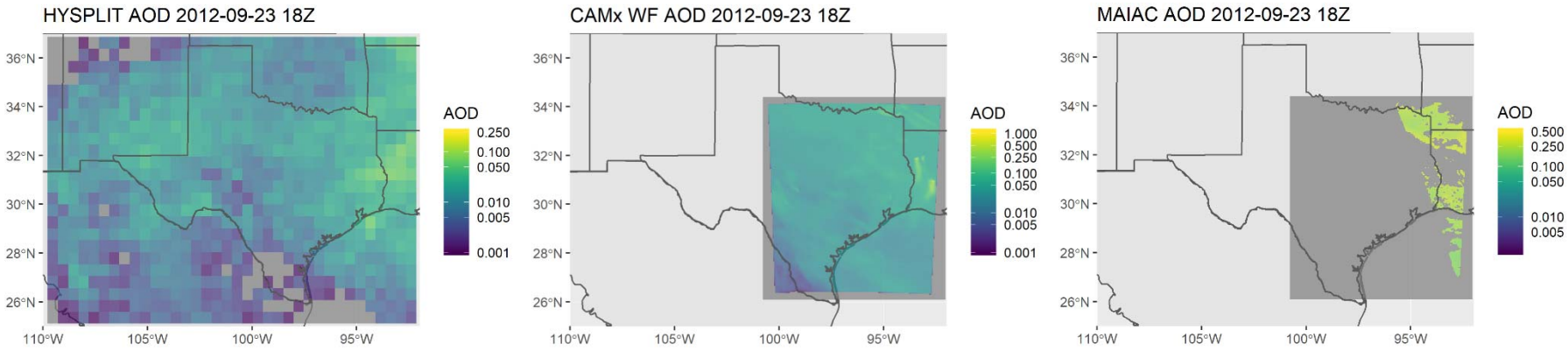

Figure 64. CAMx v2.2 wildfire-only AOD values (shown in blue) and CAMx v1.5 wildfire-only AOD values (shown in green) are plotted versus MAIAC observed AOD on September 23, 2012, at 18:00 Z. The background cut-off for CAMx is 0.05. The subset area is 90°-96° W Longitude and 29°-33° N Latitude. Linear regression equations and R^2 values for each comparison are shown at the top of the figure in the respective model color.

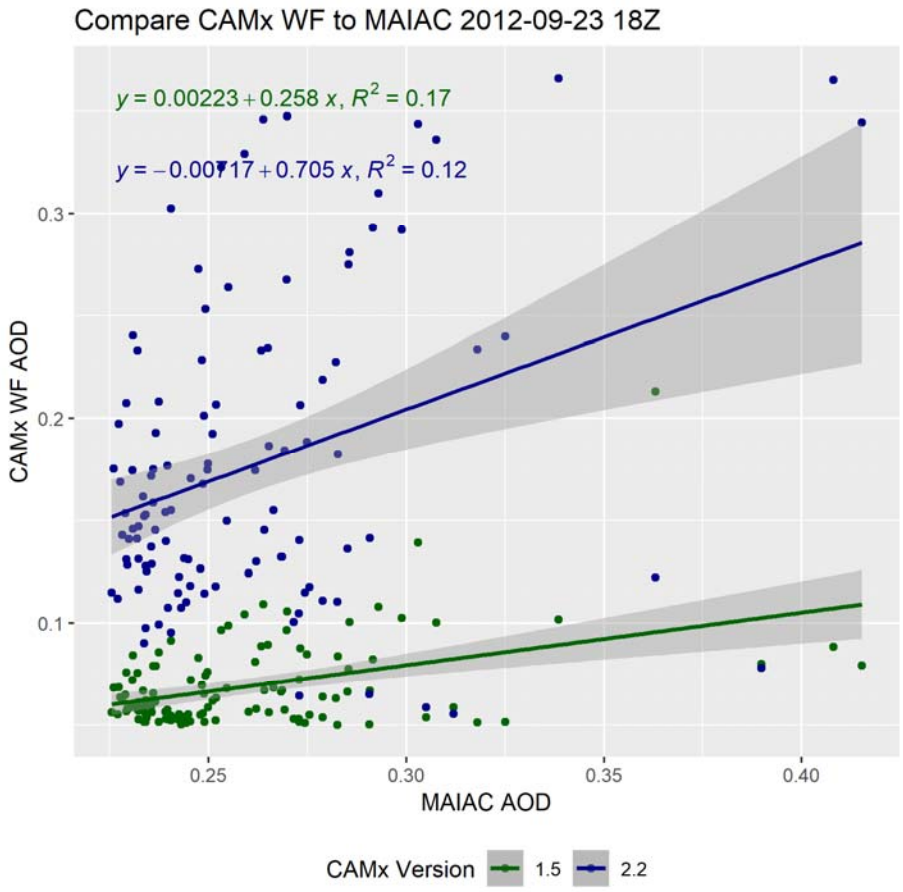

Figure 65. HYSPLIT (left), CAMx v2.2 wildfire-only (middle), and MAIAC (right) AOD values are shown for September 24, 2012, at 17:00 Z. HYSPLIT data is at 50 km resolution, while CAMx and MAIAC data is at 4 km resolution. Light grey area indicates area outside of the boundaries of MAIAC/CAMx data. Dark grey indicates areas with no AOD values within the HYSPLIT, CAMx, and MAIAC boundaries. Note the difference in AOD scaling for each figure.

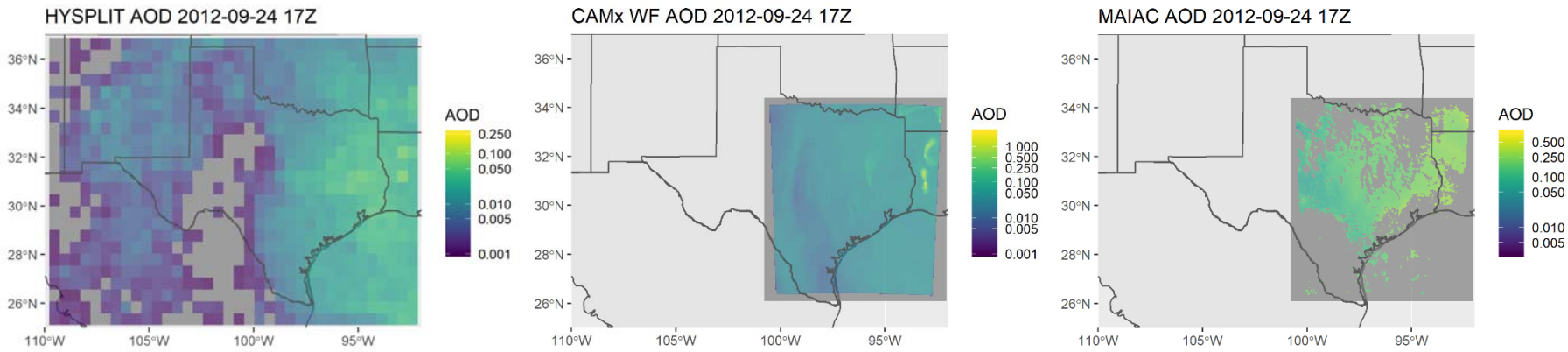

Figure 66. CAMx v2.2 wildfire-only AOD values (shown in blue) and CAMx v1.5 wildfire-only AOD values (shown in green) are plotted vs. MAIAC observed AOD on September 24, 2012, at 17:00 Z. The background cut-off for CAMx is 0.1. The subset area is 90°-94° W Longitude and 30°-33° N Latitude. Linear regression equations and R^2 values for each comparison are shown at the top of the figure in the respective model color.

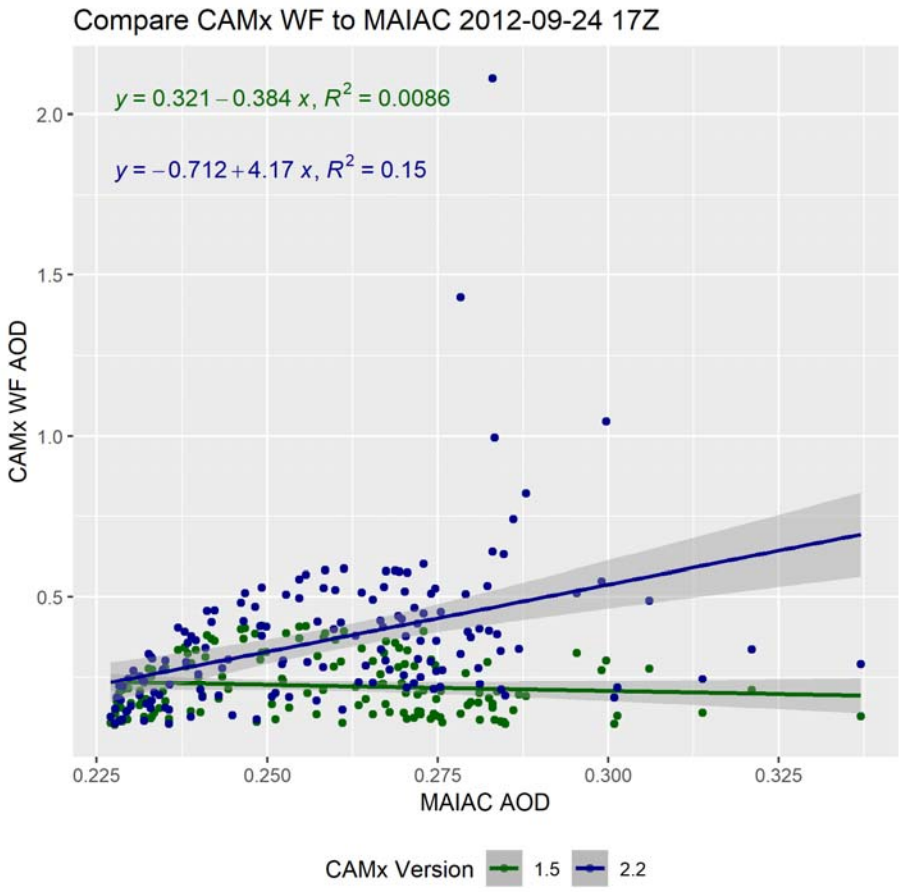

Figure 67. HYSPLIT (left), CAMx v2.2 wildfire-only (middle), and MAIAC (right) AOD values are shown for September 26, 2012, at 19:00 Z. HYSPLIT data is at 50 km resolution, while CAMx and MAIAC data is at 4 km resolution. Light grey area indicates area outside of the boundaries of MAIAC/CAMx data. Dark grey indicates areas with no AOD values within the HYSPLIT, CAMx, and MAIAC boundaries. Note the difference in AOD scaling for each figure.

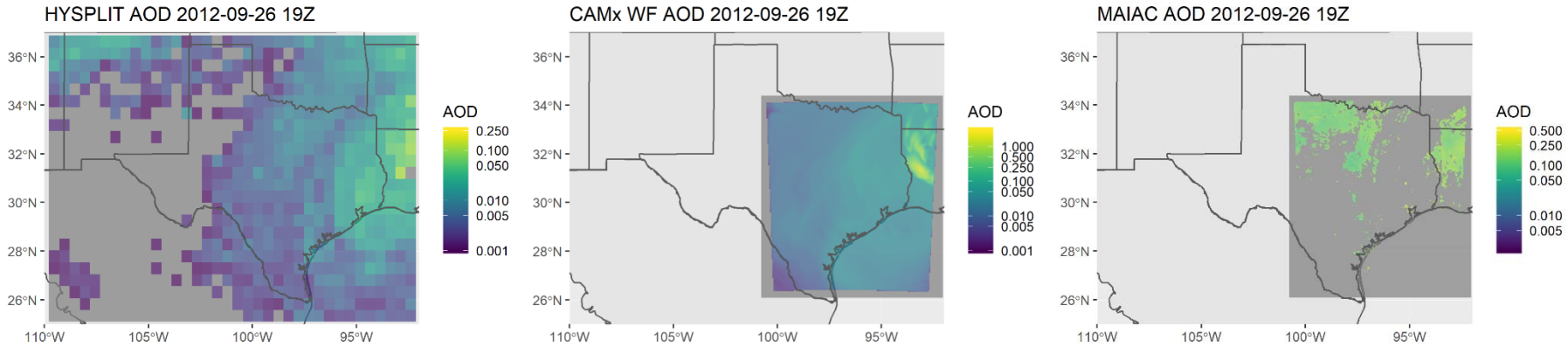

Figure 68. CAMx v2.2 wildfire-only AOD values (shown in blue) and CAMx v1.5 wildfire-only AOD values (shown in green) are plotted vs. MAIAC observed AOD on September 26, 2012 at 19:00 Z. The background cut-off for CAMx is 0.05. The subset area is 90°-93° W Longitude and 30°-33° N Latitude. Linear regression equations and R^2 values for each comparison are shown at the top of the figure in the respective model color.

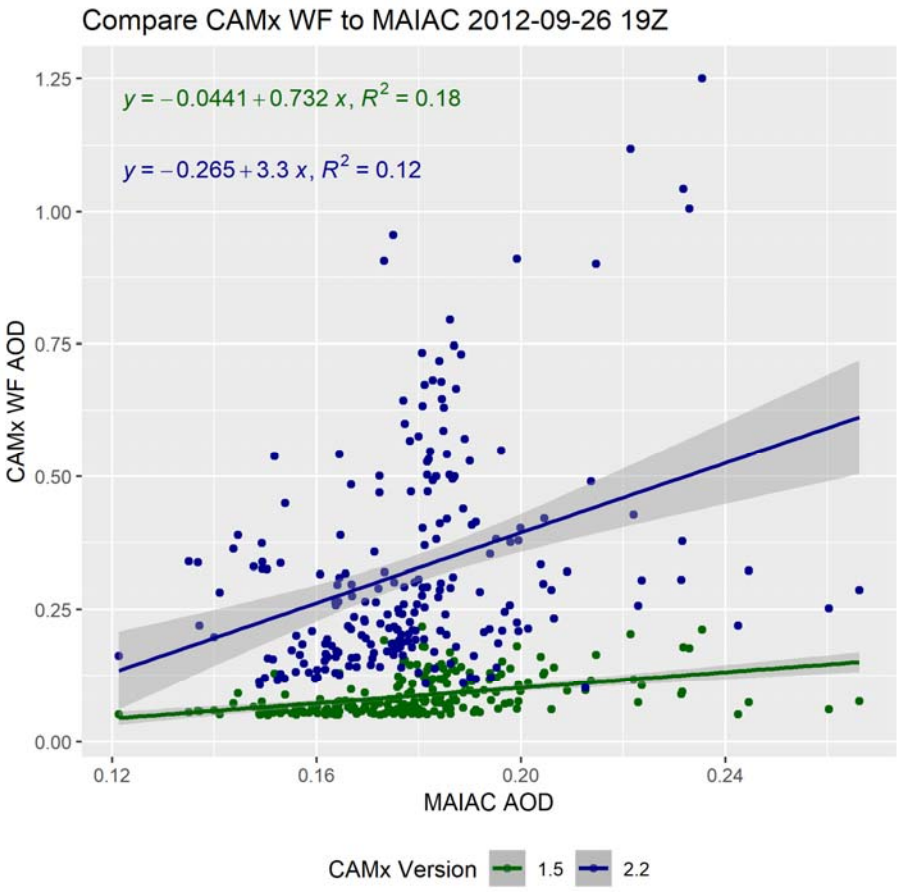

Figure 69. HYSPLIT (left), CAMx v2.2 wildfire-only (middle), and MAIAC (right) AOD values are shown for June 27, 2012, at 17:00 Z. HYSPLIT data is at 50 km resolution, while CAMx and MAIAC data is at 4 km resolution. Light grey area indicates area outside of the boundaries of MAIAC/CAMx data. Dark grey indicates areas with no AOD values within the HYSPLIT, CAMx, and MAIAC boundaries. Note the difference in AOD scaling for each figure.

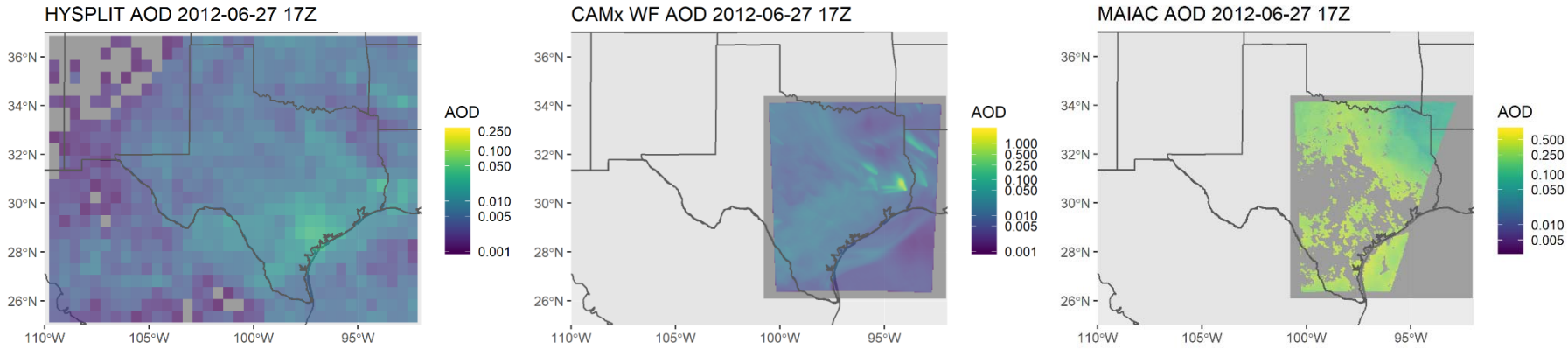

Figure 70. CAMx v2.2 AOD values (shown in blue) and CAMx v1.5 wildfire-only AOD values (shown in green) are plotted vs. MAIAC observed AOD on June 27, 2012, at 17:00 Z. Linear regression equations and R^2 values for each comparison are shown at the top of the figure in the respective model color.

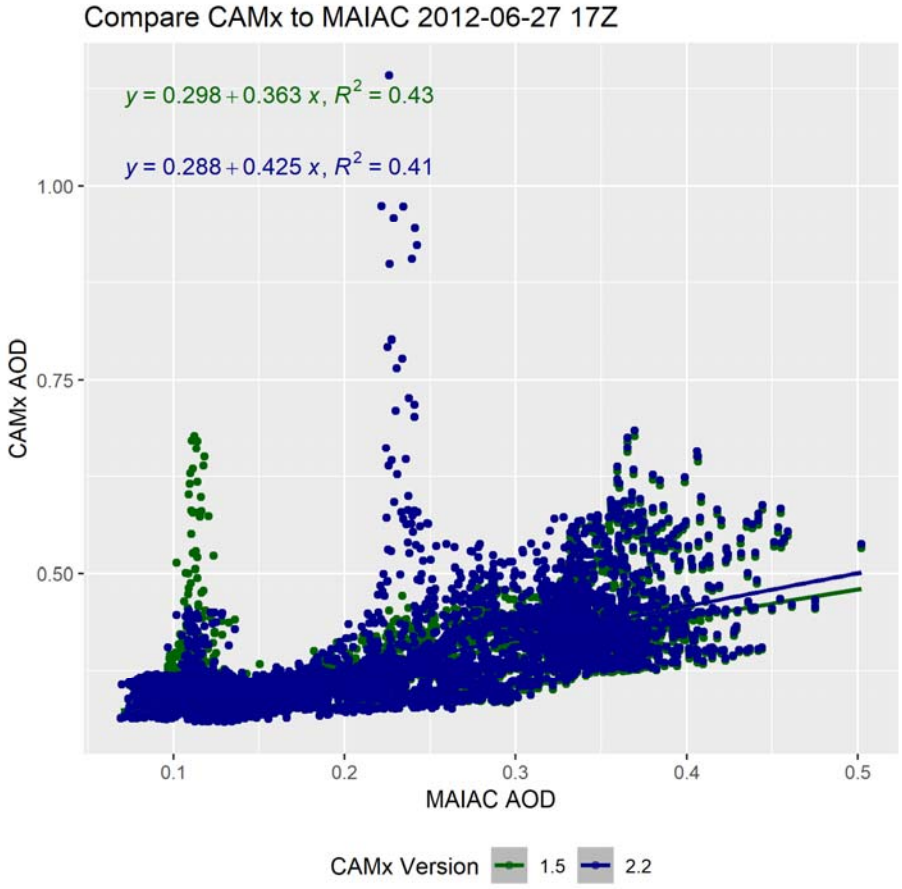

Figure 71. CAMx v2.2 wildfire-only AOD values (shown in blue) and CAMx v1.5 wildfire-only AOD values (shown in green) are plotted vs. MAIAC observed AOD on June 27, 2012, at 17:00 Z. The background cut-off for CAMx is 0.1. The subset area is 91°-97° W Longitude and 30°-33° N Latitude. Linear regression equations and R^2 values for each comparison are shown at the top of the figure in the respective model color.

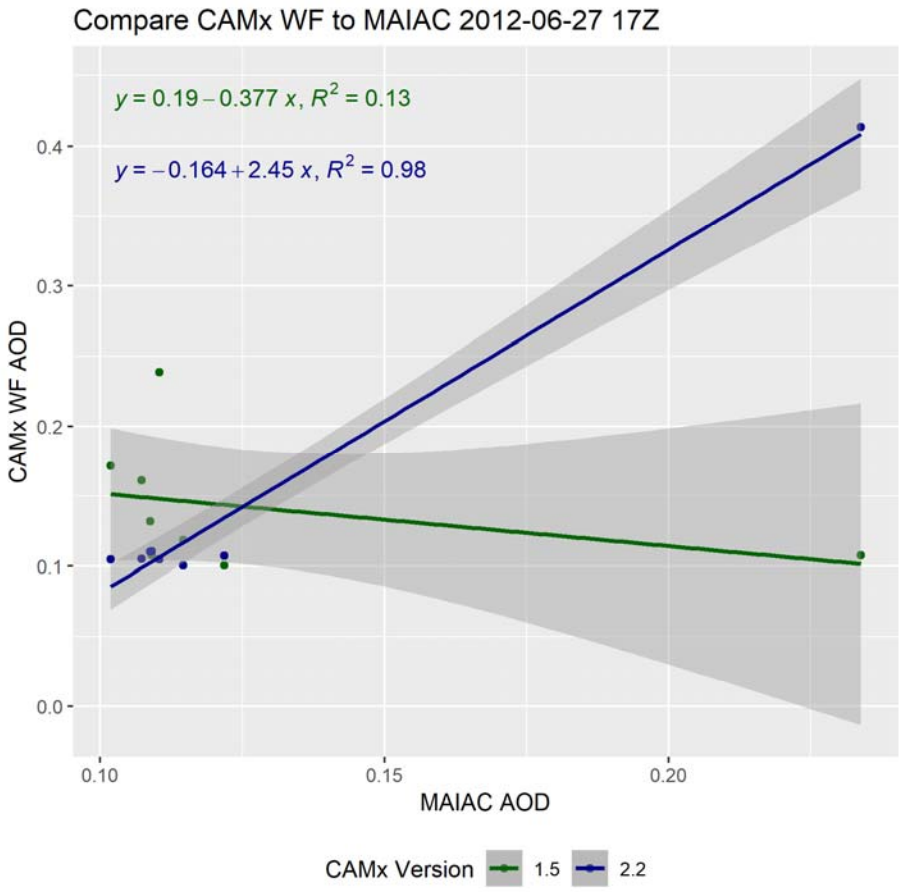

6. Audits of Data Quality

6.1 Model Development

Quality assurance was addressed throughout the project including FINN algorithm development, data processing, and analysis activities. As part of AQRP Project 14-011 (McDonald-Buller et al., 2015), a thorough independent review of all lines of the FINN source code was conducted by Dr. Yosuke Kimura at the University of Texas at Austin. The FINN v.2.2 application for this project was developed as an outcome of AQRP Project 14-011 and TCEQ feedback.

The FINNv2.2 geographic preprocessor was written in Structured Query Language (SQL) and Python3 by Dr. Yosuke Kimura. McDonald-Buller et al. (2015) described in detail the data quality assurance processes for burned area estimates and geometries and comparisons of vector and raster intersection methods for identifying underlying land cover in burned areas. The preprocessor code was originally written in a Linux environment and ported into the Docker environment. Porting to the Docker environment was accomplished by Mr. Max Joseph at University of Colorado, Boulder. These two project personnel independently worked on their assignments, and quality assured each other's work by reviewing the code and applying sample input data. Dr. Christine Wiedinmyer conducted testing by running the code and evaluating the results with the sample inputs. The open source code and instructions for its installation and use are accessible at https://github.com/yosukefk/finn_preproc.

In project AQRP 14-011, the algorithm that formed the basis of the FINN preprocessor was implemented in ArcPy in the ArcGIS workstation environment. The code had scaling issues that prohibited wide application of the model. Implementing it in the PostGIS environment resolved this issue. Execution wall clock times for the applications of FINNv2.2 with MODIS and VIIRS active fire detections for North America and at a global scale are shown in Table 14.

Table 14. Execution wall clock time (hours) by geographic extent and model year (with active fire feature count).

Geographic Extent	Model Year	Input AF Feature Count	Wall Clock Time (hours)	Processing Speed (feature/sec)
North America	2012	1643598	1.1	421
North America	2013	1922007	1.4	377
North America	2014	1859737	1.5	341
North America	2015	1827237	1.5	335
North America	2016	1606230	0.9	478
North America	2017	2153236	1.5	403
Global	2016	24805366	13.1	524
Global	2818	23399746	12.6	515

The FINNv2.2 emissions and chemical speciation codes used in this work were written in Interactive Data Language (IDL) by Dr. Wiedinmyer. The code was applied in its original form and its implementation was quality assured by Dr. Kimura.

Input data used in the study, including active fire detections, land cover, and biomass loading products were obtained from and quality assured by their independent official sources as described in Section 2. The sources and versions of the data products are documented in Section 2. They were visually inspected by QGIS mapping and evaluated for agreement with the original source as well as for reasonableness. Emission factors were taken from the peer-reviewed literature.

FINN emission estimates were rigorously quality assured by summarizing emissions of NOx, NMOC, CO, $PM_{2.5}$ by geographic region and land cover (by both the MODIS and FINN generic land cover types). Selected events that were associated with high concentration estimates based on CAMx and HYSPLIT simulations were revisited for quality assurance. In addition to the systematic quality assurance activities described above, the inventory was examined using GIS systems throughout the course of the project.

The FINN emissions output for 2012 was processed with EPS3 fire emission-specific pre-processors developed as a part of AQRP 14-011 project. The entire code was evaluated carefully; updates were made for the new mapping of the MOZART-T1 mechanism. Special attention was paid to the vertical placement of fires and the assigned plume rise values (bottom and top values) for adequacy.

Extensive QA was performed on the HYSPLIT model output and MAIAC satellite observations by an analyst at Sonoma Technology who was unassociated with the project. In each data set for which QA was performed, the number of files examined was at minimum 10% of the total data set. Additionally, the files used in QA were chosen at random from each data set.

6.2 HYSPLIT Model AOD Data Quality Audit

To validate fire locations and smoke patterns, HYSPLIT model outputs were compared to MODIS Terra Aerosol and Aqua Aerosol satellite images and/or to Hazard Mapping System (HMS) fire maps as observed on the AirNow-Tech website. 148 data files (equivalent to >10% of total HYSPLIT data), corresponding to 148 days, were assessed during QA. Hourly $PM_{2.5}$ data at 50 m height were investigated for all files. For 67 files either $PM_{2.5}$ at 500 m or 10,000 m was additionally assessed. QA analysis resulted in 6.1% (9 days) of files flagged as questionable for reasons including: (1) inconsistencies between fires marked on HMS fire maps and smoke observed in HYSPLIT output, and (2) smoke lingering over oceans in HYSPLIT output longer than expected. The remaining 94% of data examined during the QA screening were deemed consistent with the compared data sets.

144 HYSPLIT Aerosol Optical Depth (AOD) output files (equivalent to 10% of the total AOD HYSPLIT data set) were visually examined to ensure the validity of the results. These files were specifically checked for abnormal geometric features in spatial variability of AOD and for unreasonably high AOD values (AOD ≥1). Of the files checked, 8.3% (12 files) were noted to have issues such as suspect geometric AOD patterning or “spots,” which were inconsistent with

expected results. 40 files (27.8%) contained at least one hour when AOD was ≥1. The remaining 93 files checked (64.6%) exhibited no issues.

6.3 MAIAC Satellite AOD Data Quality Audit

219 MAIAC AOD satellite images (equivalent to 10% of the total MAIAC data set) were visually examined for indications of cloud masking, edge effects, and/or other spatial AOD abnormalities. 77 files (35.2%) were assessed as potentially having one of these issues. Of these 77 instances, in 13 files (5.9%) the cloud masking algorithm appeared especially aggressive at the center of fires, which materialized as a red triangular artifact at the center of some fires. The remaining 142 files (64.8%) exhibited none of the above issues. The masking of smoke was confirmed as an issue with processing of MODIS collection 6 MAIAC AOD (MCD19A2) that was not present in previous versions of the MAIAC retrieval. Where observed, the wildfire smoke masking issue impacted only the densest portion of the smoke plume, while the majority of the plume remained unmasked. Therefore, it is considered that images can still be used for valid comparisons between the model and satellite data to evaluate the agreement for smoke-impacted locations.

7. Conclusions and Recommendations

The FINN modeling system was developed as a global-scale fire emissions model to estimate the daily emissions of trace gases and particles from open biomass burning. It was designed to support atmospheric chemical transport modeling, including consistent, high temporal and spatial resolution across local to global scales and chemical speciation of compounds for common atmospheric chemical mechanisms. Since its initial release in 2010, the model and its applications have continued to evolve, which has culminated in the development of FINNv2.2.

The FINNv2.2 modeling system consists of three primary components that include the preprocessor, emissions model, and chemical speciation code. Its development addresses improvements needed to earlier versions, particularly in the detection of smaller fires and the estimation of area burned. The model incorporates recent data products and/or scientific findings for active fire detections, land cover characterization, biomass loadings, emission factors, and the chemical speciation of NMOC. It is an open source code available through the GitHub development platform.

Global simulations for 2016 and 2018 highlighted the effects of fire activity on emissions estimates for different regions of the world, as well as the interannual variability of emissions between the 2016 and 2018 fire seasons. Emissions estimates were developed for 2012 through 2018 for North America. In Texas during this time span, years with relatively higher peaks in emissions, which typically occurred in the late winter/spring, included 2013 and 2016, 2017, and in particular 2018.

During 2016, fire activity in Texas primarily occurred during the winter/spring months with peak emissions in February, as well as the late summer/fall with peak emissions in September. $PM_{2.5}$, NO_x, and NMOC emissions exhibited the same seasonal patterns. Grasslands had a greater contribution to fire activity in February 2016 than September 2016. Forests provided smaller contributions to total area burned and NO_x emissions than grasses or shrublands in Texas but had more pronounced influences on emissions of $PM_{2.5}$ and especially NMOC.

Several significant changes occurred between FINNv1.5 and v2.2. Overall the changes led to increases in emissions of $PM_{2.5}$, NO_x and NMOC with v2.2 in Texas. It is difficult to capture the full complexity of the interactions between model parameters that contribute to variations emissions estimates for any given fire event or between different fire events. However, it is evident that the new algorithm implemented in FINNv2.2 to address the limitations in the burned area assumptions of previous versions and the inclusion of active fire detections from VIIRS have made important contributions to the differences in emissions estimates. Transitions to more recent MODIS active fire detection and land cover data products, as well as biomass loadings from the USDA Forest Service FCCS, also play a role. Emission factors are similar between the model versions with the notable exception of NMOC. All measured NMOC is included in the applied emission factor for FINN v2.2 rather than only the identified NMOC fraction. This change dominates the contribution to differences in these emissions estimates between the model versions.

Overall results of the model evaluation indicate that photochemical modeling with FINN fire emissions shows reasonable agreement with independent satellite data (FB ~50%, FAC2 ~55%). The model performance improved for cases with higher average AOD, showing reduced levels

of error and bias. HYSPLIT model results showed good agreement between surface observations of total carbon at the surface, indicating that the model well-represents the distribution of $PM_{2.5}$ from wildfire smoke at ground level. However, HYSPLIT results generally showed poor performance when compared to satellite data. In particular, HYSPLIT's estimates are biased low relative to satellite observations, likely due to the lack of simulated aerosols from non-fire sources. Agreement between HYSPLIT model results and satellite observations improved at times when smoke emissions were elevated above normal levels.

Results of the evaluation indicate that the modifications to FINN made between versions 1.5 and 2.2 have improved representation of wildfire smoke in the photochemical modeling results. Overall statistics for the CAMx model AOD comparison with satellite data indicate similar performance with the two versions of the emissions model. However, when smoke-dominated events were identified, the relationship between modeled and observed AOD improved for both FINN emissions versions. Furthermore, the case studies of smoke events show that model runs conducted with FINN v2.2 frequently showed better agreement with satellite observations of AOD relative to model runs conducted with FINN v1.5. These results indicate that the domain-wide statistics are dominated by variability in AOD unrelated to wildfire smoke. By focusing on high-smoke cases, we are able to identify and quantify notable improvements in model performance between FINN v1.5 and FINN v2.2. Prior work has shown success in using satellite AOD retrievals for assessing emissions models for biomass burning, where model agreement has increased substantially during periods of heavy smoke activity (Rolph et al., 2009). The evaluation performed here further demonstrate the value of emissions inventory assessment using satellite data.

It is recommended that FINNv2.2 continue to undergo evaluation across different regions of the world and that new findings from on-going field campaigns continue to be used to inform future evolution of the model.

8. References

Air Sciences, Inc., 2005, 2002 Fire Emission Inventory for the WRAP Region – Phase II, Western Governors Association/Western Regional Air Partnership, Project NO. 178-6, July 22, 2005.

Akagi, S. K., R. J. Yokelson, C. Wiedinmyer, M. J. Alvarado, J. S. Reid, T. Karl, J. D. Crounse, P. O. Wennberg, 2011, Emission factors for open and domestic biomass burning for use in atmospheric models, *Atmospheric Chemistry and Physics*, 11(9), 4039-4072.

Crippa, P., S. Castruccio, S. Archer-Nicholls, G. B. Lebron, M, Kuwata, A. Thota, S. Sumin, E. Butt, C. Wiedinmyer, D. V. Spracklen, 2016, Population exposure to hazardous air quality due to the 2015 fires in

Equatorial Asia, *Scientific Reports*, 6: 37074.

Ester, M., Kriegel, H.P., Sander, J. and Xu, X., 1996. A density-based algorithm for discovering clusters in large spatial databases with noise, *Kdd*, 96(34), 226-231.

Fang, Z., W. Deng, Y. Zhang, X. Ding, M. Tang, T. Liu, Q. Hu, M Zhu, Z. Wang, W. Yang, Z. Huang, W. Song, X. Bi, J. Chen, Y. Sun, C. George, X. Wang, Open burning of rice, corn and wheat straws: primary emissions, photochemical aging, and secondary organic aerosol formation, *Atmospheric Chemistry and Physics*, 17, 14821–14839.

Hatch L. E., Yokelson, R.J., Stockwell, C.E., Veres, P.R., Simpson, I.J., Donald R. Blake, D.R., Orlando, J.J., Barsanti, K.C., 2017, Multi-instrument comparison and compilation of non-methane organic gas emissions from biomass burning and implications for smoke-derived secondary organic aerosol precursors, *Atmospheric Chemistry & Physics*, 17, 1471–1489.

Hoelzemann, J.J., M. G. Schultz, G. P. Brasseur, C. Granier, M.Simon, 2004, Global Wildland Fire Emission Model (GWEM): Evaluating the use of global area burnt satellite data, *Journal of Geophysical Research*, 109, D14S04.

Hurteau, M.D., Westerling, A.L., Wiedinmyer, C., Bryant, B.P., Projected Effects of Climate and Development on California Wildfire Emissions through 2100, *Environmental Science & Technology*, 2014, 48, 2298−2304.

Ivey, C., D. Lavoué, A. Davis, Y. Hu, A. Russell, 2014, CMAQ Simulations using Fire Inventory of NCAR (FINN) Emissions, 18th Annual CMAS Conference, Chapel Hill, NC, October 27-29, 2014.

Larkin, N., S.M. Raffuse, T. M. Strand, 2014, Wildland fire emissions, carbon, and climate: U.S. emissions inventories, *Forest Ecology and Management*, 317 (2014) 61–69.

Larkin, N.K., O'Neill, S.M., Solomon, R., Raffuse, S., Strand, T., Sullivan, D.C., Krull, C., Rorig, M., Peterson, J. and Ferguson, S.A., 2010, The BlueSky smoke modeling framework, *International Journal of Wildland Fire*, 18(8), 906-920.

Liu, X., G. Huey, R. J. Yokelson, V. Selimovic, I. J. Simpson, M. Müller, J. L. Jimenez, P. Campuzano-Jost, A. J. Beyersdorf, D. R. Blake, Z. Butterfield, Y. Choi, J. D. Crounse, D. A. Day, G. S. Diskin, M. K. Dubey, E. Fortner, T. F. Hanisco, W. Hu, L. E. King, L. Kleinman, S. Meinardi, T. Mikoviny, T. B. Onasch, B. B. Palm, J. Peischl, I. B. Pollack, T.

B. Ryerson, G.W. Sachse, A. J. Sedlacek, J. E. Shilling, S. Springston, J. M. St. Clair, D. J. Tanner, A. P. Teng, P. O. Wennberg, A. Wisthaler, G. M. Wolfe, 2017, Airborne measurements of western U.S. wildfire emissions: Comparison with prescribed burning and air quality implications, *Journal of Geophysical Research Atmospheres*, 122, 6108–6129.

Liu, Z., T. Shah, C. Emery, G. Yarwood, Review of Fire Plume Rise Algorithms and Recommendations for SMOKE/CMAQ, Memo to Alison Eyth, Office of Air Quality Planning and Standards, U.S. Environmental Protection Agency, From Ramboll Environ, Novato, CA, September 23, 2016.

Lyapustin, A., Korkin, S., Wang, Y., Quayle, B. and Laszlo, I., 2012. Discrimination of biomass burning smoke and clouds in MAIAC algorithm. *Atmospheric Chemistry and Physics,* 12(20), pp. 9679-9686.

Lyapustin, A., Wang, Y., Korkin, S. and Huang, D., 2018. MODIS Collection 6 MAIAC algorithm. *Atmospheric Measurement Techniques*, 11(10).

McCarty, J., 2011, Remote sensing-based estimates of annual and seasonal emissions from crop residue burning in the contiguous United States, 2011, *Journal of the Air & Waste Management Association*, 61(1), 22-34.

McDonald-Buller, E., Y. Kimura, C. Wiedinmyer, C. Emery, 2013, The effects of uncertainties in fire emission estimates on predictions of Texas air quality, Submitted to the Texas Air Quality Research Program (Project #12-018), http://aqrp.ceer.utexas.edu/.

McDonald-Buller, E., Y. Kimura, C. Wiedinmyer, C. Emery, Z. Liu, G. Yarwood, 2015, Targeted improvements in the Fire INventory from NCAR (FINN) model for Texas air quality planning, Submitted to the Texas Air Quality Research Program (Project #14-011), http://aqrp.ceer.utexas.edu/.

McMillan, W.W., R.B. Pierce, L.C. Sparling, G. Osterman, K. McCann, M.L. Fischer, B. Rappengluck, R. Newson, D. Turner, C. Kittaka, K. Evans, S. Biraud, B. Lefer, A. Andrews, and S. Oltmans, 2010. An observational and modeling strategy to invetigate the impact of remote sources on local air quality: A Houston, Texas, case study from the Second Texas Air Quality Study (TexAQS II), *Journal of Geophysical Research*, *115,* D01301.

Morris, G.A., S. Hersey, A.M. Thompson, S. Pawson, J. E. Nielsen, P.R. Colarco, W.W. McMillan, A. Stohl, S. Turquety, J. Warner, B.J. Johnson, T. L. Kucsera, D. E. Larko, S.J. Oltmans, and J.C. Witte, 2006. Alaskan and Canadian forest fires exacerbate ozone pollution over Houston, Texas, on 19 and 20 July 2004, *Journal of Geophysical Research*, 111, D24S03.

Morris, R. E. Tai, C.Loomis, Z. Adelman, 2012, Final Technical Memorandum No. 5 Fire Emissions, Wildfires, Prescribed Burns and Agricultural Burning Emissions, Submitted to Tom Moore, Western Regional Air Partnership (WRAP), April 27, 2012.

N. Santiago-De La Rosa, G. González-Cardoso, J. de Jesús Figueroa-Lara, M.a Gutiérrez-Arzaluz, Cl. Octaviano-Villasana, I. Fabiola Ramírez-Hernández, V. Mugica-Álvarez, 2018, Emission factors of atmospheric and climatic pollutants from crop residues burning, *Journal of the Air & Waste Management Association*, 68:8, 849-865.

National Aeronautics and Space Administration (NASA), https://earthdata.nasa.gov/earth-observation-data/near-real-time/firms/viirs-i-band-active-fire-data, accessed July 2019.

Nuryanto, D.E., 2015, Simulation of forest fires smoke using WRF-Chem model with FINN fire emissions in Sumatera, *Procedia Environmental Sciences*, 24, 65 – 69.

Paton-Walsh, C., T. E. L. Smith, E. L. Young, D. W. T. Griffith, É.-A. Guérette, New emission factors for Australian vegetation fires measured using open-path Fourier transform infrared spectroscopy – Part 1: Methods and Australian temperate forest fires, *Atmospheric Chemistry and Physics*, 14, 11313-11333.

Pereira, G., R. Siqueira, N. E. Rosário, K. L. Longo, S. R. Freitas, F. S. Cardozo, J.W. Kaiser, M. J. Wooster, 2016, Assessment of fire emission inventories during the South American Biomass Burning Analysis (SAMBBA) experiment, *Atmospheric Chemistry and Physics*, 16, 6961–6975.

Pimonsree, S., Vongruang, P., S. Sumitsawan, 2018, Modified biomass burning emission in modeling system with fire radiative power: Simulation of particulate matter in Mainland Southeast Asia during smog episode, *Atmospheric Pollution Research*, 9 (1), 133-145.

Pitchford , M., W. Malm, B. Schichtel, N. Kumar, D. Lowenthal, J. Hand. 2007. Revised Algorithm for Estimating Light Extinction from IMPROVE Particle Speciation Data, *Journal of the Air & Waste Management Association*, 57(11), 1326-1336.

Pouliot, G., V. Rao, J.K. McCarty, A. Soja, 2017. Development of the crop residue and rangeland burning in the 2014 National Emissions Inventory using information from multiple sources, *Journal of the Air & Waste Management Association*, 67(5).

Ramboll, 2015. User's Guide Emissions Processor, Version 3.22.

Randerson, J.T., Y. Chen, G. R. van der Werf, B. M. Rogers D. C. Morton, 2012, Global burned area and biomass burning emissions from small fires, *Journal of Geophysical Research*, 117, G04012.

Randles, C.A., Da Silva, A.M., Buchard, V., Colarco, P.R., Darmenov, A., Govindaraju, R., Smirnov, A., Holben, B., Ferrare, R., Hair, J. and Shinozuka, Y., 2017. The MERRA-2 aerosol reanalysis, 1980 onward. Part I: System description and data assimilation evaluation. *Journal of climate*, *30*(17), pp.6823-6850.

Reddington, C.L., W. T. Morgan, E. Darbyshire, J. Brito, H. Coe, P. Artaxo, J. Marsham, D. V. Spracklen, 2019, Biomass burning aerosol over the Amazon: analysis of aircraft, surface and satellite observations using a global aerosol model, *Atmospheric Chemistry and Physics*, 19, 9125–9152.

Rolph, G.D., R.R. Draxler, A.F. Stein, A. Taylor, M.G. Ruminski, S. Kondragunta, J. Zeng, H.C. Huang, G. Manikin, J.T. McQueen, P.M. Davidson, 2009. Description and verification of the NOAA smoke forecasting system: the 2007 fire season. *Weather and Forecasting,* 24(2), pp. 361-378.

Russell, A., 2018, Part of the state enter wilfire season earlier than usual, Texas A&M AgriLife Today, January 31, 2018.

Schoennagel, T., J. K. Balch, H. Brenkert-Smith, P. E. Dennison, B. J. Harvey, M. A. Krawchuk, N. Mietkiewicz, P. Morgan, M. A. Moritz, R. Rasker, M. G. Turner, C.

Whitlock, 2017, Adapt to more wildfire in western North American forests as climate changes, *Proceedings of the National Academy of Sciences*, 114 (18) 4582-4590.

Stavrakou1, T., J.-F. Müller, M. Bauwens, I. De Smedt, C. Lerot, M. Van Roozendael, P.-F. Coheur, C. Clerbaux, K. F. Boersma, R. van der A, Y. Song, 2016, Substantial underestimation of post-harvest burning emissions in the North China Plain revealed by multi-species space observations, 6:32307.

Stein, A.F., Draxler, R.R., Rolph, G.D., Stunder, B.J., Cohen, M.D. and Ngan, F., 2015. NOAA's HYSPLIT atmospheric transport and dispersion modeling system, *Bulletin of the American Meteorological Society*, 96(12).2059-2077.

Stockwell1, C.E., P. R. Veres, J. Williams, R. J. Yokelson, 2015, Characterization of biomass burning emissions from cooking fires, peat, crop residue, and other fuels with high-resolution proton-transfer-reaction time-of-flight mass spectrometry, *Atmospheric Chemistry and Physics*, 15, 845-865.

Texas Commission on Environmental Quality, Houston 2011 $PM_{2.5}$ Exceptional Event Demonstration for a $PM_{2.5}$ Exceptional Event at the Houston Clinton Monitoring Site, August 30, 2013.

U.S. Environmental Protection Agency, 2018. 2014 National Emissions Inventory, version 2 Technical Support Document. Accessed from https://www.epa.gov/air-emissions-inventories/2014-national-emissions-inventory-nei-technical-support-document-tsd

Urbanski, S. P., M. C. Reeves, R. E. Corley, R. P. Silverstein, W Min Hao, 2018. Contiguous United States wildland fire emission estimates during 2003–2015, *Earth System Science Data*, 10, 2241–2274.

Urbanski, S., 2014, Wildland fire emissions, carbon, and climate: Emission factors. *Forest Ecology and Management*, 317, 51-60.

Val Martin, M., Kahn, R. and Tosca, M., 2018. A Global Analysis of Wildfire Smoke Injection Heights Derived from Space-Based Multi-Angle Imaging. *Remote Sensing*, *10*(10), p.1609.

van Leeuwen, T.T., G. R. van der Werf, A. A. Hoffmann, R. G. Detmers, G. Rücker, N. H. F. French, S. Archibald, J. A. Carvalho Jr., G. D. Cook, W. J. de Groot, C. Hély, E. S. Kasischke, S. Kloster, J. L. McCarty, M. L. Pettinari, P. Savadogo, E. C. Alvarado, L. Boschetti, S. Manuri, C. P. Meyer, F. Siegert, L. A. Trollope, W. S. W. Trollope, 2014, Biomass burning fuel consumption rates: a field measurement database, *Biogeosciences*, 11, 7305-7329.

Villanueva-Fierro, I., C.J. Popp, R.W. Dixon, R.S. Martin, J.S. Gafney, N.A. Marley, J.M. Harris, 2009. Ground-level chemical analysis of air transported from the 1998 Mexican-Central American fires to the Southwestern USA, *Revista Internacional de Contaminacion Ambiental, 25*(1), pp. 23-32.

Wang, J., S.C. Van den Heever, J.S. Reid, 2009, A conceptual model for the link between Central American biomass burning aerosols and severe weather over the south central United States, *Environmental Research Letters*, *4*(1), 015003.

Wang, Y., R. Talbot High background ozone events in the Houston-Galveston-Brazoria Area: Causes, effects, and case studies of Central American fires, Submitted to the Texas Air

Quality Research Program (Project #16-008), 2017, http://aqrp.ceer.utexas.edu/.

Westenbarger, D.A., G. A. Morris, 2018, Identifying biomass burning impacts on air quality in Southeast Texas 26–29 August 2011 using satellites, models and surface data, *Atmospheric Chemistry & Physics*, discussion paper preprint.

Western Regional Air Partnership, 2005, 2002 Fire Emission Inventory for the WRAP Region – Phase II, Project No. 178-6, 1–97, https://www.wrapair.org//forums/fejf/documents/WRAP_2002_PhII_EI_Report_20050722.pdf (last access: 26 Jun 2019), 2005.

Wiedinmyer, C., S. K. Akagi, R. J. Yokelson, L. K. Emmons, J. A. Al-Saadi, J. J. Orlando, A. J. Soja, 2011, The Fire INventory from NCAR (FINN): a high resolution global model to estimate the emissions from open burning, *Geoscientific Model Development*, 4(3), 625-641.

Z. Liu, T. Shah, C. Emery, G. Yarwood, Ramboll Environ, Novato, CA

Appendix A. - Chemical Speciation

Table A1. Chemical speciation profile applied to FINN (VOC) emissions(g) for the MOZART-T1 chemical mechanism (moles) as a function of land cover type.

Description	MOZART-T1 Species	Grassland and Savanna	Boreal Forest	Tropical Forest	Temperate Forest	Woody Savanna/ Shrubland	Croplands
alpha-pinene	APIN	0.009	0.259	0.000	0.261	0.053	0.010
benzene	BENZENE	0.144	0.290	0.000	0.253	0.442	0.091
lumped alkanes C>3	BIGALK	0.156	1.821	0.219	0.415	0.644	0.246
lumped alkenes C>3	BIGENE	1.467	0.627	0.662	1.393	1.274	0.674
beta-pinene	BPIN	0.000	0.209	0.000	0.008	0.004	0.000
benzaldehyde	BZALD	0.791	0.166	0.120	0.298	0.272	0.325
ethyne (acetylene)	C2H2	2.103	1.167	0.672	2.513	1.975	1.701
ethene	C2H4	1.218	1.407	1.505	1.930	2.886	1.412
ethane	C2H6	0.859	1.168	0.939	0.611	0.641	0.673
propene	C3H6	0.647	0.499	0.603	0.487	0.557	0.457
propane	C3H8	0.090	0.194	0.114	0.149	0.561	0.142
formaldehyde	CH2O	1.532	1.361	2.299	2.181	2.285	1.716
ethanol	C2H5OH	0.000	0.023	0.000	0.066	0.055	0.000
acetaldehyde	CH3CHO	1.037	0.416	1.404	0.758	0.792	0.929
acetonitrile	CH3CN	0.117	0.176	0.399	0.088	0.130	0.142
acetone	CH3COCH3	0.201	0.242	0.433	0.297	0.242	0.162
acetic acid	CH3COOH	2.371	1.360	2.029	1.292	1.353	2.349
methanol	CH3OH	1.451	1.608	3.031	1.744	1.650	2.328
lumped cresols (hydroxymethylbenzenes)	CRESOL	0.059	0.040	0.000	0.059	0.058	0.074
glycolaldehyde	GLYALD	0.390	0.233	1.886	0.210	0.128	0.800
hydrogen cyanide	HCN	0.559	0.846	0.625	0.684	0.927	0.416
formic acid	HCOOH	0.206	0.254	0.683	0.259	0.134	0.426
nitrous acid	HONO	0.298	0.228	1.001	0.326	0.643	0.187
hydroxyacetone	HYAC	0.309	0.149	0.609	0.223	0.118	1.548
isoprene	ISOP	0.069	0.085	0.029	0.129	0.138	0.062
limonene	LIMON	0.000	0.000	0.000	0.158	0.013	0.000
methacrolein	MACR	0.000	0.024	0.222	0.113	0.147	0.000
methyl ethyl ketone	MEK	0.370	0.104	0.666	0.274	0.286	0.387
methyl glyoxal	CH3COCHO	0.347	0.090	0.000	0.135	0.094	0.171
methyl vinyl ketone	MVK	0.317	0.087	0.222	0.247	0.301	0.193
limonene	MYRC	0.000	0.000	0.000	0.002	0.003	0.000
phenol, product of benzene chemistry	PHENOL	0.472	0.517	0.191	0.345	0.457	0.408
toluene	TOLUENE	0.457	1.327	0.769	0.605	0.531	0.375

Description	MOZART-T1 Species	Grassland and Savanna	Boreal Forest	Tropical Forest	Temperate Forest	Woody Savanna/ Shrubland	Croplands
lumped xylenes	XYLENES	0.385	0.238	0.040	0.422	0.355	0.295
dimethyl phenol from xylenes oxidation	XYLOL	0.108	0.056	0.000	0.088	0.046	0.130

Table A2. Mapping between MOZART-T1 and CB6r4 (gas phase) and CF (particulate phase) chemical species used in the EPS v.3.22 processing stream.

Description	MOZART-T1 Species	CB6r4 Species
carbon monoxide	CO	CO
oxides of nitrogen	NOx	NO2
sulfur dioxide	SO2	SO2
ammonia	NH3	NH3
alpha-pinene	APIN	TERP
benzene	BENZENE	BENZ
lumped alkenes C>3	BIGENE	0.75 OLE + 1.5 PAR + 0.25 IOLE
beta-pinene	BPIN	TERP
benzaldehyde	BZALD	TOL
ethyne (acetylene)	C2H2	ETHY
ethene	C2H4	ETH
ethanol	C2H5OH	ETOH
ethane	C2H6	ETHA
propene	C3H6	PAR + OLE
propane	C3H8	PRPA
formaldehyde	CH2O	FORM
acetaldehyde	CH3CHO	ALD2
acetonitrile	CH3CN	2*NR
acetone	CH3COCH3	ACET
methyl glyoxal	CH3COCHO	MGLY
acetic acid	CH3COOH	AACD
methanol	CH3OH	MEOH
lumped cresols (hydroxymethylbenzenes)	CRESOL	CRES

Description	MOZART-T1 Species	CB6r4 Species
glycolaldehyde	GLYALD	ALDX
hydrogen cyanide	HCN	NR
formic acid	HCOOH	FACD
nitrous acid	HONO	HONO
hydroxyacetone	HYAC	3*PAR
isoprene	ISOP	ISOP + ISP
limonene	LIMON	TERP
methacrolein	MACR	ISPD
methyl ethyl ketone	MEK	3*PAR + KET
methyl vinyl ketone	MVK	ISPD
limonene	MYRC	TERP
phenol, product of benzene chemistry	PHENOL	CRES
toluene	TOLUENE	TOL
lumped xylenes	XYLENES	XYL
dimethyl phenol from xylenes oxidation	XYLOL	CRES
particulate matter ≤2.5 μm	PM25*	-1*CPRM + [(1-*x*-*y*)*FPRM + *x**PSO4 + *y**PNO3]
organic carbon	OC+	1.7*POA + (-1.7)*FPRM
black carbon	BC	PEC + (-1)*FPRM
particulate matter ≤10 μm	PM10r	CPRM

*FINN PM25 is mapped to CF mechanism FPRM, PSO4 and PNO3. The distribution among three CB6 species are dependent on generic vegetation type identified by FINN. For the vegetation types of croplands, savanna and grasslands, woody savanna and shrublands, 3.45% PSO4 and 1.03% PNO3 is assumed. For other vegetation types (forests), 28.6% PSO4 and 2.86% PNO3 are assumed on mass basis. The remaining mass is mapped to FPRM.

+POA for the CF mechanism is estimated from OC in FINN, assuming an OA to OC ratio of 1.7. The masses of POA and EC are subtracted from FPRM estimate.

rCPRM for the CF mechanism is determined by subtracting FINN PM25 from PM_{10}.

Appendix B – CAMx v1.5 wildfire-only vs. HYSPLIT

Table B1. HYSPLIT vs. CAMx v1.5 wildfire-only AOD model comparison statistics. Monthly values are averaged hourly data for 2012. Values are provided with ± one standard deviation.

Month	N	Mean CAMx1 WF AOD	Mean HYSPLIT AOD	R	R^2	FB (%)	NMSE	FAC2
5	322	0.006 ± 0.003	0.019 ± 0.020	0.182 ± 0.265	0.103 ± 0.120	47 ± 66	8 ± 11	0.431 ± 0.495
6	322	0.006 ± 0.002	0.008 ± 0.004	0.204 ± 0.244	0.101 ± 0.122	15 ± 37	1 ± 1	0.559 ± 0.496
7	322	0.002 ± 0.001	0.003 ± 0.002	0.293 ± 0.248	0.147 ± 0.144	61 ± 45	6 ± 6	0.289 ± 0.453
8	322	0.004 ± 0.002	0.005 ± 0.003	0.306 ± 0.242	0.152 ± 0.138	14 ± 50	2 ± 1	0.436 ± 0.496
9	322	0.009 ± 0.006	0.011 ± 0.007	0.501 ± 0.222	0.301 ± 0.165	1 ± 46	1 ± 1	0.465 ± 0.496

Figure B1. Domain-wide HYSPLIT AOD values (mean model AOD - left) and CAMx v1.5 WF-only AOD values (mean observed AOD – bottom) for 2012. Linear regression equations and R^2 values for each comparison are shown at the top of the figure.

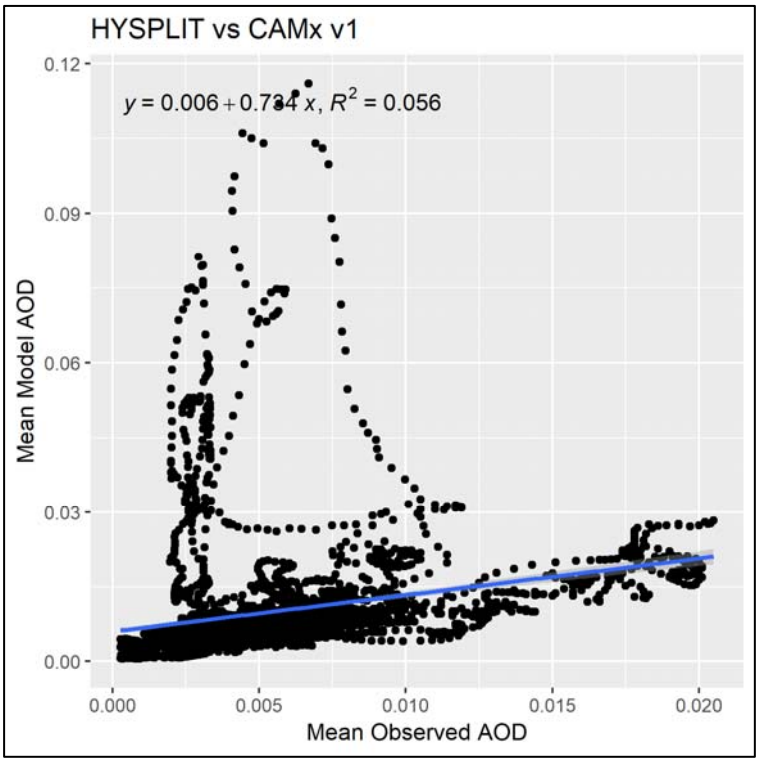

Figure B2. Domain-wide FB histogram of HYSPLIT vs. CAMx v2.2 wildfire-only AOD values for 2012.

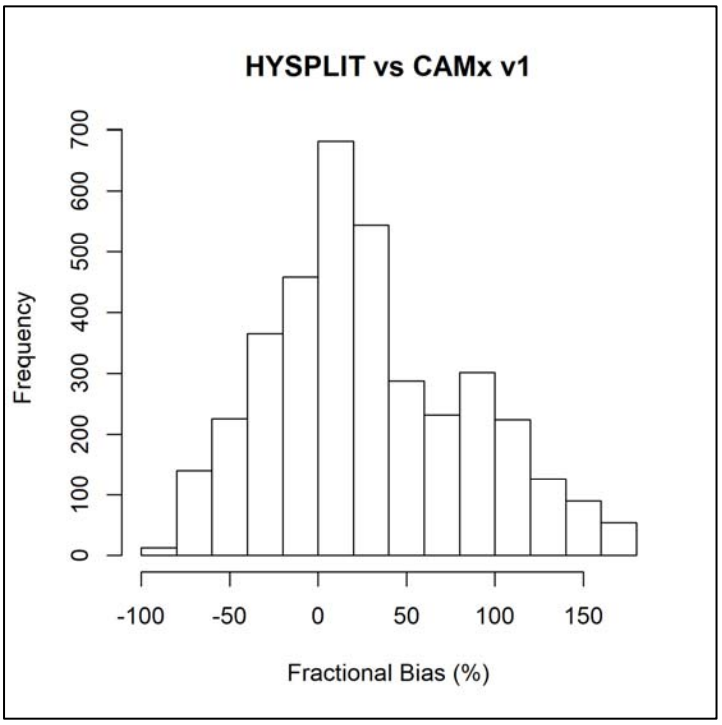

Figure B3. Domain-wide NMSE histogram of HYSPLIT vs. CAMx v1.5 WF-only AOD values for 2012-2017.

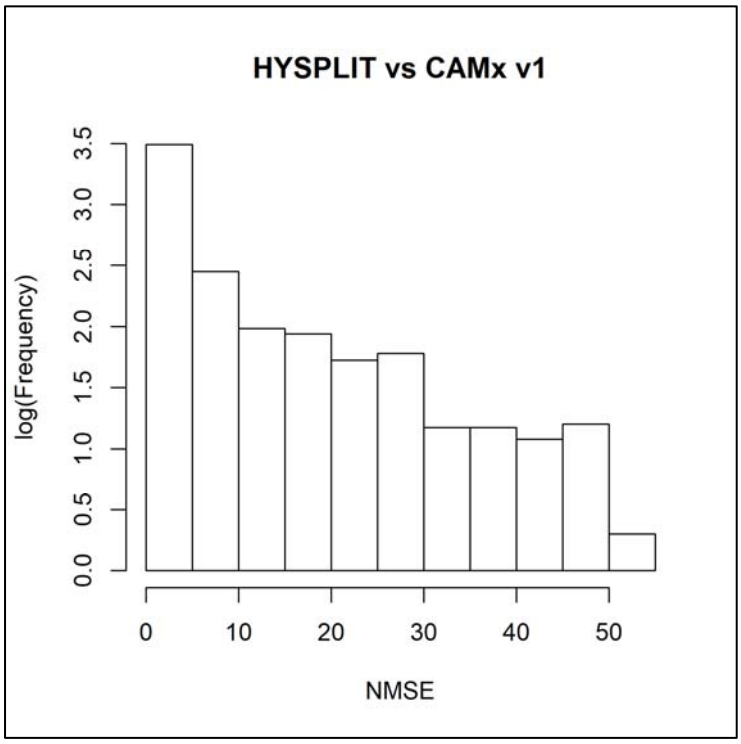

Figure B4. Domain-wide bugle plots of HYSPLIT vs CAMx v1.5 WF-only AOD values for 2012. The fractional bias bugle plot is shown on the left, while the fraction error bugle plot is shown on the right.

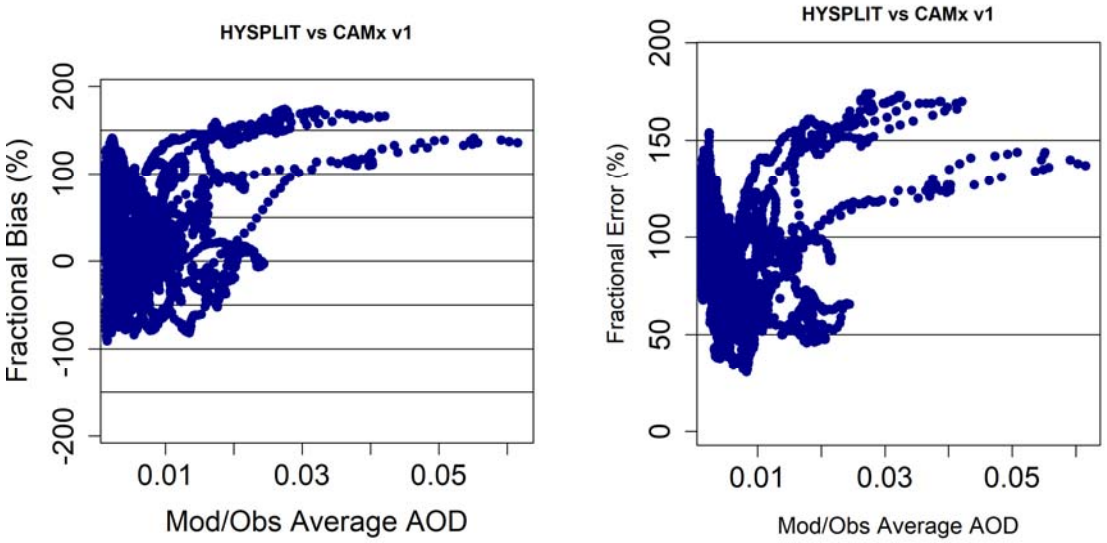

Figure B5. Domain-wide Q-Q plots of HYSPLIT (mean model AOD - left) and CAMx v1.5 (mean observational AOD - right) WF-only AOD values for 2012.

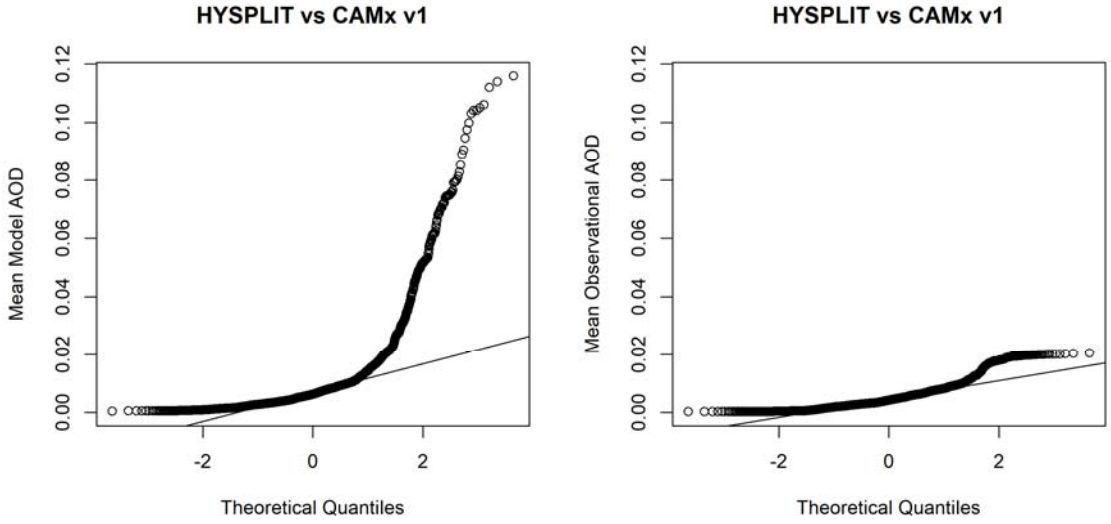

Figure B6. A domain-wide soccer plot of normalized mean error vs. normalized mean bias for HYSPLIT vs. CAMx v1.5 wildfire-only AOD data during 2012. Values are colored by the maximum HYSPLIT AOD value in the domain to assess the influence of wildfire smoke on bias and error between these two datasets

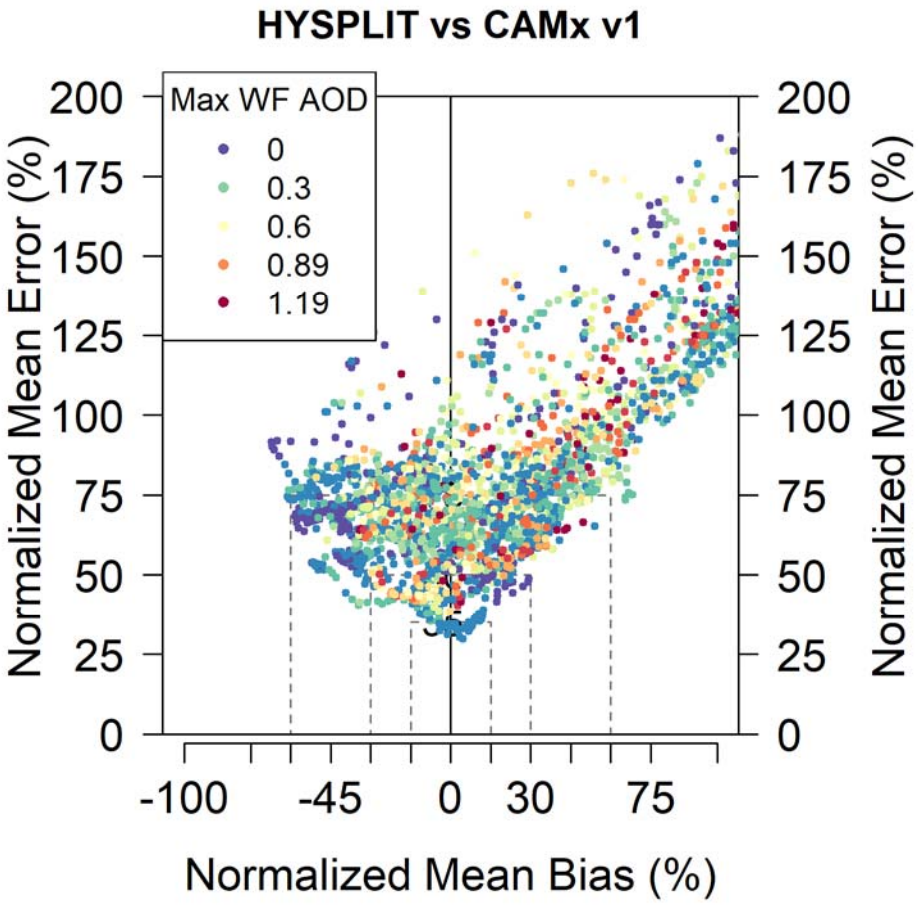

Appendix C – CAMx v1.5 vs. MAIAC

Table C1. MAIAC vs. CAMx v1.5 AOD model comparison statistics. Monthly values are averaged hourly data for 2012. Values are provided with ± one standard deviation.

Month	N	Mean MAIAC AOD	Mean CAMx1 AOD	R	R^2	FB (%)	NMSE	FAC2
5	6710	0.179 ± 0.066	0.264 ± 0.037	0.137 ± 0.300	0.108 ± 0.150	48 ± 37	0.497 ± 0.489	0.588 ± 0.492
6	6613	0.169 ± 0.068	0.274 ± 0.039	0.166 ± 0.295	0.114 ± 0.153	56 ± 34	0.564 ± 0.511	0.570 ± 0.495
7	5436	0.155 ± 0.082	0.243 ± 0.030	0.062 ± 0.272	0.077 ± 0.105	59 ± 43	0.767 ± 0.856	0.379 ± 0.485
8	7430	0.152 ± 0.054	0.245 ± 0.025	0.131 ± 0.262	0.085 ± 0.103	56 ± 33	0.540 ± 0.481	0.540 ± 0.498
9	10635	0.123 ± 0.056	0.255 ± 0.034	0.202 ± 0.261	0.108 ± 0.130	80 ± 34	1.099 ± 1.144	0.294 ± 0.455

Figure C1. Domain-wide CAMx v1.5 AOD values (mean model AOD - left) and MAIAC AOD values (mean observed AOD – bottom) for 2012. Linear regression equations and R^2 values for each comparison are shown at the top of the figure.

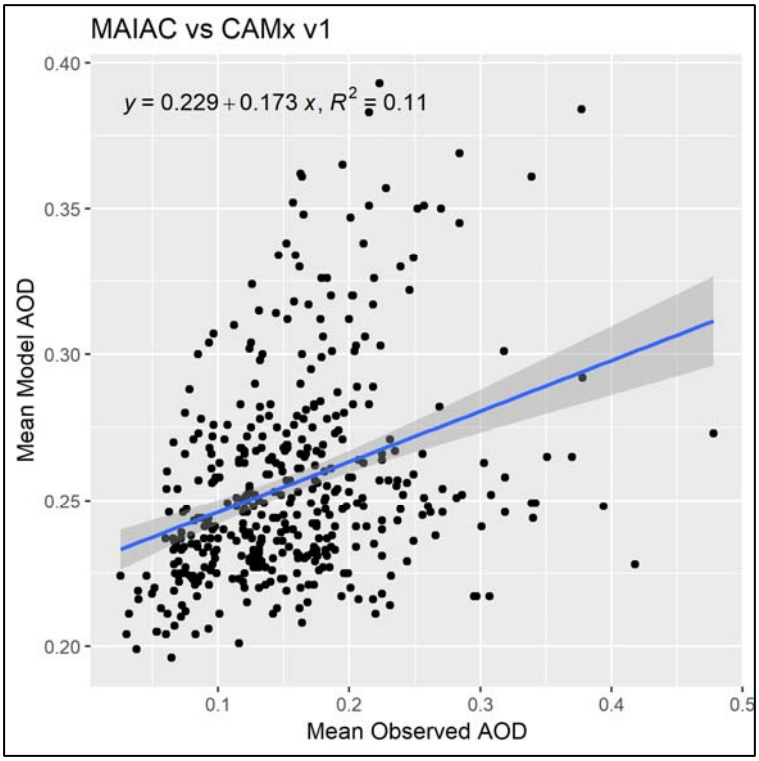

Figure C2. Domain-wide FB histogram of MAIAC vs. CAMx v1.5 AOD values for 2012.

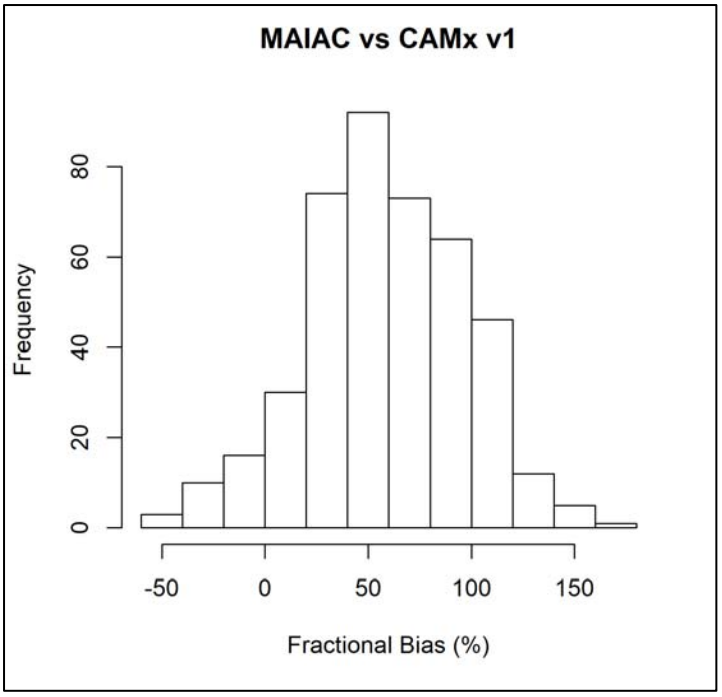

Figure C3. Domain-wide NMSE histogram of MAIAC vs. CAMx v1.5 AOD values for 2012.

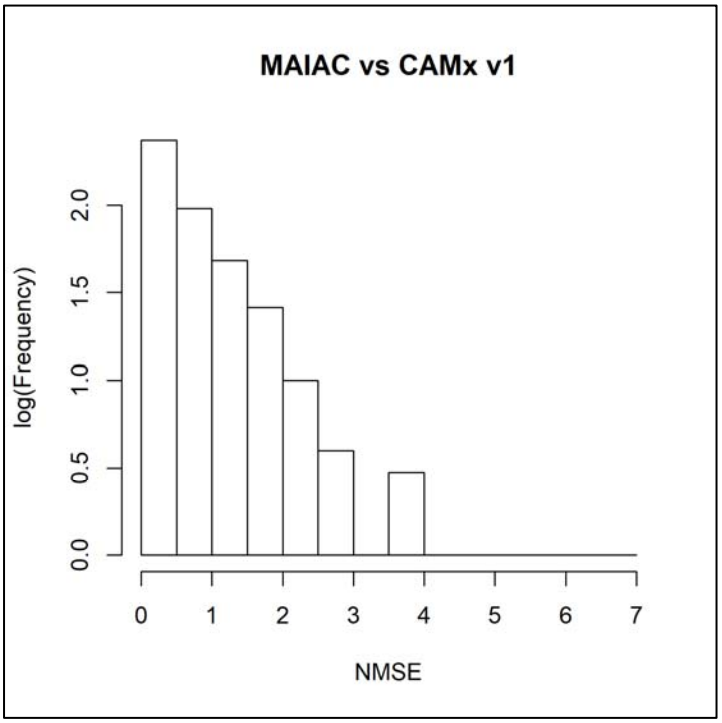

Figure C4. Domain-wide bugle plots of MAIAC vs CAMx v1.5 AOD values for 2012. The fractional bias bugle plot is shown on the left, while the fraction error bugle plot is shown on the right.

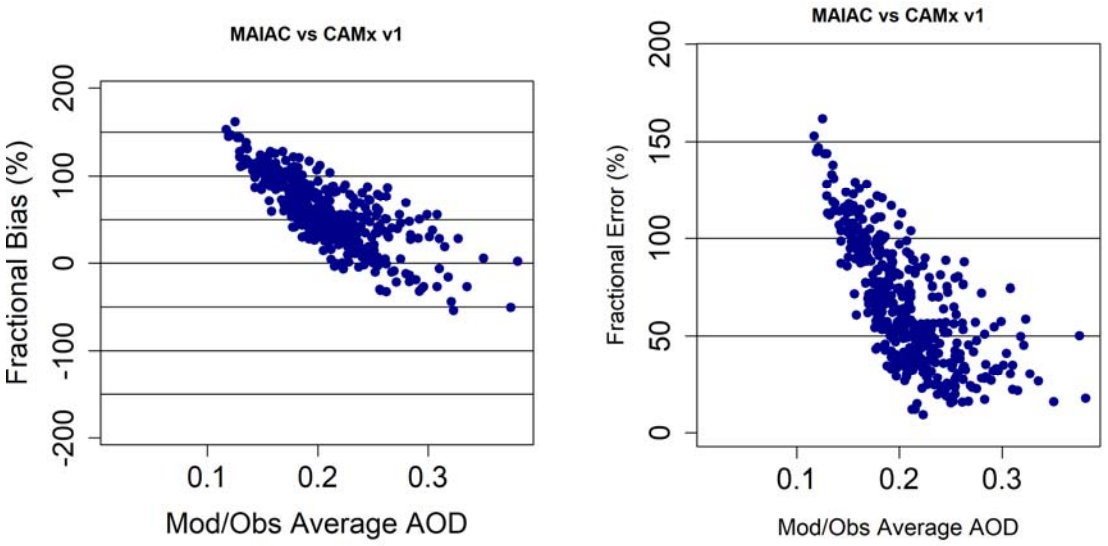

Figure C5. Domain-wide Q-Q plots of CAMx v1.5 (mean model AOD - left) and MAIAC (mean observational AOD - right) AOD values for 2012.

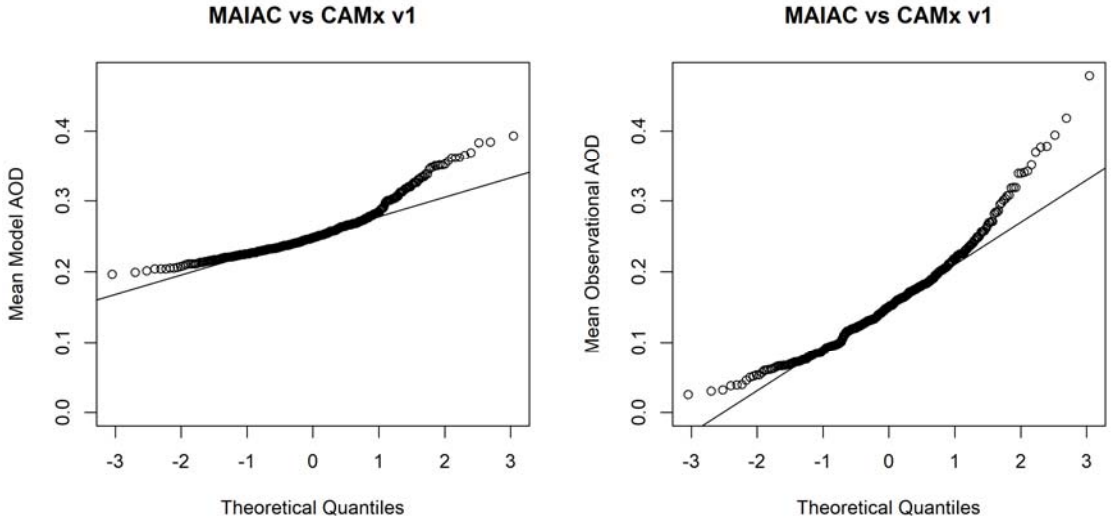

Figure C6. A domain-wide soccer plot of normalized mean error vs. normalized mean bias for MAIAC vs. CAMx v1.5 AOD data during 2012. Values are colored by the maximum CAMx v1.5 wildfire-only AOD value in the domain to assess the influence of wildfire smoke on bias and error between these two datasets.